Efficient Global Optimization of Multidisciplinary System using Variable Fidelity Analysis and Dynamic Sampling Method

Jangho Park

Dissertation submitted to the Faculty of the
Virginia Polytechnic Institute and State University
in partial fulfillment of the requirements for the degree of

Doctor of Philosophy
in
Aerospace Engineering

Seongim S Choi, Chair
Pradeep Raj, Co-chair
William J Devenport
Xi Chen

April 29, 2019
Blacksburg, Virginia

Keywords: Efficient Global Optimization(EGO), Variable-Fidelity(VF) Analysis, Data mining, Gaussian Process Regression(GPR) modeling, Design of Experiment(DoE)

Efficient Global Optimization of Multidisciplinary System using Variable Fidelity Analysis and Dynamic Sampling Method

Jangho Park

(ABSTRACT)

Work in this dissertation is motivated by reducing the design cost at the early design stage while maintaining high design accuracy throughout all design stages. It presents four key design methods to improve the performance of Efficient Global Optimization for multidisciplinary problems. First, a fidelity-calibration method is developed and applied to lower-fidelity samples. Function values analyzed by lower fidelity analysis methods are updated to have equivalent accuracy to that of the highest fidelity samples, and these calibrated data sets are used to construct a variable-fidelity Kriging model. For the design of experiment (DOE), a dynamic sampling method is developed and includes filtering and infilling data based on mathematical criteria on the model accuracy. In the sample infilling process, multi-objective optimization for exploitation and exploration of design space is carried out. To indicate the fidelity of function analysis for additional samples in the variable-fidelity Kriging model, a dynamic fidelity indicator with the overlapping coefficient is proposed. For the multidisciplinary design problems, where multiple physics are tightly coupled with different coupling strengths, multi-response Kriging model is introduced and utilizes the method of iterative Maximum Likelihood Estimation (iMLE). Through the iMLE process, a large number of hyper-parameters in multi-response Kriging can be calculated with great accuracy and improved numerical stability. The optimization methods developed in the study are validated with analytic functions and showed considerable performance improvement. Consequentially, three practical design optimization problems of NACA0012 airfoil, Multi-element NLR 7301 airfoil, and all-moving-wingtip control surface of tailless aircraft are performed, respectively. The results are compared with those of existing methods, and it is concluded that these methods guarantee the equivalent design accuracy at computational cost reduced significantly.

Efficient Global Optimization of Multidisciplinary System using Variable Fidelity Analysis and Dynamic Sampling Method

Jangho Park

(GENERAL AUDIENCE ABSTRACT)

In recent years, as the cost of aircraft design is growing rapidly, and aviation industry is interested in saving time and cost for the design, an accurate design result during the early design stages is particularly important to reduce overall life cycle cost. The purpose of the work to reducing the design cost at the early design stage with design accuracy as high as that of the detailed design.

The method of an efficient global optimization (EGO) with variable-fidelity analysis and multidisciplinary design is proposed. Using the variable-fidelity analysis for the function evaluation, high fidelity function evaluations can be replaced by low-fidelity analyses of equivalent accuracy, which leads to considerable cost reduction. As the aircraft system has sub-disciplines coupled by multiple physics, including aerodynamics, structures, and thermodynamics, the accuracy of an individual discipline affects that of all others, and thus the design accuracy during in the early design states.

Four distinctive design methods are developed and implemented into the standard Efficient Global Optimization (EGO) framework: 1) the variable-fidelity analysis based on error approximation and calibration of low-fidelity samples, 2) dynamic sampling criteria for both filtering and infilling samples, 3) a dynamic fidelity indicator (DFI) for the selection of analysis fidelity for infilled samples, and 4) Multi-response Kriging model with an iterative Maximum Likelihood estimation (iMLE).

The methods are validated with analytic functions, and the improvement in cost efficiency through the overall design process is observed, while maintaining the design accuracy, by a comparison with existing design methods. For the practical applications, the methods are applied to the design optimization of airfoil and complete aircraft configuration, respectively. The design results are compared with those by existing methods, and it is found the method results design results of accuracies equivalent to or higher than high-fidelity analysis-alone design at cost reduced by orders of magnitude.

Contents

List of Figures vii

List of Tables x

1 Introduction 1

1.1 Motivations and Objectives 1

1.2 Background 3

1.2.1 Optimization methods for design problems 3

1.2.2 Efficient Global Optimization(EGO) 6

1.2.3 Variable fidelity analysis 8

1.2.4 Kriging surrogate model 11

1.3 Scope of Research Work 13

1.4 Literature Survey 17

1.4.1 Variable fidelity analysis and adaptive sampling 17

1.4.2 Sample infilling and dynamic fidelity indicator 19

1.4.3 Multi-Response Kriging model for multidisciplinary problems 20

1.5 Contribution 24

2 Single Discipline Optimization 26

2.1 Kriging Surrogate Model 27

2.2 Variable Fidelity Analysis 30

2.3 Dynamic and Adaptive Sampling Method 34

2.3.1 Filtering low-accuracy samples . . . 34
2.3.2 Infilling samples for single fidelity optimization . . . 37
2.3.3 Infilling samples for variable fidelity optimization . . . 45
2.4 Dynamic Fidelity Indicator . . . 49
2.5 Variable Fidelity EGO Framework . . . 50

3 Extension to Multidisciplinary Optimization **52**
3.1 Multi-response Kriging (MRK) . . . 52
3.1.1 Reduced-Covariance Multi-Response Kriging (RC-MRK) . . . 53
3.1.2 Fully-Expanded-Covariance Multi-Response Kriging (FEC-MRK) . . . 57
3.1.3 Comparisons between RC-MRK and FEC-MRK . . . 60
3.1.4 Iterative method for Maximum Likelihood (iMLE) Estimation . . . 62
3.2 MRK for Variable Fidelity Optimization . . . 65

4 Validations **68**
4.1 Infill sampling criteria . . . 68
4.1.1 Parametric study on dynamic switching approach . . . 70
4.1.2 Cost comparison . . . 72
4.2 EGO Framework with Variable Fidelity Analysis . . . 75
4.2.1 Cost comparison . . . 75
4.2.2 Sensitivity to filtering criteria . . . 81
4.3 Multi-Response Kriging model . . . 83
4.3.1 Global accuracy . . . 84
4.3.2 Local accuracy . . . 88

5 Design Applications **93**

5.1 Aeroelastic Shape Optimization Airfoil 93

5.2 Aerodynamic shape optimization of high-lift multi-element airfoil 97

5.2.1 Design problem 97

5.2.2 High-fidelity aerodynamic analysis 99

5.2.3 Design results 100

5.3 Aerodynamic shape optimization of control surface of tailless aircraft 104

5.3.1 Innovative control effectors 105

5.3.2 Design problem 106

5.3.3 Variable-fidelity aerodynamic analysis 107

5.3.4 Design results 109

6 Conclusion **112**

Bibliography **115**

List of Figures

1.1 Life cycle cost and impact on cost for each design phrase 1

1.2 Schematics of EGO process 6

1.3 Example of different fidelity analysis methods in Aerodynamics 9

1.4 Comparison of lift coefficient of NACA 0015 airfoil 11

1.5 Example of Gaussian process with 5 samples 12

1.6 Probability density function of estimated function value 12

1.7 Developed design methods for Efficient Global Optimization 16

2.1 OVL coefficient between two probability functions 35

2.2 Pareto-front for ISC 42

2.3 Comparison of probability density function of calibrated lower fidelity Kriging, the highest fidelity Kriging, and variable fidelity Kriging at an arbitrary design point 46

2.4 Pareto-front for ISC in variable-fidelity Kriging 48

2.5 The schematics of variable fidelity EGO framework 51

3.1 The comparison of the number of hyper-parameter for different number of input and output variate 62

3.2 The schematics of iterative Maximum Likelihood Estimation (k = iteration number) 63

3.3 Example of Kriging in variable fidelity optimization 66

3.4 Example of the use of multi-response Kriging in variable fidelity multidisciplinary design problem 67

4.1 Configurations and iso-contours of six-hump camel back function 69
4.2 Configurations and iso-contours of Matlab peak function 70
4.3 Parameter study results for six hump camel back function 71
4.4 Parameter study results for Matlab peak function 72
4.5 2D contour and 3D plot of six hump camel back function with different fidelities 77
4.6 Design history of 3D plots of VF optimization framework for six hump camel back function 78
4.7 Comparison of variable fidelity and high fidelity optimization for six hump camel back function 78
4.8 2D contour and 3D plot of simplified Rastrigin function with different fidelities 80
4.9 Design history of VF optimization framework with the simplified Rastrigin function 81
4.10 Comparison of variable fidelity and high fidelity optimization for simplified Rastrigin function 81
4.11 Design iterations and the CCF w.r.t the varying filtering criteria (six hump camel back function) 82
4.12 Design iterations and the CCF w.r.t the varying filtering criteria (simplified Rastrigin function) 83
4.13 The contour of weakly coupled functions 85
4.14 The result of global accuracy test for weakly coupled function 86
4.15 The sliced contour of strongly coupled functions ($z_1 = 0$) 86
4.16 The result of global accuracy test for strongly coupled function 87
4.17 The contour of objective function for weakly coupled case 89
4.18 The comparison of f_1 and f_2 contour at the last iteration (Weakly coupled function) 90
4.19 The result of EGO test for weakly coupled functions 91

4.20 The contour of objective function for strongly coupled case($z_1 = 0$) 91
4.21 The result of EGO test for strongly coupled functions 92

5.1 NACA 0012 diagram with design variables 94
5.2 Aerodynamic analysis result of NACA0012 baseline airfoil 95
5.3 Aerodynamic force and aeroelastic torsion of the wing 95
5.4 Schematic of airfoil optimization process 96
5.5 Configuration of design variables in NLR 7301 multi-element airfoil 98
5.6 Validation of CFD analysis for baseline airfoil 100
5.7 Comparison of objective value variations w.r.t the number of sample points . 103
5.8 Comparison of baseline and design results in pressure coefficient contour . . 103
5.9 Comparison of baseline and design results in geometry 104
5.10 ICE 101 configuration and the models for wind tunnel test 105
5.11 Control surfaces of ICE 101 configuration 106
5.12 Design variables of AMT 107
5.13 Surface mesh for computational methods 108
5.14 Pressure coefficient contour comparison between each method (M=0.3, α=3.76 °) 108
5.15 The comparison of pressure coefficient along the cross section between each method (M=0.3, α=3.76 °) 109
5.16 Design history for the optimum AMT shape between VF optimization and HF optimization 110
5.17 The comparison of AMT shape 111
5.18 Pressure contour of the optimum AMT design result by variable fidelity optimization 111

List of Tables

2.1 The algorithms of the approximated q-EI 40

3.1 Comparison of the number of hyper-parameters in various GPR models . . . 61

4.1 A total required number of sample points (Six hump camel back function) . 73

4.2 A total required number of sample points (Matlab Peak Function) 74

5.1 NACA 0012 airfoil optimization results 97

5.2 Design variable bound for NLR 7301 multi-element airfoil optimization . . . 99

5.3 Aerodynamic performance of the minimum point 102

5.4 Design variable of the minimum point 102

5.5 Comparison of Design result for AMT shape 111

List of Abbreviations

Symbols

α	multiplicative error
β	additive error
$\boldsymbol{I}_a$	Identity matrix whose size is $(a \times a)$
$\boldsymbol{w}$ or $\boldsymbol{W}$	a vector of regression parameter for linear regression
ϵ	additive Gaussian noise with zero mean and non-zero variance
κ	switching parameter for MPMO-ISC, dynamic switching approach
$\mathcal{I}^+$	the set of index of the infilling sample points
$\mathcal{I}^-$	the set of index of the filtered sample points
$\mathcal{I}^{\mathcal{VF}}$	the set of index of the sample points for variable fidelity Kriging
$\mathcal{I}$	the set of index for sample points prior to the adaptive sampling
μ	the mean function value of random variate
$\Phi(\cdot)$	cumulative probability density function
$\phi(\cdot)$	probability density function
σ^2	variance of Gaussian distribution
θ_G	global clustering parameter
θ_L	local clustering parameter
B	covariance matrix between responses
C	covariance matrix

c	covariance function
$Cov[\cdot,\cdot]$	covariance between two random variates
$det(\cdot)$	determinant of a matrix
$E[\cdot]$	expected value of random variate
EI	expected improvement
$G(\cdot,\cdot)$	Gaussian process with mean and variance
K	the number of total design iteration
KRG	Kriging interpolation function
n	the number of observed data points
n^*	the number of additional samples
n_{pop}	the total number of optimal candidates on the Pareto-front in MPMO-ISC process
OVL	overlapping coefficient
p	the number of design variables (the dimension of design space)
pdf	probability distribution function
q	the number of responses, disciplines or physics (the dimension of response space)
Q and R	spatial covariance matrix
r	the number of different fidelity for the sample analysis
T	Threshold for MPMO-ISC, dynamic switching approach
$Var[\cdot]$	variance of random variate
x or $\boldsymbol{x}$	sample location
y or $\boldsymbol{y}$	sample response

Superscripts

(k)	iteration number

Subscripts

aug	augmented vector
g, h	index for different responses
i, j	index for different sample locations
m	index for function fidelity
VF	variable fidelity

Letter modifiers

$\bar{}$	mean function value of Gaussian distribution
$\hat{}$	trial location
$\tilde{}$	location of adaptive infill sampling
$'$	calibrated function value
*	Optimized value

Abbreviations

CCF	Computational Cost Factor
CFD	Computational Fluid Dynamics
DFO	Derivative Free Optimization
EGO	Efficient Global Optimization
FDM	Finite Difference Method
FEC-MRK	Fully Expanded Covariance Multi-Response Kriging
GBO	Gradient Based Optimization

GPR	Gaussian Process Regression
iMLE	iterative Maximum Likelihood Estimation
IOC	Impact On Cost
ISC	Infill Sampling Criteria
LCC	Life Cycle Cost
MDO	Multidisciplinary Design Optimization
PDF	Probability Distribution Function
RANS	Reynolds-Averaged Navier-Stokes
RC-MRK	Reduced Covariance Multi-Response Kriging
RMSE	Root Mean Square Error

Chapter 1

Introduction

1.1 Motivations and Objectives

These days, both the military and commercial aircraft industries show a dramatic escalation in cost across a unit's life cycle. According to Augustine's law [1], the unit cost for U.S. combat aircraft has grown by a factor of four every decade. Therefore, considering the trend of cost increase, the aviation industry is focusing on reducing the total life cycle cost (LCC) in aircraft design and manufacturing.

Fig. 1.1 shows the graph of the life cycle cost and impact on cost of an aircraft design at each stage of its life cycle [2, 3]. At the early design stages, namely the pre-conceptual, conceptual, and preliminary design stages, the cumulative percentage of LCC is less than

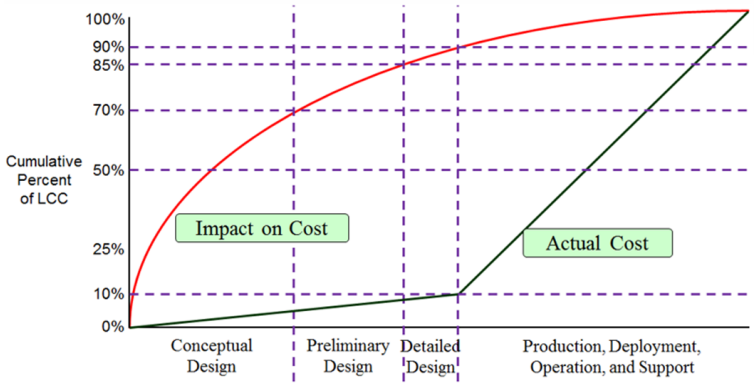

Figure 1.1: Life cycle cost and impact on cost for each design phrase

10%. The most of actual cost is concentrated on the later stages since the production of the designed aircraft takes a huge cost. While the cumulative percentage of actual cost at the early design stage is small, the impact on cost (IOC) is considerable, accounting for more than 80%. This shows the importance of accurate design at the early design stage. If a problem is discovered late in the design stage, correcting the issue will result in a major cost. Therefore, obtaining accurate design results at the early design stages provides huge cost savings, along with improved efficiency and effectiveness of the whole design process.

To achieve the goal of accurate design at the early design stage, many studies have been done to obtain accurate analysis results in various disciplines and apply them into the design. For example, in aerodynamics, potential flow codes or panel codes were developed in the late 1960s to early 1970s.

As numerical solutions of differential equations such as JST [4] and ROE [5] scheme have been developed, Euler or RANS(Reynolds-Average-Navier-Stokes) solutions have become the industry standard. The dramatic increment in the computing power with parallel computing and advanced CPUs lead to a development of Direct Numerical Simulation(DNS), Detached-Eddy Simulation(DES) and Large-Eddy Simulation(LES) in the past decades. As a result, designers are able to design aircraft precisely through analysis from reliable data similar to natural phenomena. However, the trade-off between the cost and accuracy in design results became an issue.

In the case of the panel method, it solves the two-dimensional airfoil problem in only a few seconds. Even in the case of three-dimensional geometry, it takes less than a minute. However, in the case of higher fidelity analysis such as Euler or RANS, it requires several hours of computational time even with a support of parallel computing. In particular, LES sometimes takes more than a day depending on the complexity of problem. As a result, it becomes a big issue how fast design can be done with accurate design results since the time

required for designing in the aviation industry is strongly related to the expenditure.

In this paper, the objective is set to develop a new design methodology which minimize the design cost while guaranteeing the accuracy of the design result. In the following section, several design concepts will be introduced and the research scope of the developed design methods will be introduced.

1.2 Background

1.2.1 Optimization methods for design problems

Any optimization problems are categorized into the two types: gradient-based optimization(GBO) or derivative-free optimization(DFO). The gradient-based optimization is an algorithm to solve a problem with the search directions calculated by the gradient values of the function at an individual optimizer throughout design iterations [6], and there are Newton's method, steepest descent method, conjugate gradient, and their variation methods. Therefore, the gradient values of the objective function of interest and associated constraints should be derived analytically or calculated numerically at each design iteration. Moreover, the GBO methods are easily trapped into the local optima, not being able to find the global optima. However, the GBO methods are still attractive as long as the gradient values can be calculated in an efficient way, as it allows a relatively large number of design variables.

The most challenging issue of the GBO methods is how to calculate precise gradient values at reasonable cost. The simplest method is the Finite Difference Method(FDM). Eq. 1.1 shows a simple equation of central difference method for function $f(x)$.

$$\frac{\partial f}{\partial x} = \frac{f(x + \Delta x) - f(x - \Delta x)}{2\Delta x} \tag{1.1}$$

With a step size Δx, which should be carefully chosen not to be subject to the subtractive cancellation errors, the second-order derivative can be calculate with two function calculations of $f(x + \Delta x)$ and $f(x - \Delta x)$. However, as the number of design variable increases, the number of function calculations for the derivative increases proportionally. If higher-order derivatives are used in the optimization, like Hessian values, the cost to calculate continuous deviates increases rapidly proportional to the number of design variables

The adjoint-based sensitivity analysis is a state-of-the-art method to compute the sensitivity values of model outputs with respect to input design variables using an adjoint equation, which is a linear differential equation derived from its primal equation using integration by parts [7]. The main advantage of the adjoint- based sensitivity analysis is that it can handle high dimensionality of design variable with relative ease. The computational cost of the adjoint-solution system is roughly equivalent to that of the function analysis even with the increased number of design variables.

However, it should be noted that the adjoint analysis has a disadvantages that the discrete adjoint equations should be re-derived whenever (1) different discretization schemes are used in the governing equations, and (2) different physics of structures or thermodynamics is included in the design problem. Prasad et al. derived the coupled adjoint equation for dynamic aero-elastic problems with applications to flutter and limit cycle oscillation (LCO) design optimization [8, 9]. The adjoint method is derived for the coupling of the Euler solver for aerodynamic analysis and the finite element solver for the structural analysis. If the problem is extended to aerothermoelasticity design, which considers the thermal interactions between the fluids and structures, the adjoint equation should be derived taking into account

the cross derivative terms for three physics disciplines.

On the other hand, the DFO methods search optimum candidates only by function evaluations and does not require gradient information. For the problems where the derivatives of the objective and constraint functions are very difficult or time-consuming to compute, the DFO methods can be very powerful tool. Genetic algorithm(GA) [10, 11], Nelder–Mead Simplex(Nonlinear Simplex) [12], and particle swarm optimization (PSO) are widely-used optimization algorithms. The DFO method estimates a number of design samples in the design space to determine the relations between samples and find the design optimum. Therefore, the global optima can be found by the algorithms, although the number of function evaluations and their cost associated increases greatly due to a huge number of samples and design variables.

The huge cost of the DFO methods can be mitigated by the surrogate model which approximates the objective function at an arbitrary location in the design space. The surrogate model is a mathematical model and approximates the exact function based on a number of observed discrete samples. Huge reduction in computational cost is the biggest advantage of the surrogate model due to an explicit form of the mathematical form. For example, the exact function evaluations for the genetic algorithm for a simple one dimensional optimization problem requires thousands of function calculations. However, the similar optimum result can be obtained by the surrogate model which is constructed by tens of function evaluations, and the design iteration is carried out with the surrogate model.

An algebraic regression or interpolation can be used as a simple surrogate model. However, in a practical engineering design, the advanced surrogate model such as polynomial response surfaces [13], Kriging model [14], or artificial neural networks(ANN) [15] are popularly used. Furthermore, to improve the cost-efficiency and accuracy of the design results, the concept of the DFO using the surrogate model is employed and applied to the Efficient Global

Optimization (EGO).

1.2.2 Efficient Global Optimization(EGO)

The method of Efficient Global Optimization(EGO) is popular for the computationally expensive black-box functions [16]. The basic concept of EGO is that the surrogate model of expensive black-box functions is constructed with a few number of initial samples, and the model is trained with infilled samples iteratively throughout the design. A general EGO process can be proceeded through five design steps as shown in Figure 1.2.

First, initial samples are randomly selected from the design space. Since the goal of the EGO process is to reduce the cost of optimization, the number of initial samples are restricted to be small. In fact, the number and the location of initial sample points are still an open research topic. By considering a general sampling rule, the number of samples can be $(p+1)(p+2)/2$, where p is the number of design variables (or the dimension of design space) [17]. To distribute the initial samples evenly in the multi-dimensional design space,

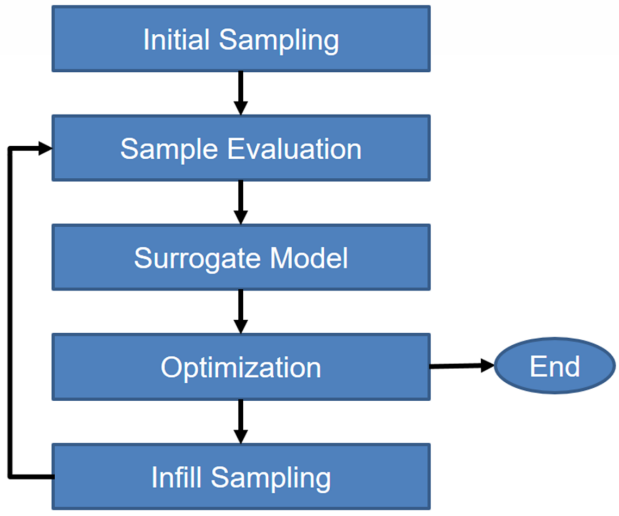

Figure 1.2: Schematics of EGO process

a diverse sampling technique including random sampling, orthogonal sampling, or Latin Hypercube Sampling (LHS) [18, 19] can be used.

Second, the function values of the samples are evaluated by computation or experiment. The sample point can have either a single or a multiple output function value. For example, in an aeroelasticity problem, a sample has both aerodynamics and structures result, i.e., a lift coefficient and a torsional angle.

Next, the surrogate model is constructed using a discrete set of observed or computed function values. Any models briefly discussed in the previous section can be used in this step. If the design problem is multidisciplinary, multiple surrogate models are constructed, each of which corresponds to an individual discipline. Otherwise, a single surrogate model is constructed.

Using the surrogate model, the optimum is searched throughout the design space while the function value at the trial location is evaluated by the surrogate model. The DFO method such as the Genetic Algorithm(GA) can be practically used with surrogate models. Once the global optimum is identified and predicted, the exact function value is evaluated either from the numerical computation or by an experiment, and the error from the predicted by the model is calculated to check the convergence of the iterative design process. If the error is lower than a pre-specified termination threshold, the design iteration is terminated. Otherwise, the design process continues for another iteration, followed by the adaptive infill sampling step to improve the accuracy of the surrogate model.

Since the EGO process begins with only a small number of sample points, the global and local accuracy of the model is not satisfactory during the early design iterations. The surrogate model should be trained with additional samples throughout the design iterations. During the infill sampling step, the locations of additional sample points are determined. Both

global and local accuracies are considered for the decision making. The global accuracy means the overall accuracy of surrogate model in the entire design space in comparison to the exact function. It is important to guarantee the global optimum. The local accuracy means the accuracy of the surrogate model near the optimum candidates, and is significant for the accuracy of the optimum result. Once the locations for the additional samples are determined, exact function values are calculated, and added to the existing training set. The surrogate models are updated by the additional function values.

The proposed, improved EGO method is advantageous for various reasons: the DFO algorithm can be effective for the identification of global optima in combination with (1) the surrogate model which replaces highly expensive physics simulations, and (2) the adaptive sampling strategy which further reduces the size of the total training sample set for design convergence.

Therefore, the accuracy of the surrogate model and the efficiency of the adaptive sampling strategy on the locations and number of sample points in the design space directly affects those of the EGO method. If the surrogate model is incorrectly constructed or the response is not well-approximating the exact function, the process will find incorrect optimum. Also, if the infilling is not carried out with efficiency, more additional sample points are incurred throughout the entire design iterations, and the advantage of the cost efficiency of the EGO method will be lost.

1.2.3 Variable fidelity analysis

The variable-fidelity (VF) analysis is a data fusion/integration method between data sets of different fidelity analysis. In the EGO process, as the computational simulation of the physical phenomena develops, designers have the opportunity to choose a fidelity for the

Method	Fidelity	Cost (3D Tailless aircraft)
Wind tunnel test	Real phenomena	Days to Months
RANS solution	High fidelity	<< 21,600s 64 CPUs with 20M volume cells
Euler solution	Medium fidelity	<< 3600s 64 CPUs with 5M volume cells
Potential Flow solver	Low fidelity	<< 3s 1 CPU with 4560 surface cells

Figure 1.3: Example of different fidelity analysis methods in Aerodynamics

analysis method for the problem of interest.

Figure 1.3 shows an example of aerodynamics analysis methods of different fidelity. In the figure, the level of fidelity of the aerodynamic analysis methods are shown in descending order. While a potential flow solver is developed based on the assumption of linear and irrotational velocity field which cannot account for flow viscosity [20], a Reynolds-Averaged Navier-Stokes (RANS) solver can consider the flow viscosity, providing more accurate solution. However, as the level of fidelity increases, the analysis cost increases accordingly. In the figure, the cost of analysis is estimated for the 3D tailless aircraft case [21]. By the potential flow solver, the computation can be done in a few seconds with only one CPU. However, the RANS solution takes about 6 hours with 64 CPUs using parallel computation platforms. While the wind tunnel test provides the most trustworthy data, it takes days to months to complete the experiments including model manufacturing and test setups.

In general, designers are forced to choose one of the analysis methods of different fidelity. If one chooses a low fidelity analysis method, such as a potential flow solver, a huge amount of design cost can be reduced, but there is uncertainty on the design result. Otherwise, if a higher fidelity method, such as a RANS solution, is selected, reliable design results can be obtained, but the cost is considerable. For example, in the 3D tailless aircraft case, if 100 samples are needed to construct a surrogate model for both potential flow solver only

case and RANS solution only case, the computational time for the function evaluations for sampled points will be 5 minutes and 600 hours, respectively.

The VF analysis can be a solution to these problems. The key concept of VF analysis is to use both a large number samples analyzed by the low fidelity analysis, called a low-fidelity samples, and a small number of samples analyzed by the high fidelity samples, called a low-fidelity samples. The low-fidelity samples can be used to describe the overall fit of exact function, and the high fidelity samples can be used to describe the local accuracy around the local point of interest, e.g., optimum candidate for the optimization problem. Let's assume that we can use 80 potential flow samples and 20 RANS samples in the tailless aircraft case. The total computational time for the function evaluations for all sample points will be 120 hours and 3 minutes. If the resultant design result is equivalent to that by the RANS solution only case, designers can save design cost considerably.

For the VF analysis, the data analyses including error estimation and calibration between different fidelity samples is critical to ensure overall high accuracy at the reduced cost. Figure 1.4 shows an example of aerodynamic analysis result of NACA 0015 airfoil at Reynolds number of 10^6. In the figure, the lift coefficients of NACA 0015 airfoil calculated by the potential flow solver, RANS solver [22], LES solver [23], and wind tunnel experiments [24] are compared. As the governing equations of computational analyses are modeling same physical phenomena around the airfoil, the results are in the same trend. However, because of the difference in fidelity, the lift coefficient curves shows discrepancies as well. In the figure, as the angle of attack increases, the discrepancy between potential flow solver result and other results increases.

Therefore, to use lower fidelity samples with high fidelity sample, the error between these two sample sets should be estimated, and lower fidelity samples should be calibrated to be as accurate as high fidelity samples. For this process, many researchers have studied the

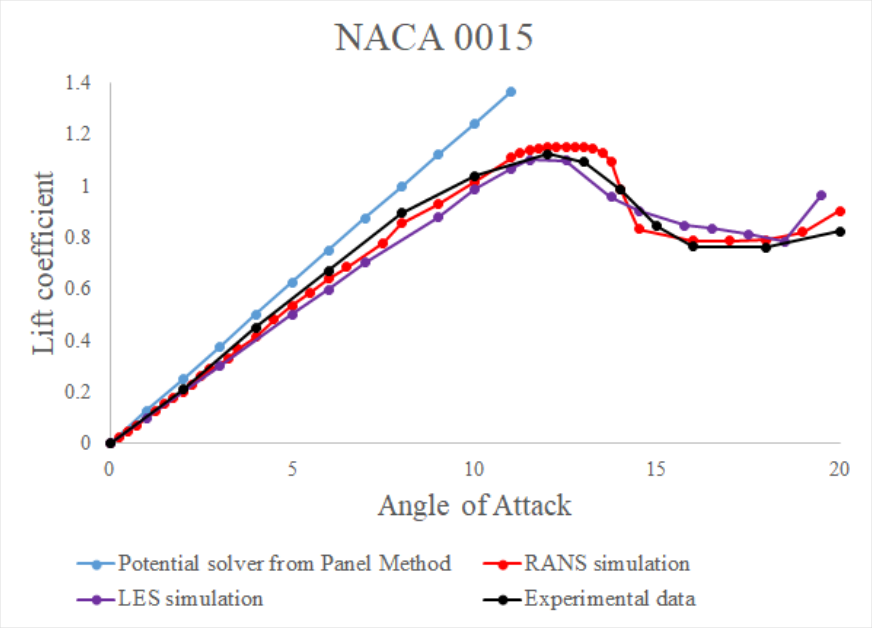

Figure 1.4: Comparison of lift coefficient of NACA 0015 airfoil

strategy of data treatment in different fidelities. The existing methods from other researchers are introduced in Section 1.4.

1.2.4 Kriging surrogate model

For the VF analysis and the surrogate model for the EGO, a Kriging model is used. The Kriging or Gaussian Process Regression(GPR), is a mathematical approximation which can calculate both estimated function value and estimation uncertainty [25]. The Kriging model assumes that a possible approximation model which passes exactly through the observed sample points follows a Gaussian process when it predicts/approximates an exact function.

Figure 1.5 shows an example of Gaussian process with the training set of five samples [26]. Solid lines in red, blue and green are realizable model fits which passes five observed sample points. As the Gaussian process is a random process, we have an infinite number of potential function approximations in function space, almost of which will be in the grey region with a

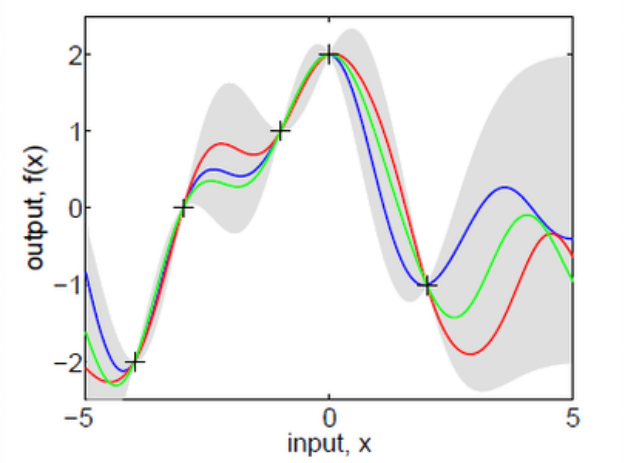

Figure 1.5: Example of Gaussian process with 5 samples

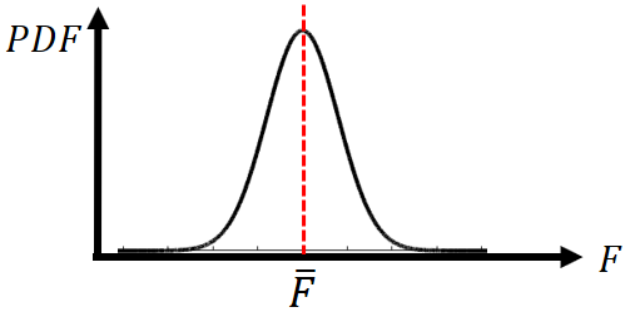

Figure 1.6: Probability density function of estimated function value

given confidence level. Therefore, considering the Gaussian process, an estimated function value of a certain input value can be obtained in form of probability density function which is shown in Figure 1.6.

In Figure 1.6, $\bar{F}$ is the mean value of the probability density function and we assume that this value is a predicted function value. The probability follows Gaussian normal distribution with variance σ^2, which represents estimation uncertainty. The variance value is related to the distance to observed sample points and its mathematical form includes a couple of hyper-parameters to determine. In Figure 1.5, the grey region is the region of $\bar{F} - 2\sigma$ to $\bar{F} + 2\sigma$, which is 95%, and the region increases (σ increases) as the location of function estimation

is far from the observed sample.

Hyper-parameters are unknown variables in the correlation function of the Kriging surrogate model. These unknown variables should be determined to construct the Kriging model, and the process of searching for the hyper-parameters is called Maximum Likelihood Estimation (MLE). In this process, the hyper-parameter is optimized to minimize the mean square error between the observed function value and estimated function value at the sample location. For the optimization process, derivative-based optimization such as Gauss-Seidel method, is generally used.

Aforementioned, the advantage of the Kriging model is that it offers both estimated function value and estimation uncertainty while other surrogate models gives only an estimated function value. The estimation uncertainty can be used in various ways. Since the estimation uncertainty is strongly related to the observed information, it can be used to quantify the global accuracy of surrogate model. Moreover, since it is in form of variance, if we have more than two surrogate models, using covariance, the relation between two surrogate models can be quantified as well. The detailed mathematical formulation of the Kriging model for single response is introduced in Section 2.1.

1.3 Scope of Research Work

In this study, two approaches were used to minimize the design cost while ensuring the accuracy of the design for Efficient Global Optimization process for a single- and multidisciplinary problems. The first approach is to save the cost of function evaluations needed to create a surrogate model. For this purpose, a new variable-fidelity analysis method has been developed. As introduced in the previous section, variable-fidelity analysis uses both a large number of low fidelity samples and a small number of high fidelity samples. Since the

data sets from different fidelity analysis method have discrepancies with each other, error estimation and calibration of lower fidelity samples are necessary. The method evaluates the error between low fidelity samples and high fidelity samples in terms of additive error and multiplicative error.

Multiplicative error terms are for the calibration of overall trend between two samples. For example, in Figure 1.4, the difference in slope of C_l-α curve can be easily corrected with multiplicative error term. Additive error term is for pointwise correction at each sample location. In Figure 1.4, at the high angle of attack, the overall trend of RANS, LES, and experimental data are similar. However, small discrepancies exist between the data sets, and it can be treated by additive error term. Two error terms are estimated through the sub-optimization process using Genetic Algorithm. Then, based on the error terms, lower fidelity samples can be calibrated as accurate as the highest fidelity sample set, and the entire sample set can be used together in the EGO design process. The detailed process and mathematical formulation is described in Section 2.2.

The second approach is to effectively limit the number of samples required for the design. It is an approach to reduce design costs by reducing the total number of samples required for design results by making only the necessary samples available in the right place in the design space. For this process, dynamic sampling technique is developed. Dynamic sampling consists of two sampling methods, which are filtering and infilling.

A sample filtering technique is related to the calibration process of variable fidelity samples in the first approach. Once the lower fidelity samples are calibrated, some samples can be inaccurately updated. In filtering process, these inaccurately calibrated low fidelity samples are filtered out in build a surrogate model correctly. Sample infilling technique is for the training of the surrogate model. In this study, a new strategy of infilling multiple points, which is Multi-Point Multi-Objective Infill Sampling Criteria (MPMO-ISC), is developed

to improve both global accuracy of the surrogate model and the local accuracy near the expected optimum. The main idea of MPMO-ISC is the effective utilization of the trade-off between exploration and exploitation through the multi-point infill sampling criteria. Using developed method, the global accuracy of the model and local accuracy around the optimum is parameterized, and multi-objective optimization is performed to select appropriate infilling sample set which can improve the surrogate model at the next design iteration both locally and globally. The details of dynamic sampling is introduced in Section 2.3.

To connect two design approaches, dynamic fidelity indicator is developed as well. Once the locations of additional samples are determined in infill sampling process, the fidelity of analysis method should be selected for the sample evaluation using variable-fidelity analysis. For the selection of the fidelity, dynamic fidelity indicator (DFI) using overlapping coefficient (OVL) is developed in this paper. Overlapping coefficient is the overlapped area between two probability density functions, and it gives us the evaluation of the agreement between two probability distribution. Since the prediction uncertainty can be provided in form of Gaussian distribution from Kriging surrogate model, based on this information, we can decide what fidelity method will be improve the surrogate model at the next design iteration efficiently. The mathematical formulation of OVL and DFI is described in Section 2.4.

Moreover, to extend the design method to the multidisciplinary design optimization (MDO) problem, multi-response Kriging surrogate model is developed. In MDO problems, multiple systems are strongly (or weakly) coupled to each other, and for the accurate design result, correlation between systems should be considered in the design process. To consider the correlation mathematically in surrogate modeling step, multi-response Kriging is introduced. For the tight coupling of different principles, Wang et al. and Kleijnen et al. suggested Gaussian Process Regression (GPR) of multiple response variables [27, 28]. Traditional Kriging model can construct a meta-model only for a single response which considers the

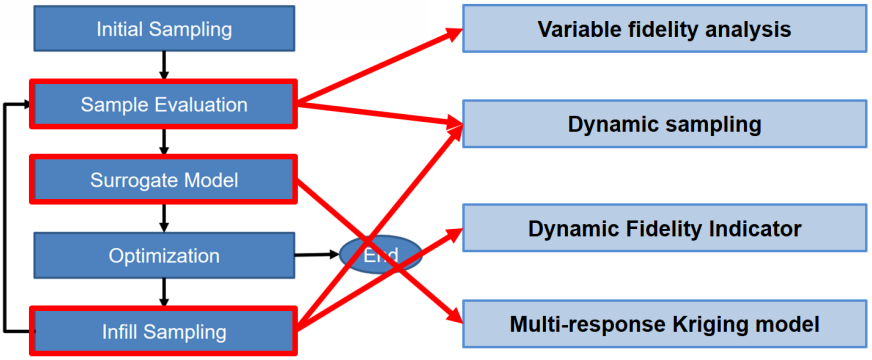

Figure 1.7: Developed design methods for Efficient Global Optimization

correlation between the locations of the observed samples. However, they added correlation terms which considers the coupling between different responses.

In this research, the multi-response Kriging models were improved with iterative method to estimate Maximum Likelihood (iMLE), which is an advanced Maximum Likelihood Estimation (MLE) process with large number of hyper-parameters. Since multi-response Kriging models from Wang and Kleijnen are considering the correlation between responses which are treated as unknown hyper-parameters, the number of hyper-parameters increases dramatically. As the number of unknown hyper-parameters increases, it can easily cause the numerical instability and reduce the chance to find the optimum hyper-parameter. The iMLE process helps to search the optimum hyper-parameters efficiently and accurately. The detail of mathematical formulation of multi-response Kriging model and iMLE is described in Section 3.1.

Figure 1.7 shows how the developed design method above was used at each stage in the EGO process. In the following sections, the previous study on these topics will be introduced and the key contribution of my research is be provided.

1.4 Literature Survey

1.4.1 Variable fidelity analysis and adaptive sampling

An approach of variable-fidelity analysis and design is effective in handling experiment and computation data as function analyses with different fidelities. Various research efforts on the variable-fidelity design have been made recently and are as follows.

The first approach is the CoKriging method. Using the CoKriging model [29], the surrogate model of an exact function can be constructed using both low and high fidelity samples. The covariance between low and high fidelity samples is defined to quantify the relations between the analyses of different fidelity [30]. Han et al. developed a variable-fidelity model by combining a direct gradient-enhanced Kriging(GEK) model and a bridge function [31]. Using this model, a global surrogate model for the aerodynamic coefficient and the drag polar of RAE2822 airfoil was constructed [30, 32]. Jo et al. developed the variable-fidelity Kriging model, where gradient values are calculated by the adjoint solution method, are directly utilized to improve the accuracy of the surrogate model [33]. The model is implemented for the design method of Efficient Global Optimization, and the unmanned combat air vehicle (UCAV) of the innovative control effector (ICE) [34, 35] has been designed for optimal shape of the control surface to maximize stability and controllability at given aerodynamic constraints [36].

Other approaches use the space mapping method which distorts the design space of low-fidelity analysis to match that of the high-fidelity function [37]. Linear and non-linear mapping algorithms have been developed by Bark et al. [38]. Robinson et al. developed a corrected space mapping method to solve the variable fidelity optimization with design variables defined over difference spaces [39]. They applied the method to a practical design

of bat wing. Leifsson et al. applied the method to the design of transonic airfoil involving lift and drag as multi-objectives [40].

The correction-based methods calibrate the low-fidelity model using a scaling function to make it as accurate as the high-fidelity function. Hafka et al. developed a multiplicative scaling function for the calibration [41] and the additive scaling function was developed by Choi et al. [42]. Combining these two scaling approaches, Gano et al. developed a method of a hybrid scaling function which can achieve further improvement in accuracy for the approximation of the high-fidelity function [43].

The current research is somewhat similar to the Gano's hybrid scaling method which uses both multiplicative and additive scaling terms to calibrate the lower fidelity samples. However, while Gano et al. calibrated the lower fidelity samples by the multiplicative terms first with the additive terms applied separately, and averaged two calibrated values through a weight function, two terms are applied simultaneously in the present work so that the multiplicative and additive error terms are more tightly correlated. In addition, the concept of sample point filtering is new in the present work, which was not found in the literature. It has been shown in the previous studies that if samples points which are incorrectly calibrated are directly included in the training set, they can mislead the surrogate model and contaminate the accuracy of the model. In this research, since the calibration is performed through the Kriging surrogate model which provides prediction uncertainty, the designer can evaluate the quality of the calibrated lower fidelity samples and determine whether the lower fidelity sample has been calibrated properly. Through this process, one can filter out incorrectly-calibrated samples, and enhance the quality of surrogate model using variable-fidelity samples of high accuracy only.

1.4.2 Sample infilling and dynamic fidelity indicator

Since Jones et al. suggested infill sampling criteria (ISC) [16] to add sample points efficiently and accurately in search of the global optima, several ISC methods are suggested. One of the most popular methods is based on the expected improvement (EI) and searches for additional samples by considering probabilities to find optimum and to reduce estimation uncertainty for the global accuracy. A generalized EI method is developed by Schonlau, and uses a parameter 'g' in the formulation of the EI function [44]. The parameter represents how much effort should be focused between global exploration and local exploitation. Sasena et al. suggested using a simulated annealing (SA) algorithm for the adaptation of the parameter 'g' [45].

Beside the EI method, Cox et al. suggested the concept of lower confidence bounding (LCB) for sequential and adaptive selection of the infill samples [46]. Kushner also suggested predicted improvement (PI) as the infill sampling criterion [47]. Those conventional ISC methods add only a single sample point per design iteration to update a surrogate model until the termination criteria of the design is satisfied.

The biggest drawback of these methods is the limit of the number of samples to add per design iteration. As the computer power and parallel computation capability advances rapidly, a number of function analyses can be performed simultaneously at a single design iteration. If multiple samples are selected and added to the training set, the total number of design iterations of the EGO is reduced, leading a huge cost saving in the design. The concept of multiple sample point selection has been proposed by numerous researchers. Viana et al. suggested the multiple sample point selection where high estimation uncertainty is predicted by the Kriging surrogate model [48]. Ginsbourger et al. derived the analytic formulation of the multi-point EI as an extension of a single EI method to a higher dimension [49]. They

pointed out that the highly expensive computational method such as the Monte-Carlo simulation is needed to calculate the analytic form of the multi-point EI, where the computational cost is considerably high. As an alternative to the analytic form of the multi-point EI, they proposed a concept of an approximate multi-point EI (q-EI) based on a Kriging believer (KB) and a constant liar (CL) [49, 50]. The method uses functional response of the Kriging surrogate model for the determination of accuracy.

As another approach, Feng et al. and Yi et al. suggested a method which formulates a multi-objective optimization problem where the local exploitation and the global exploration are a separate objective of the sub-optimization problem [51, 52]. The additional samples are selected from the Pareto front of multi-objective sub-optimization at each design iteration adaptive to the designer's intent on the two types of the accuracy. In the present study, additional criteria to determine how to select additional samples in the Pareto front were developed and applied to the EGO with the VF analysis.

To make a decision on the fidelity of the function evaluation for the additional samples, Jo et al. developed a Bayesian based dynamic fidelity indicator (DFI) to probabilistically determine the required fidelity of function analysis for any design candidate in design space [53]. Moreover, Han et. al. developed a method of the variable-fidelity EI as one of variations of the standard EI method and considers the probability of the level of fidelity [30].

1.4.3 Multi-Response Kriging model for multidisciplinary problems

Precise analysis of multiple disciplines, including aerodynamics, structures, controls, and thermodynamics, during the early design stages are critical to the accuracy and reliability of the final design at a reduced cost. For example, aircraft wing structure can be deformed

under the aerodynamic loading [54] at certain flight conditions, and the aeroelastic analysis to account for the tight coupling between aerodynamic and structural characteristics of the wing needs to be integrated early in the preliminary design..

In the multidisciplinary design optimization (MDO) process, several design objectives representative of different sub-disciplines, can be considered. For instance, if the aspect ratio of the wing increases, lift to drag ratio of the wing increases by reduced induced drag [20]. However, the increased span length makes a high aspect ratio wing experience higher bending stress, which then, produces larger deformation. Since both lift to drag ratio and the deformation are the function of aspect ratio, the coupling interface or correlation needs to be well resolved.

Simpson et al. used the Kriging model for multidisciplinary design optimization of aerospike nozzle [55]. The thrust, weight of engine, and gross lift-off weight (GLOW) of the aircraft were set as objective functions, and the Kriging model was constructed separately for an individual objective. However, the coupling of the objective functions was not modeled explicitly through the surrogate model because they were built independently without modeling any mathematical relations between the model outputs. To mathematically model the coupling of the sub-disciplinary objectives, Bowcutt used a new objective which includes the effect of different sub-disciplines. For the multidisciplinary optimization of air breathing hypersonic vehicle with aerodynamics, propulsion, stability, controllability, and mass property of the aircraft fully considered in the design, he used the design objective function of maximizing flight range [56]. Constructing the surrogate model of flight range, he could mildly couple the effects of multiple disciplines in one surrogate model. However, using this approach, a designer cannot determine the coupling degree among all disciplines and an individual discipline stays as a black-box function analysis.

To overcome this problem, a multi-response Kriging (MRK) model has been studied by

researchers. The MRK considers covariance between the function responses of different disciplines and construct the model in the consideration of the coupling of those. We can divide multi-response Kriging into two types.

First, CoKriging model is a Gaussian process regression(GPR) method which provides simultaneously the predictions of multiple output responses that may be potentially correlated with its accuracy typically higher than that from the two independent single response Kriging models. The multi-variate output responses can be predicted by a linear combination of all observed function responses [14]. Covariance between responses is expressed as a closed form of function of observed outputs [57].

If a gradient value is available at the sampling location as well as a function value, the accuracy of the surrogate model becomes higher than when the function values are used alone for the model construction. Since the gradient value is strongly correlated in mathematics with the function value, the CoKriging model is ideal to utilize gradient values into the model. Chung et al.[58] developed the CoKriging model which takes into account gradient information in addition to the function value and improved the accuracy and efficiency of the Kriging model for high-dimensional design problem of low-boom supersonic jets. Forrester et al. and Yamazaki et al. introduced a gradient- and Hessian-enhanced Kriging model, respectively, and employed gradient or Hessian information as a second set of basis functions in the Kriging model [59, 60]. Laurenceau used the Gradient-enhanced Kriging model to build the response surface of aerodynamic functions, and the improvement in global accuracy of the model was demonstrated in comparison to the ordinary Kriging model [61].

While the CoKriging model calculates the covariance between responses as a function of observed output responses, there are attempts to define the covariance between output responses as unknown hyper-parameters which are determined by Maximum Likelihood Estimation (MLE). Neal suggested a single hyper-parameter, which represents noise variance,

for all covariances between output responses. However, this method is not be sufficient to account for the correlation of multiple outputs [62]. Wang et al developed a multiple response Kriging method to jointly model the quantile with a correlated and less-noisy expectation to improve the accuracy of the model and predictions from the quantile meta-model [63]. Conti et al. suggested a separable multiple response Gaussian Process(GP) model which is an extended model of the single-output Bayesian model [64, 65]. Ver Hoef et al. developed a multi-response GP model with the convolution model [66], and Goulard et al. proposed the model with the linear model of co-regionalization(LMC) [67]. Alvarez et al. introduced a multiple-output GP model using a dependent-output GP model constructed through the convolution formalism [68].

Wang et al developed a GPR model with multiple response variables by assuming that the covariance of multi-response is the nominal uni-output covariance multiplied by the covariances between different outputs [27]. This approach can handle a training sample set of multiple output responses which may not be necessarily observed at the same design locations. Hong et al. extended Wang's approach to have heteroscedastic and correlated noises terms [69, 70]. Kleijnen et al. proposed a multivariate Kriging meta-model for multiple output responses with a non-separable dependent covariance structure [28]. The method requires the same number of output responses at any sampling location in design space, and covariance of multiple responses are modelled across any sample points in the form of correlation function. Using the Kleijnen's multivariate Kriging meta-model, Sadoughi et al. proposed multivariate system reliability analysis (MSRA) for complex engineered systems with highly nonlinear and dependent components that are connected in series, parallel, and mixed configurations [71].

However, multi-response Kriging model by Wang and Kleijnen has difficulties in searching proper hyper-parameters. Since the covariance between output responses are treated as un-

known hyper-parameters, the number of unknown hyper-parameters hugely increases. As the number of unknowns increases, the maximum likelihood estimation process using derivative-based optimization became a tough problem due to numerical uncertainty. In this paper, to overcome this problem, iterative method to search maximum likelihood is developed to search the hyper-parameters correctly and stably.

1.5 Contribution

Contributions of the research are several. The variable fidelity analysis is effective in complex design problems, as a large number of low- to medium-fidelity analysis replace expensive high fidelity analyses, enabling extensive search of the design space. The error approximation and calibration of the lower-fidelity analyses are formulated with a great scalability to include a large hierarchy of function fidelity.

The biggest merit is the dynamic sampling strategy based on the mathematical formulations of filtering criterion and infilling criterion. It identifies sample points of lower accuracy in the design space and identify regions in the design space where additional sample points are needed to improve the local accuracy effectively and dynamically. A required analysis fidelity for the infill samples is determined mathematically by the fidelity indicator. Since the fidelity indicator is derived in reference to the probability distribution function (PDF) of the variable fidelity surrogate model which also being updated over the design iterations, we defined it as dynamic fidelity indicator (DFI). The approaches of the adaptive sampling and the fidelity indication are easily extended to the large hierarchy of the variable analysis.

Using multi-response Kriging model, the physical coupling between different disciplines can be modeled mathematically. In case of using single response Kriging for different discipline, we would lose the information of coupling between disciplines, which would be very significant

information in MDO. Using multi-response Kriging model, without the loss of information, much more accurate surrogate model can be constructed with less number of samples, and it will improve both accuracy of the optimum and cost efficiency of the design.

From the validations and design applications, it is verified that using developed methods the design cost can be hugely saved while the design result is same or better than the existing methods. Applying developed variable-fidelity analysis, dynamic sampling technique, and dynamic fidelity indicator into Efficient Global Optimization process, the design cost is saved up to 45%. Especially, comparing developed infill sampling strategy with existing method of Q-EI, the required number of samples for the design is reduced up to 55%, which is a remarkable progress. Moreover, the multi-response Kriging model provided similar global accuracy of single response Kriging with about 50% reduced number of samples. The details of the validations and design applications is described in Chapter 4 and Chapter 5.

Chapter 2

Single Discipline Optimization

In this chapter, three developed design methods for single discipline Efficient Global Optimization (EGO) problem will be introduced; variable-fidelity analysis, dynamic sampling and dynamic fidelity indicator (DFI), which are the first three developed design methods in Figure 1.7. First of all, single response Kriging surrogate model, which will be used for the surrogate model in EGO process and variable-fidelity analysis, is introduced with mathematical details. Using Kriging model, newly developed variable-fidelity analysis method will be introduced. In this method, the samples in different fidelities will be calibrated to have same fidelity, so that the samples can be used together without discrepancy.

To use the sample efficiently, dynamic sampling technique is introduced. Dynamic sampling includes both filtering and infilling samples. In a filtering process, inaccurately calibrated samples are filtered out to avoid inaccuracy in surrogate modeling. In an infilling process, the number and location of additional samples for training of the surrogate model is selected. Once the samples are selected in the infilling process, dynamic fidelity indicator select the fidelity of sample in the next design iteration. At the end of the chapter, variable-fidelity EGO framework, which is the combination of EGO process and developed design methods, will be provided.

2.1 Kriging Surrogate Model

In this section, Kriging model, which is also called Gaussian Process Regression (GPR) model, is introduced. Kriging is a method of interpolation with observed sample values which is modeled by a Gaussian process governed by prior covariances. [14] A Gaussian process (GP) is a realization process of random variables of which have a joint Gaussian distribution [25]. This process can be specified by the mean function $\mu(\boldsymbol{x})$ and covariance function $c(\boldsymbol{x}, \boldsymbol{x'})$ of a real process $f(\boldsymbol{x})$ as below,

$$\begin{aligned} \mu(\boldsymbol{x}) &= E[f(\boldsymbol{x})] \\ c(\boldsymbol{x}, \boldsymbol{x'}) &= E[(f(\boldsymbol{x}) - \mu(\boldsymbol{x}))(f(\boldsymbol{x'}) - \mu(\boldsymbol{x'}))] \end{aligned} \tag{2.1}$$

where $\boldsymbol{x}$ is made up of p-dimensional input covariates, $\boldsymbol{x} = [x_1, x_2, \cdots, x_p]^T$. The Gaussian process can be written as

$$f(\boldsymbol{x}) \sim G(\mu(\boldsymbol{x}), c(\boldsymbol{x}, \boldsymbol{x'})) \tag{2.2}$$

The GPR or Kriging model is a meta-model for which a function values are estimated by a Gaussian process [72]. Using linear regression, the observed response variable y can be expressed as a function of covariates and a regression parameter $\boldsymbol{w} = [w_1, w_2, \cdots, w_p]^T$.

$$y_i = \boldsymbol{x}_i^T \boldsymbol{w} + \epsilon_i, \;\; i = 1, 2, \cdots, n, \tag{2.3}$$

where n is the number of observed data points, and ϵ is additive Gaussian noise with zero mean and unknown variance σ_ϵ^2. The ordinary GPR model sets the mean of response variable

y as zero. Under the Bayesian update approach, a prior distribution of the model needs to be assumed. In the regression model, the regression parameter $\boldsymbol{w}$ will be assumed to follow a Gaussian distribution with zero mean and covariance σ_w^2 which is independent of ϵ_i as below.

$$\boldsymbol{w} \sim G(\mathbf{0}, \sigma_w^2 \boldsymbol{I}_p) \tag{2.4}$$

where $\boldsymbol{I}_p$ is $p \times p$ identity matrix.

Now, for a trial location $\hat{\boldsymbol{x}} \in \mathbb{R}^p$ which has the estimated function value $\hat{y}$, the joint probability distribution of observed data augmented by $\hat{\boldsymbol{x}}$ and $\hat{y}$ can be used to evaluate the Gaussian process posterior distribution at $\hat{\boldsymbol{x}}$ [73].

$$\begin{bmatrix} \boldsymbol{y} \\ \hat{y} \end{bmatrix} \sim G\left(\mathbf{0}, \begin{bmatrix} \boldsymbol{C}(\boldsymbol{x_i}, \boldsymbol{x_j}) & \boldsymbol{C}(\boldsymbol{x_i}, \hat{\boldsymbol{x}}) \\ \boldsymbol{C}(\hat{\boldsymbol{x}}, \boldsymbol{x_i}) & \boldsymbol{C}(\hat{\boldsymbol{x}}, \hat{\boldsymbol{x}}) \end{bmatrix} \right) \quad i, j = 1, 2, \cdots, n, \tag{2.5}$$

where $\boldsymbol{y} = [y_1, y_2, \cdots, y_n]^T$ is a vector of the observed response variable, and $\boldsymbol{C}$ is a covariance matrix. Since there are n number of $\boldsymbol{x_i}$ and $\boldsymbol{x_j}$ vectors corresponding to n number of observed data points, the size of $\boldsymbol{C}(\boldsymbol{x_i}, \boldsymbol{x_j})$ matrix is $(n \times n)$. The size of $\boldsymbol{C}(\boldsymbol{x_i}, \hat{\boldsymbol{x}})$ is $(n \times 1)$, and $\boldsymbol{C}(\hat{\boldsymbol{x}}, \boldsymbol{x_i})$ is transpose matrix of $\boldsymbol{C}(\boldsymbol{x_i}, \hat{\boldsymbol{x}})$. The size of $\boldsymbol{C}(\hat{\boldsymbol{x}}, \hat{\boldsymbol{x}})$ matrix is (1×1). The elements of the $\boldsymbol{C}$ matrix can be obtained by calculating the expected covariance. For two observed data points, $\boldsymbol{x}_i$ and $\boldsymbol{x}_j$, the covariance between two data can be calculated as below,

$$\begin{aligned} C_{ij} = c(\boldsymbol{x}_i, \boldsymbol{x}_j) &= Cov[y_i, y_j] = E\left[(y_i - E[y_i]) (y_j - E[y_j]) \right] \\ &= \sigma_w^2 \boldsymbol{x}_i^T \boldsymbol{x}_j + \delta_{ij} \sigma_\epsilon^2 \end{aligned} \tag{2.6}$$

where δ_{ij} is the delta function; if $i = j$, $\delta_{ij} = 0$, and if $i \neq j$, $\delta_{ij} = 1$. In Eq. (2.6), the

covariance is a function of σ_w^2, the variance of prior probability. Since the observation of $\boldsymbol{y}$ and the estimated function value of $\hat{y}$ are connected by the joint probability in Eq. (2.5), using Gaussian identities, the posterior probability, which is the conditional probability of $\hat{y}$ for given data $\boldsymbol{y}$ can be calculated as below,

$$\begin{aligned} p\left(\hat{y}|\boldsymbol{y}\right) &= G\left(\mu(\hat{y}), \sigma^2(\hat{y})\right) \\ \mu(\hat{y}) &= \boldsymbol{C}(\hat{\boldsymbol{x}}, \boldsymbol{x_i})\boldsymbol{C}^{-1}(\boldsymbol{x_i}, \boldsymbol{x_j})\boldsymbol{y} \\ \sigma^2(\hat{y}) &= \boldsymbol{C}(\hat{\boldsymbol{x}}, \hat{\boldsymbol{x}}) - \boldsymbol{C}(\hat{\boldsymbol{x}}, \boldsymbol{x_i})\boldsymbol{C}^{-1}(\boldsymbol{x_i}, \boldsymbol{x_j})\boldsymbol{C}(\boldsymbol{x_i}, \hat{\boldsymbol{x}}) \end{aligned} \tag{2.7}$$

where $\mu(\hat{y})$ is the mean of $\hat{y}$ which is the estimated function value of a trial location $\hat{\boldsymbol{x}}$, and $\sigma^2(\hat{y})$ is estimation uncertainty.

Instead of inferring parameter $\boldsymbol{w}$, the regression model can be summarized by several forms of the covariance function, which are related to $\boldsymbol{C}$ matrix. The covariance function below is one of an example form which is gamma exponential function [74].

$$\begin{aligned} C_{ij} &= \prod_{k=1}^{p} C_k\left(\theta, \gamma, x_{ik} - x_{jk}\right) \\ C_k &= \exp\left(-\theta_k \left|x_{ik} - x_{jk}\right|^{\gamma}\right), \ 0 < \gamma \leq 2 \end{aligned} \tag{2.8}$$

Since k varies from 1 to p, there are $(p+1)$ unknown variables, which are θ_k and γ. These parameters are called hyper-parameters. Assuming a Gaussian process, the optimal hyper-parameters of the covariance function can be determined using optimization process, which called Maximum Likelihood Estimation (MLE) [75]. The MLE problem is defined below.

$$\min_{\theta,\gamma} \left\{ \psi(\theta,\gamma) \equiv |\boldsymbol{C}(\boldsymbol{x_i},\boldsymbol{x_j})|^{1/n} \sigma_w^2 \right\} \tag{2.9}$$

where $|\boldsymbol{C}(\boldsymbol{x_i},\boldsymbol{x_j})|$ is the determinant of $\boldsymbol{C}(\boldsymbol{x_i},\boldsymbol{x_j})$.

2.2 Variable Fidelity Analysis

In practical design, we are able to obtain samples with various analyses in different fidelities. For instance, in the design of airfoil, Vortex panel, Euler, and RANS analysis methods are considerable aerodynamic analysis methods. However, the samples from different fidelity analyses cannot be used together to make a surrogate model since lower fidelity data includes errors due to the lack of knowledge compared to higher fidelity data. Therefore, the errors between different fidelity samples need to be estimated, and lower fidelity samples should be calibrated with the estimated errors to equivalent fidelity with the highest fidelity sample set.

For the error estimation between different fidelity sample data, two assumptions are made as below,

Assumption 1. The data from the highest fidelity analysis method is the most reliable data.

Assumption 2. The sets of data in different fidelities are correlated.

To calculate the errors, we need a reference data which can be compared with lower fidelity data. Since the highest fidelity data is the most accurate data which we can achieve at the current stage, we are able to assume that the highest fidelity data can be used as exact reference. Moreover, if lower fidelity data is not well-correlated with the highest fidelity

data, we have no reason to use corresponding low fidelity data set. Since different fidelity analysis methods are describing same physics, they should be correlated to each other data set. In conclusion, prior to the variable-fidelity data analysis, the different fidelity analysis methods should be validated if they are describing the real physics well.

If we define the hierarchy of the function fidelity by m, where $m = 1, 2, \cdots, r$, with the higher index representing the higher fidelity, the function value analyzed by the mth fidelity method at $\boldsymbol{x_i}$ are written as $f_m(\boldsymbol{x_i})$, where $i \in \mathcal{I}_m^{(k)}$. The superscript (k) indicates the design iteration number. The set of indices for all sample points at (k)th design iteration can be denoted as $\mathcal{I}^{(k)}$ and consist of the subsets of $\mathcal{I}_m^{(k)}$, i.e., $\mathcal{I}^{(k)} = \mathcal{I}_1^{(k)} \cup \mathcal{I}_2^{(k)} \cup \cdots \cup \mathcal{I}_r^{(k)}$. Then, the set of entire sample points are defined as $\mathcal{F}^{(k)}$ at the (k)th design iteration,

$$\mathcal{F}^{(k)} = \{f_m(\boldsymbol{x_i}) \mid i \in \mathcal{I}_m^{(k)}, \text{ for } m = 1, 2, \cdots, r\} \tag{2.10}$$

Based on the observed sample points, a series of single-fidelity Kriging surrogate model for lower fidelity sample sets (except for the highest fidelity sample set) are constructed as shown below,

$$\begin{aligned} \hat{f}_m^{(k)}(\hat{\boldsymbol{x}}) &= KRG(\{f_m(\boldsymbol{x_i}) \mid i \in \mathcal{I}_m^{(k)}\}) \ , m = 1, 2, \cdots, r-1 \\ \bar{f}_m^{(k)}(\hat{\boldsymbol{x}}) &= \mu\left(\hat{f}_m^{(k)}(\hat{\boldsymbol{x}})\right) \end{aligned} \tag{2.11}$$

where KRG represents the Kriging interpolation function constructed with the sample set in the bracket. $\bar{f}_m^{(k)}(\hat{\boldsymbol{x}})$ represents the mean value of Kriging estimation $\hat{f}_m^{(k)}$ at arbitrary design location of $\hat{x}$. Then, the errors between the highest-fidelity and the lower-fidelity analyses can be estimated from the Kriging model of an individual fidelity analysis.

In this paper, the estimated function value of $\bar{f}_m^{(k)}$ and $\bar{f}_{m+1}^{(k)}$ are related by additive and multiplicative errors of α_m and $\beta_m(:)$, respectively, at the sample locations of highest-fidelity analysis (for $\boldsymbol{x}_i$, where $i \in \mathcal{I}_r^{(k)}$).

$$\begin{aligned}
\bar{f}_1^{(k)}(\boldsymbol{x}_i) &= \alpha_1 \bar{f}_2^{(k)}(\boldsymbol{x}_i) + \beta_1(\boldsymbol{x}_i), \ i \in \mathcal{I}_r^{(k)} \\
\bar{f}_2^{(k)}(\boldsymbol{x}_i) &= \alpha_2 \bar{f}_3^{(k)}(\boldsymbol{x}_i) + \beta_2(\boldsymbol{x}_i), \ i \in \mathcal{I}_r^{(k)} \\
&\vdots \\
\bar{f}_{r-1}^{(k)}(\boldsymbol{x}_i) &= \alpha_{r-1} f_r^{(k)}(\boldsymbol{x}_i) + \beta_{r-1}(\boldsymbol{x}_i), \ i \in \mathcal{I}_r^{(k)}
\end{aligned} \tag{2.12}$$

The multiplicative error of α_m represents the overall ratio between two Kriging models of $\hat{f}_m^{(k)}$ and $\hat{f}_{m+1}^{(k)}$ whereas the additive error $\beta_m(:)$ accounts for the pointwise difference between function approximations of $\hat{f}_m^{(k)}$ and $\hat{f}_{m+1}^{(k)}$ at the location of the highest-fidelity analysis. Since the errors are estimated at the sample location of the highest fidelity data set($i \in \mathcal{I}_r^{(k)}$), we know the exact function value $f_r^{(k)}(\boldsymbol{x}_i)$. For other fidelities, since we will not have the same sample point with the highest fidelity data set, the prediction value from Kriging model $\bar{f}_m^{(k)}(\boldsymbol{x}_i)$ $(m = 1, 2, \cdots, r-1)$ is used.

To calculate α_m and $\beta_m(:)$, Eq. (2.12) is re-written in matrix form for $\boldsymbol{x}_i$ where $i \in \mathcal{I}_r^{(k)}$. For example, with three different fidelity methods ($r = 3$), the equation can be written as Eq. (2.13) and is arranged for the vector of additive errors of $\beta_1(\boldsymbol{x}_i)$ and $\beta_2(\boldsymbol{x}_i)$.

$$\begin{bmatrix} \beta_1(\boldsymbol{x}_i) \\ \beta_2(\boldsymbol{x}_i) \end{bmatrix} = \begin{bmatrix} I & \alpha_1 I \\ 0 & I \end{bmatrix}^{-1} \begin{bmatrix} \bar{f}_1^{(k)}(\boldsymbol{x}_i) - \alpha_1 \alpha_2 f_3(\boldsymbol{x}_i) \\ \bar{f}_2^{(k)}(\boldsymbol{x}_i) - \alpha_2 f_3(\boldsymbol{x}_i) \end{bmatrix}, \ i \in \mathcal{I}_r^{(k)}, \tag{2.13}$$

where the size of the identity matrix I is $|\mathcal{I}_r^{(k)}|$. For this equation, the sub-optimization problem is solved for α_k to minimize the l_2 norm of the additive errors of $[\beta_1(\boldsymbol{x}_i), \beta_2(\boldsymbol{x}_i)]^T$. The generalize form of sub-optimization can be written as below. For the optimization,

Genetic Algorithm(GA) is used [10].

$$\begin{aligned} &\text{minimize} && |[\beta_1(\boldsymbol{x}_i), \beta_2(\boldsymbol{x}_i), \cdots, \beta_{r-1}(\boldsymbol{x}_i)]^T| \\ &\text{w.r.t} && \alpha_1, \alpha_2, \cdots, \alpha_{r-1} \\ &\text{subject to} && i \in \mathcal{I}_r^{(k)} \end{aligned} \tag{2.14}$$

This process is equivalent to scaling lower fidelity models by α_m to the highest fidelity model to have minimum additive errors. The optimum additive error is represented by $\alpha_1^*, \alpha_2^*, \cdots, \alpha_{r-1}^*$. Once we obtained multiplicative errors from the optimization process, additive errors at the location of the highest fidelity sample set can be calculated, which are $\beta_1^*(\boldsymbol{x}_i), \beta_2^*(\boldsymbol{x}_i), \cdots, \beta_{r-1}^*(\boldsymbol{x}_i)$, where $i \in \mathcal{I}_r^{(k)}$. For three fidelity models case, Eq. (2.13) can be directly used for the calculation of additive errors. Using the calculated additive errors, the Kriging surrogate model of additive errors is created for each fidelity m as $\hat{\beta}_m$, and represented as

$$\hat{\beta}_m^*(\hat{\boldsymbol{x}}) = KRG(\{\beta_m^*(\boldsymbol{x}_i) \mid i \in \mathcal{I}_r^{(k)}\}), \text{ for } m = 1, 2, \cdots, r-1. \tag{2.15}$$

The approximated errors are used to calibrate the lower-fidelity samples based on the equation of the error statement, Eq. (2.12). In this paper, the calibrated sample is represented as $f_m'(\boldsymbol{x}_i)$, where $i \in \mathcal{I}_m^{(k)}$ for $m = 1, 2, \cdots, r-1$. With three different fidelity analyses, for example, two lower fidelity samples of $f_1(\boldsymbol{x}_i)$ and $f_2(\boldsymbol{x}_j)$ are calibrated to be $f_1'(\boldsymbol{x}_i)$ and $f_2'(\boldsymbol{x}_j)$, where $i \in \mathcal{I}_1^{(k)}$ and $j \in \mathcal{I}_2^{(k)}$ with corresponding errors of α_m^* and $\hat{\beta}_m^*$.

$$\begin{aligned} f_1'(\boldsymbol{x}_i) &= \frac{f_1(\boldsymbol{x}_i) - \hat{\beta}_1^*(\boldsymbol{x}_i) - \alpha_1^* \hat{\beta}_2^*(\boldsymbol{x}_i)}{\alpha_1^* \alpha_2^*}, i \in \mathcal{I}_1^{(k)} \\ f_2'(\boldsymbol{x}_j) &= \frac{f_2(\boldsymbol{x}_j) - \hat{\beta}_2^*(\boldsymbol{x}_j)}{\alpha_2^*}, \ j \in \mathcal{I}_2^{(k)} \end{aligned} \tag{2.16}$$

2.3 Dynamic and Adaptive Sampling Method

Dynamic sampling consist of two sampling techniques, which are filtering and infilling. Sample filtering is for the variable fidelity analysis. It filters out incorrectly calibrated lower samples in the set of lower fidelity sample data before using with high fidelity sample set. This process can prevent irregular distortion in variable-fidelity Kriging model, which is constructed with calibrated lower fidelity samples and high fidelity samples. Sample infilling process is for general Efficient Global Optimization process. It is for the selection of additional samples for the training of surrogate model through the design iteration. The details of two sampling techniques are provided in following sections.

2.3.1 Filtering low-accuracy samples

Even though we calibrated the lower-fidelity sample to be accurate as the highest fidelity sample, some of the calibrated samples can be inaccurate to be used with the highest fidelity sample. One of the reason for the inaccuracy is for the small number of high fidelity samples at the early design stage. In variable-fidelity analysis, to reduce the cost as much as possible, the initial number of the highest fidelity sample, which will have the highest cost as well, is restricted to be small. Since the calibration is performed based on the high fidelity sample points, if we do not have sufficient information, the calibration can be inaccurate.

The second reason is related to the uncertainty from Kriging estimation. As the additive error terms in Eq. (2.15) and (2.16) are predicted by the Kriging surrogate model which uses a Gaussian kernel, calibrated lower-fidelity sample points of $f'_m(\boldsymbol{x}_i)$, where $i \in \mathcal{I}_m^{(k)}$ for $m = 1, 2, \cdots, r-1$, follow the Gaussian probability distributions of the $\hat{\beta}_m$. Since we have the probability distribution of calibrated function value rather than the exact value, we cannot guarantee that the mean of $f'_m(\boldsymbol{x}_i)$ will be correctly calibrated function value if the

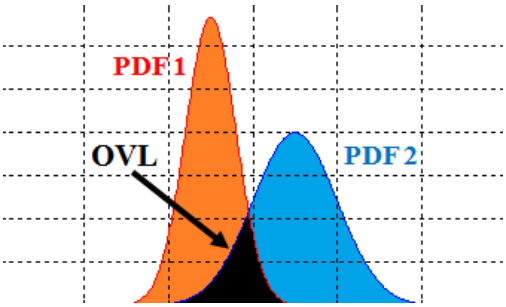

Figure 2.1: OVL coefficient between two probability functions

variance of the probability distribution is large.

Therefore, low-fidelity sample points having insufficient accuracy should be filtered out based on a probabilistic filtering criterion (FC). In this paper, the FC is defined by the overlapping coefficient (OVL) [76] which indicates how closely the two probability distribution functions(PDFs) agrees and is computed by the area of the overlapped PDFs, as illustrated in Figure 2.1.

The FC compares the PDFs of calibrated lower-fidelity sample points $f'_m(\boldsymbol{x}_i)$, where $i \in \mathcal{I}_m^{(k)}$ for $m = 1, 2, \cdots, r-1$, and Kriging prediction of the highest-fidelity sample points at the location of lower-fidelity sample point $(\hat{f}_r(\boldsymbol{x}_i))$, where $i \in \mathcal{I}_m^{(k)}$ for $m = 1, 2, \cdots, r-1$. If the OVL coefficient is less than a threshold value, 0.5 for example in the present study, then the corresponding low-fidelity sample point is filtered out. The set of indices of the filtered low-fidelity sample points becomes

$$\begin{aligned} \mathcal{I}_m^{-(k)} =& \{i \mid OVL(f'_m(\boldsymbol{x}_i), \hat{f}_r(\boldsymbol{x}_i)) < 0.5, i \in \mathcal{I}_m^{(k)}\} \\ \mathcal{I}^{-(k)} =& \mathcal{I}_1^{-(k)} \cup \mathcal{I}_2^{-(k)} \cup \cdots \cup \mathcal{I}_{r-1}^{-(k)} \text{ for } m = 1, 2, \cdots, r-1, \end{aligned} \tag{2.17}$$

where a function of $OVL(x_1, x_2)$ [76] is defined as the OVL coefficient for two random variates of x_1 and x_2 with the PDFs of $pdf(x_1)$ and $pdf(x_2)$, respectively,

$$OVL(x_1, x_2) = \int_{R_n} \min\left[pdf(x_1), pdf(x_2)\right] dx \tag{2.18}$$

where R_n is the range of sample values which is decided based on the standard derivation of the Kriging estimation.

As the calibrated lower-fidelity sample points are compared with Kriging predictions from the highest fidelity analysis alone, the filtering process becomes relatively sensitive to the accuracy of the highest fidelity Kriging model and a threshold value, which is set as 0.5 in this paper. To resolve this issue, the filtered-out lower fidelity sample set $\mathcal{I}^{-(k)}$ is re-considered in the following $(k+1)$th design iteration while the highest fidelity samples keep added through infilling additional sample points, and the highest fidelity Kriging model keeps being improved in accuracy. Moreover, the sensitivity of design results with respect to a varying OVL value is shown in Sec 4.2.

Once the sample point filtering is carried out, we have sets of lower fidelity samples which are correctly calibrated. Since these data set have same or similar fidelity with the highest fidelity samples, we can make a data set for variable fidelity Kriging, by integrating the data set with the highest fidelity samples. The indices of data set for variable fidelity Kriging at (k)th design iteration can be defined as below,

$$\begin{aligned} \mathcal{I}_{VF}^{(k)} =& \mathcal{I}^{(k)} - \mathcal{I}^{-(k)} \\ =& \left(\mathcal{I}_1^{(k)} - \mathcal{I}_1^{-(k)}\right) \cup \left(\mathcal{I}_2^{(k)} - \mathcal{I}_2^{-(k)}\right) \cup \cdots \cup \left(\mathcal{I}_{r-1}^{(k)} - \mathcal{I}_{r-1}^{-(k)}\right) \cup \mathcal{I}_r^{(k)} \end{aligned} \tag{2.19}$$

Now, the variable fidelity Kriging surrogate model can be constructed from the sets of $\mathcal{I}^{VF(k)}$, as follows,

$$\hat{f}_{VF}(\hat{\boldsymbol{x}}) = KRG(\ \{f_r(\boldsymbol{x}_i) \mid i \in \mathcal{I}_r^{(k)}\} \cup \{f'_m(\boldsymbol{x}_j) \mid j \in \mathcal{I}_m^{(k)} \backslash \mathcal{I}_m^{-(k)} \text{ for } m = 1, 2, \cdots, r-1\}). \tag{2.20}$$

2.3.2 Infilling samples for single fidelity optimization

As the accuracy and computational efficiency of the Efficient Global Optimization(EGO) greatly depend on the performance of the infill sampling criteria (ISC), various types of ISC have been proposed and used. One of the most popular ISC is the EI [44] which literally represents an expected value of improvement, where the improvement is defined as difference between a predicted minimum and the true minimum found so far and is considered as a random variable following a Gaussian normal distribution of $G(\bar{f}, \sigma_f^2)$. The mathematical formulation of the EI is represented in closed form as in Eq. (2.21).

$$\mathrm{EI}(\boldsymbol{x}) = \begin{cases} \overbrace{\left(\mathbb{F}_{min} - \bar{f}\right) \Phi\left(\frac{\mathbb{F}_{min} - \bar{f}}{\sigma_f}\right)}^{A} + \overbrace{\sigma_f^2 \phi\left(\frac{\mathbb{F}_{min} - \bar{f}}{\sigma_f}\right)}^{B}, & \sigma_f > 0 \\ 0, & \sigma_f = 0 \end{cases} \tag{2.21}$$

The first term of the right-hand-side of Eq. (2.21) denoted as A represents the probability to find the smaller minimum than the current minimum $\mathbb{F}_{min}$ (exploitation) and the second term of B indicates the probability to find the high estimation uncertainty (exploration) [77, 78]. To find the maximum EI point is a single objective optimization problem where two objectives of exploitation and exploration are summed with weights represented by cumulative density function and probability density functions. The mathematical form is shown in Eq. (2.21). Throughout the adaptive sampling process of the EGO method, the ratio of the terms A

and B varies. The term B is larger than A at the beginning of the design iterations and the term A grows larger when the ISC focus on searching the minimum.

A potential problem of the EI-based ISC method is that the additional point may be trapped in around the local minimum incumbent at each iteration. If the sample points are clustered with proximity to one other, the method of regression and re-interpolation of the Kriging model are used to avoid ill-conditioning of the correlation matrix. Moreover, since only one additional sample is selected, designer cannot use the advantage of parallel computing, and the number of design iteration increases (which will lead the increase of design cost as well). To resolve this problem, multiple point based ISC is suggested.

The method of multiple point-based ISC for the EGO framework is suggested by Viana et al. [48] and Ginsbourger et al. [49]. It adds multiple infill points at each design iteration and becomes ideal for parallel computation. Details of the computation of the multivariate EI values are referred to Ref. [49], and the assumption of the multivariate Gaussian process for the multiple functions and the resultant mathematical formulations of the multivariate EI value are shown in Eq. (2.22) and (2.23). The definitions of conditional covariance of $\boldsymbol{S}_q$ is also made in the reference papers and omitted here.

$$\begin{aligned} EI\left[(\boldsymbol{x}_{n+1},\cdots,\boldsymbol{x}_{n+n^*})\right] &\equiv E\left[\max\left\{I\left(\boldsymbol{x}_{n+1}\right),\cdots,I\left(\boldsymbol{x}_{n+n^*}\right)\right\} \mid \mathbb{F}\right] \\ &= E\left[\max\left\{\left(\mathbb{F}_{min}-f(\boldsymbol{x}_{n+1})\right),\cdots,\left(\mathbb{F}_{min}-f(\boldsymbol{x}_{n+n^*})\right)\right\} \mid \mathbb{F}\right] \\ &= E\left[\mathbb{F}_{min}-\min\left\{f(\boldsymbol{x}_{n+1}),\cdots,f(\boldsymbol{x}_{n+n^*})\right\} \mid \mathbb{F}\right] \end{aligned} \tag{2.22}$$

$$E\left[\{f(\boldsymbol{x}_{n+1}),\cdots,f(\boldsymbol{x}_{n+n^*})\}\right] \sim G\left(\left[\hat{f}(\boldsymbol{x}_{n+1}),\cdots,\hat{f}(\boldsymbol{x}_{n+n^*})\right]^T,\boldsymbol{S}_q\right) \tag{2.23}$$

where an arbitrary sample point $\boldsymbol{x}$ located in the design space with a dimension of p, and

the exact function value at the location $\boldsymbol{x}$ is $f(\boldsymbol{x})$. Then a set of known exact function values for n number of sample points are defined as $\mathbb{F} = \{f(\boldsymbol{x}_1), f(\boldsymbol{x}_2), \cdots, f(\boldsymbol{x}_n)\}$. I represents the improvement, which can be defined by $I(\boldsymbol{x}) \equiv \mathbb{F}_{min} - f(\boldsymbol{x})$. The n^* is the number of additional sampling at each design iteration.

However, due to prohibitive computational cost related to the Monte Carlo simulation (MCS) [79, 80] to calculate the exact value of multivariate EI, Ginsbourger et al. suggested an alternative ISC method based on an approximated EI value. It finds the n^* number of sample points in a sequential manner using the same procedure of the single point EI, and a function response of a new point is assumed as an arbitrary value rather than the value from computation or simulation. Until a total of n^* points are selected, the hyper-parameters of the Kriging surrogate model are fixed with the values determined by existing n sample points. Authors suggested two approaches depending on the arbitrary value: a Kriging Believer (KB) and a Constant Liar (CL). The KB method uses a Kriging response value temporarily for the exact function value of the new point. The CL method uses an arbitrary constant of L chosen from the existing function responses, which can be a minimum, an average, or a maximum value of the observed responses and denoted as $\mathbb{Y}_{min}$, $\mathbb{Y}_{mean}$, and $\mathbb{Y}_{max}$, respectively. The schematics of algorithms using the KB and CL methods are shown in Table 2.1. Although the approximated q-EI method is more efficient than the exact q-EI method, the choice of arbitrary value leads to a different set of additional sample points so the efficiency of the design process can be enhanced or deteriorated.

In this paper, a method of Multi-Point and Multi-Objective Infill Sampling Criteria(MPMO-ISC) [52] is developed as an alternative method to the multi-point EI. The basic idea is to formulate the trade-off between two competing merits of exploration and exploitation in a form of the multi objective optimization problem. In this multi-objective approach, two metrics to represent the exploration and exploitation quantitatively are the (maximum)

Table 2.1: The algorithms of the approximated q-EI

q-EI algorithm with a Kriging Believer	**q-EI algorithm with a Constant Liar**
Do $i = 1, \cdots, n^*$ $\boldsymbol{x}_{n+i}$**arg max** $EI(\boldsymbol{x})$) $\boldsymbol{x} \in \boldsymbol{D}$ $\mathbb{X} = \mathbb{X} \cup \{\boldsymbol{x}_{n+i}\}$ $\mathbb{Y} = \mathbb{Y} \cup \{\bar{y}(\boldsymbol{x}_{n+i})\}$ END	Do $i = 1, \cdots, n^*$ $\boldsymbol{x}_{n+i}$**arg max** $EI(\boldsymbol{x})$) $\boldsymbol{x} \in \boldsymbol{D}$ $\mathbb{X} = \mathbb{X} \cup \{\boldsymbol{x}_{n+i}\}$ $\mathbb{Y} = \mathbb{Y} \cup \{L\}$ where, $L \in \{\mathbb{Y}_{min}, \mathbb{Y}_{mean}, and \mathbb{Y}_{max}\}$ END

estimation uncertainty $\sigma^2(\hat{f})$ and the (minimum) predicted response value of $\mu(\hat{f})$ from the Kriging surrogate model, respectively. The Pareto front through the multi-objective optimization provides a set of optimal candidate points with quantitative measure of each metric. As the design iteration proceeds, the goal of ISC generally changes such that the exploration is required during initial design iterations to increase the global accuracy of the model, and once a certain level of global accuracy is achieved, the exploitation is necessary for better representation of the local area around the optimum. One important feature is that various combinations are possible for selecting multiple points and criteria for such combination can change dynamically depending on the global versus local characteristics of the surrogate model at the current iteration.

Advantages of the method are several. First, as pointed out in the work of Viana et al. [48] and Ginsbourger et al. [49], the parallel computation can be utilized for function evaluations of the multiple infill sample points, which increase design efficiency by a factor of $n^* \times K$, where n^* is the total number of additional sample points at each iteration and K is the number of total design iterations. Thus, MPMO-ISC selects n^* additional sample points by one execution of the multi-objective optimization and reduces the computing cost. In

addition, unlike the approximated q-EI ISC method which selects the n^* sample points sequentially through a series of the incomplete Kriging models using the arbitrary constant or the Kriging prediction value, the MPMO-ISC approach is solely relying on the Kriging model updated by sample points evaluated by simulations. Although the approximated q-EI method does not re-compute a hyper-parameter of the Kriging model during the infill sampling procedure, the re-construction and inversion of the Kriging correlation matrix is inevitable during the n^* number of optimization to find the maximum EI point.

The main issues of the MPMO-ISC on the adaptive sampling strategy are following: 1) which aspect should be more focused out of the exploration and exploitation, and 2) how to control the ratio of two metrics. The following subsections describe two different approaches of the MPMO-ISC method to directly address the issues: a balancing approach and a dynamic switching approach.

With three additional infill sample points per design iteration, the balancing approach adds two points from the two far ends of the Pareto front (one for the exploration and the other for the exploitation) and one additional point in between the two end points. The dynamic switching approach selects all three points near from the one of far end.

Balancing approach

At a given design iteration and the Kriging surrogate model, a sub-procedure of the multi-objective optimization is carried out to produce the Pareto front of the optimum candidates. Figure 2.2 shows an example of the multi-objective Pareto front where two axes represent the objectives of finding the large estimation uncertainty (σ_f^2) to improve the global accuracy (exploration) and of minimizing the predicted value of the response ($\bar{f}$) for the local accuracy (exploitation), respectively. The point $P_{\sigma^2_{max}}$ corresponds to the maximum value of estima-

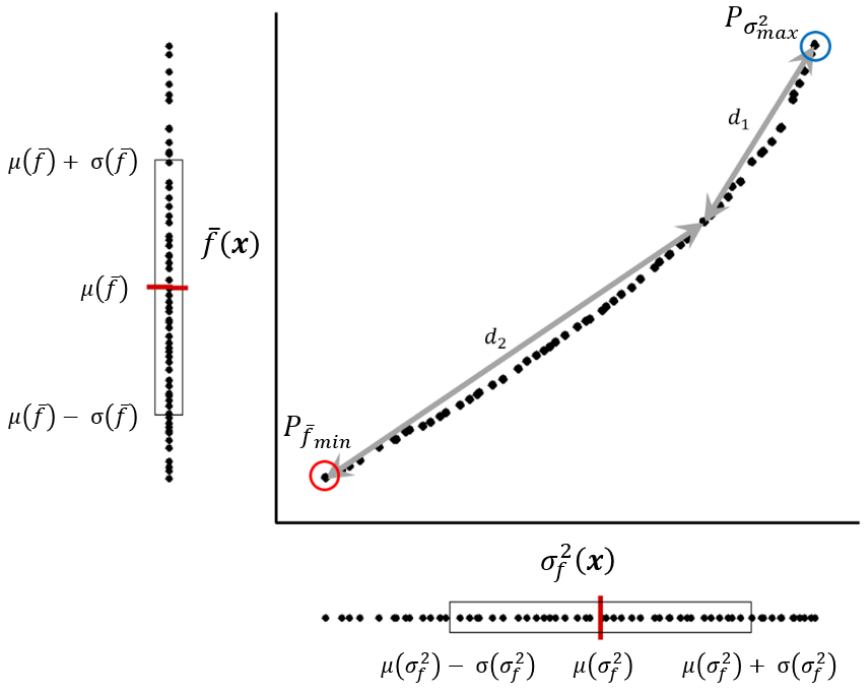

Figure 2.2: Pareto-front for ISC

tion uncertainty on the Pareto-front, and the point $P_{\bar{f}_{min}}$ corresponds to the minimum value of predicted responses. Therefore, points near the $P_{\sigma^2_{max}}$ tend to have large σ_f^2 values, while those around the $P_{\bar{f}_{min}}$ tend to have a lower function response than the current minimum. The balancing approach chooses both $P_{\bar{f}_{min}}$ and $P_{\sigma^2_{max}}$ at each design iteration regardless of the particular distribution of points on the Pareto front and tries to balance the metrics of the exploration and exploitation. The approach also selects one additional point somewhere on the Pareto-front between $P_{\bar{f}_{min}}$ and $P_{\sigma^2_{max}}$, so that the point improves the accuracy of the current Kriging surrogate model, whether local or global.

However, the exact quantification of the global and local accuracy requires the cross-validation with a large number of sample points, which is not practical and computationally prohibitive. An alternative way to determine which objective needs to be focused is the statistical distribution of the optimal candidate points on each objective. Low variance with low mean

value of an objectives indicates the convergence of desired accuracy, and therefore variance is used to diagnose whether the current Kriging model requires exploration or exploitation. For example, the large variance in the estimation uncertainty indicates poor global accuracy and more sample points are needed for the exploration. Likewise, the small variance value in the minimum predicted response values implies that additional samples point need to be added for further refinement around the minimum. The ratio of the two variance values is meaningful. For fair comparison between two variance values, the coefficient of variation (COV) [81], $[\hat{c}_v]$, is introduced, and those for the estimation uncertainty σ_f^2 and predicted response value $\bar{f}$ are calculated using Eq. (2.24).

$$\begin{aligned}
[\hat{c}_v]_{\sigma_f^2} &= \frac{\sigma\left(\sigma_f^2\right)}{\mu\left(\sigma_f^2\right)}\ ,\ \mu\left(\sigma_f^2\right) = \frac{1}{n_{pop}}\sum_{i=1}^{n_{pop}}\left(\sigma_f^2\right)_i\ ,\ \sigma\left(\sigma_f^2\right) = \frac{1}{n_{pop}-1}\sum_{i=1}^{n_{pop}}\left[\left(\sigma_f^2\right)_i - \mu\left(\sigma_f^2\right)\right]^2 \\
[\hat{c}_v]_{\bar{f}} &= \frac{\sigma\left(\bar{f}\right)}{\mu\left(\bar{f}\right)}\ ,\ \mu\left(\bar{f}\right) = \frac{1}{n_{pop}}\sum_{i=1}^{n_{pop}}\left(\bar{f}\right)_i\ ,\ \sigma\left(\bar{f}\right) = \frac{1}{n_{pop}-1}\sum_{i=1}^{n_{pop}}\left[\left(\bar{f}\right)_i - \mu\left(\bar{f}\right)\right]^2
\end{aligned} \tag{2.24}$$

where n_{pop} is the total number of optimal candidates on the Pareto-front.

The third point P_3 is selected based on the ratio of the two COVs of $[\hat{c}_v]_{\sigma_f^2}$ and $[\hat{c}_v]_{\bar{f}}$. To relate the COV ratio to a sample point on the Pareto-front, the Euclidean distances from the two extreme points of $P_{\bar{f}_{min}}$ and $P_{\sigma^2_{max}}$ to an arbitrary point P, d_1 and d_2, can be computed as shown in Eq. (2.25).

$$\begin{aligned}
d_1(P) &= \sqrt{\left[\sigma_f^2(P) - \sigma_f^2\left(P_{\sigma^2_{max}}\right)\right]^2 + \left[\bar{f}(P) - \bar{f}\left(P_{\sigma^2_{max}}\right)\right]^2} \\
d_2(P) &= \sqrt{\left[\sigma_f^2(P) - \sigma_f^2\left(P_{\bar{f}_{min}}\right)\right]^2 + \left[\bar{f}(P) - \bar{f}\left(P_{\bar{f}_{min}}\right)\right]^2}
\end{aligned} \tag{2.25}$$

The third point P3 is chosen such that the ratio of d_1/d_2 is equivalent or closest to that of

the two COVs, and this relationship is shown in Eq. (2.26). Note that the indices for two ratios are reversed.

$$d_1 : d_2 = [\hat{c}_v]_{\bar{f}} : [\hat{c}_v]_{\sigma_f^2} \tag{2.26}$$

In this way, a point close to $P_{\sigma^2_{max}}$ is selected to improve the global accuracy when the variance value of σ_f^2 is relatively large ($d_1 > d_2$). The three additional sample points, including two extreme points and the one in between, are selected at each design iteration to improve the accuracy of the Kriging model, and this procedure is iterated until termination criteria are met.

Dynamic switching approach

The dynamic switching approach is developed to resolve an issue of how to decide which aspect should be more focused out of two criteria of the exploration and exploitation. From the Pareto front shown in Figure 2.2, to focus on exploration or exploitation selectively, the sample points can be selected near one end of the front, rather than at both ends. The dynamic switching approach keeps track of the global accuracy of the fit throughout the entire design iterations via the average value of estimation uncertainty in the Pareto front, $\mu^{(k)}\left(\sigma_f^2\right)$, where (k) represents an iteration step. The ISC are switched the rule of infilling between exploitation and exploration by the comparison of $\mu\left(\sigma_f^2\right)$ at the current design iteration and the threshold value, T. The threshold value is calculated as the multiplication of the switching parameter, κ, and the maximum value of $\mu^{(k)}\left(\sigma_f^2\right)$ from the beginning of the design iteration to the current design iteration, and shown as

$$T = \kappa \times \text{Max}\left[\mu^{(k)}\left(\sigma_f^2\right)\right] \ , \ k = 1, 2, \cdots \tag{2.27}$$

If $\mu\left(\sigma_{\hat{f}}^2\right)$ of the current design iteration is larger than T, then points around the $P_{\sigma_{max}^2}$ are selected for the exploration, otherwise; points around the $P_{\bar{f}_{min}}$ are selected for the exploitation. Additional samples should not be clustered to avoid ill condition and to guarantee the exploration.

To avoid the clustering of additional samples, clustering parameters, θ_G and θ_L, are defined as well as the size of the design space, $D^{(k)}$, which is the distance between the two most distant points in the set of all sample points and defined as below.

$$D^{(k)} = \text{Max}\left[|\boldsymbol{x}_i - \boldsymbol{x}_j|\right] \ , \ i, j = 1, 2, \cdots, n^{(k)} \tag{2.28}$$

where $n^{(k)}$ represents the number of samples in the current design iteration. If the additional samples should be selected around $P_{\sigma_{max}^2}$ ($\mu\left(\sigma_{\hat{f}}^2\right) >$ T), the distance between additional samples are restricted to be larger than $\theta_G \times D^{(k)}$. To improve the global accuracy efficiently, θ_G is set to be a large number. If the additional samples should be selected around $P_{\bar{f}_{min}}$ ($\mu\left(\sigma_{\hat{f}}^2\right) <$ T), the distance between additional sample points should be larger than $\theta_L \times D^{(k)}$ to prevent numerical instability of Kriging surrogate model. Three parameters of κ, θ_G and θ_L vary from 0 to 1, and have to be specified prior to the design. Sensitivity and parameter study is introduced in the chapter of validation.

2.3.3 Infilling samples for variable fidelity optimization

The developed infill sampling method of Multi-Response Multi-Objective Infill Sampling Criteria (MPMO-ISC) can be implemented for the variable fidelity optimization process. For a single-fidelity EGO process, the metric which is shown in the previous pages can be applied; the maximum estimation uncertainty $\sigma^2\left(\hat{f}_{VF}\right)$ for the exploration and the mini-

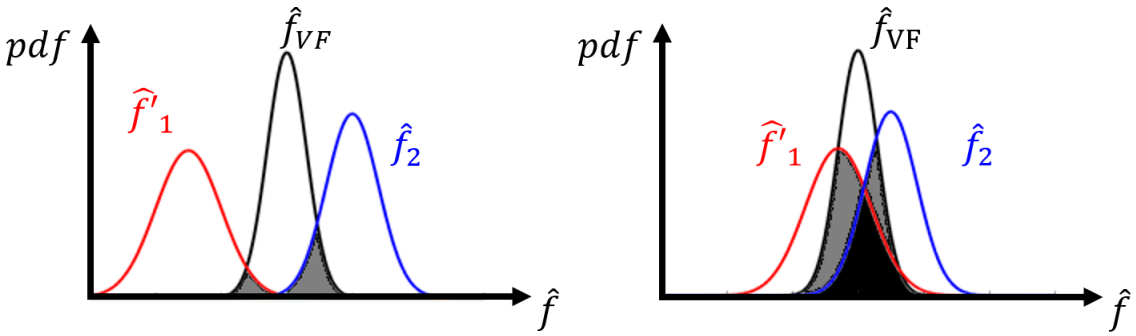

(a) Poorly agreed case (b) Well agreed case

Figure 2.3: Comparison of probability density function of calibrated lower fidelity Kriging, the highest fidelity Kriging, and variable fidelity Kriging at an arbitrary design point

mum predicted response value $\mu\left(\hat{f}_{VF}\right)$ for the exploitation. However, in variable-fidelity optimization, since the lower-fidelity sample data sets are updated based on the reference data of the highest fidelity sample set, new metric of MPMO-ISC is needed for the exploration. In this paper, a new metric of exploration which uses the agreement between updated lower-fidelity sample data, the highest fidelity sample data, and variable-fidelity Kriging is suggested.

First of all, the single-fidelity Kriging model is constructed with calibrated and filtered sample set for each fidelity at the current design iteration as below,

$$\hat{f'}_m^{(k)}(\hat{\boldsymbol{x}}) = KRG\left(\left\{f'_m(\boldsymbol{x_i}) \mid i \in \left(\mathcal{I}_m^{(k)} - \mathcal{I}_m^{-(k)}\right)\right\}\right) \ , m = 1, 2, \cdots, r-1 \tag{2.29}$$

Now, we will check the agreement (or similarity) between $\hat{f'}_m^{(k)}$, $\hat{f}_r^{(k)}$, and $\hat{f}_{VF}^{(k)}$. Figure 2.3 shows an example of probability density function at an arbitrary location in the design space for a variable-fidelity Kriging with one low fidelity sample set and one high fidelity sample set. If we do not have much information at a certain location, and the sample

update is not well-performed, Kriging prediction from $\hat{f}'_1$, $\hat{f}_2$, and $\hat{f}_{VF}$ do not well-matched (agreed) with each other as shown in sub-figure 2.3a. Grey and black region in the sub-figure are the overlapped region between the probability distribution, and we can determine that the region is very small. However, if we have enough information for the variable-fidelity analysis at an arbitrary location $\hat{\boldsymbol{x}}$, the overlapped region will be much larger as shown in sub-figure 2.3b. Therefore, we will need more information, additional samples, in the location of poor agreement to improve the sample calibration performance.

To evaluate the agreement between probability distribution, overlapping coefficient(OVL) [76] is used. The definition of OVL is provided in Eq. (2.18). The OVL between Kriging by each calibrated single fidelity sample set and variable fidelity Kriging, $OVL^{(k)}_{m,VF}(\hat{\boldsymbol{x}})$ for $m = 1, 2, \cdots, r$, can be defined as below,

$$\begin{aligned} OVL^{(k)}_{m,VF}(\hat{\boldsymbol{x}}) &= OVL\left(\hat{f}'^{(k)}_m(\hat{\boldsymbol{x}}), \hat{f}^{(k)}_{VF}(\hat{\boldsymbol{x}})\right), \text{ for } m = 1, 2, \cdots, r-1 \\ OVL^{(k)}_{r,VF}(\hat{\boldsymbol{x}}) &= OVL\left(\hat{f}^{(k)}_r(\hat{\boldsymbol{x}}), \hat{f}^{(k)}_{VF}(\hat{\boldsymbol{x}})\right) \end{aligned} \tag{2.30}$$

Now, we can define a new metric of exploration in variable fidelity Kriging, which is ΣOVL as shown below,

$$\Sigma OVL^{(k)}(\hat{\boldsymbol{x}}) = \sum_{m=1}^{r} OVL^{(k)}_{m,VF}(\hat{\boldsymbol{x}}) \tag{2.31}$$

In Figure 2.3, the area of grey and black region of overlapped pdf is equivalent to $\Sigma OVL^{(k)}(\hat{\boldsymbol{x}})$. As the summation of all $OVL^{(k)}_{m,VF}$ values at $\hat{\boldsymbol{x}}$ estimate overall similarity of the function prediction by an individual fidelity to the variable-fidelity Kriging, the low value indicates high probability of that some of the analysis fidelities are not compatible with the variable-fidelity

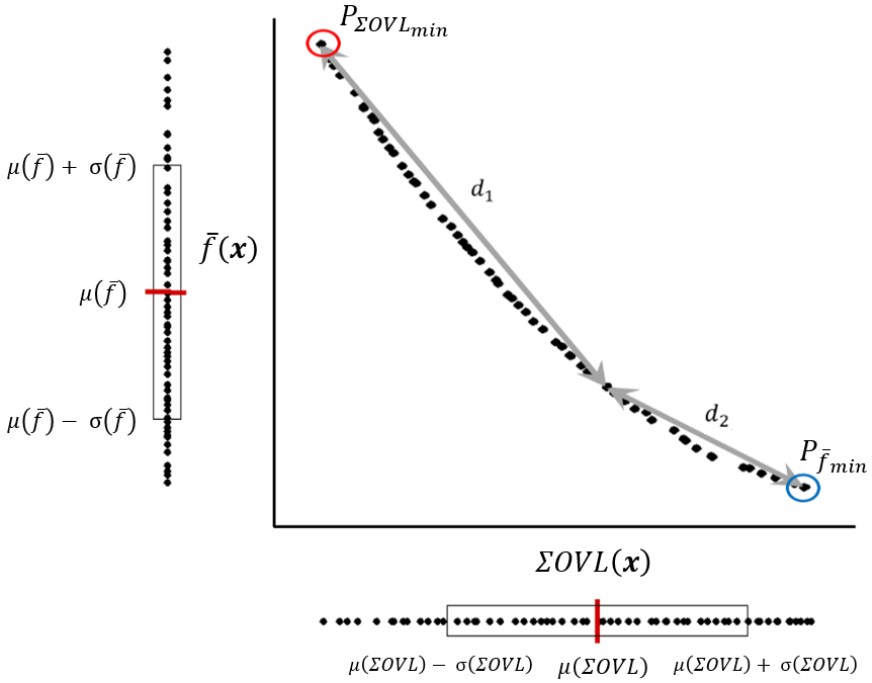

Figure 2.4: Pareto-front for ISC in variable-fidelity Kriging

analysis, inferring high estimation uncertainty in relation to the global accuracy. Therefore, $\Sigma OVL^{(k)}(\hat{\boldsymbol{x}})$ can replace the first objective function of $\sigma^2(\hat{f})$ in MPMO-ISC of previous section for the global accuracy, exploration. On the other hand, we can still use the Kriging-predicted function minimum, which is associated with the local accuracy in comparison to the exact minimum, as the second objective function.

For these two objective functions, multi-objective optimization using a genetic algorithm is performed to find the optimum candidates with both minimum $\Sigma OVL^{(k)}$ and minimum $\bar{f}$. As the result of multi-objective optimization, the Pareto front of the optimum candidates can be obtained, and a balancing approach or a dynamic switching approach can be used to select the additional sample points. Figure 2.4 shows an example Pareto front for the use of a balancing approach.

2.4 Dynamic Fidelity Indicator

In the previous section, additional sample points are selected in the variable-fidelity Kriging model through multi-point multi-objective infill sampling criteria. Unlike Efficient Global Optimization (EGO) with single fidelity analysis, in EGO with variable fidelity analysis, the fidelity of additional samples should be decided. For the fidelity decision making, the probabilistic fidelity indication is carried out for the function analysis of infill sample points.

First of all, for each of infill sample points, $OVL^{(k)}_{m,VF}(\tilde{\boldsymbol{x}}_i)$ for $i = 1, 2, \cdots n^*$ is evaluated, where $m = 1, 2, \cdots, r$.

$$\begin{aligned} OVL^{(k)}_{m,VF}(\tilde{\boldsymbol{x}}_i) &= OVL\left(\hat{f}'^{(k)}_m(\tilde{\boldsymbol{x}}_i), \hat{f}^{(k)}_{VF}(\tilde{\boldsymbol{x}}_i)\right), \text{ for } m = 1, \cdots, r-1, i = 1, \cdots n^* \\ OVL^{(k)}_{r,VF}(\tilde{\boldsymbol{x}}_i) &= OVL\left(\hat{f}^{(k)}_r(\tilde{\boldsymbol{x}}_i), \hat{f}^{(k)}_{VF}(\tilde{\boldsymbol{x}}_i)\right), \ i = 1, \cdots n^* \end{aligned} \tag{2.32}$$

where $\tilde{\boldsymbol{x}}$ represents the sample location of infill adaptive sampling. n^* is the number of additional samples and equal to 3 in the balancing approach of MPMO-ISC. Since higher OVL indicates that the prediction of single fidelity Kriging is well matching with the prediction of variable fidelity Kriging model, the fidelity which has the highest OVL value is chosen for the function analysis. Thus, the dynamic fidelity indicator, DFI, returns the analysis fidelity index given the infill sample point under consideration and is mathematically defined as

$$\begin{aligned} DFI^{(k)}(\tilde{\boldsymbol{x}}_i) = \Big\{ m \mid \max\left[OVL^{(k)}_{m,VF}(\tilde{\boldsymbol{x}}_i)\right] = OVL^{(k)}_{m,VF}(\tilde{\boldsymbol{x}}_i), \ m = 1, 2, \cdots, r \Big\}, \\ \text{for } i = 1, 2, \cdots, n^* \end{aligned} \tag{2.33}$$

Now, the indices of data set for next design iteration can be expressed as shown below,

$$\begin{aligned}\mathcal{I}^{(k+1)} &= \mathcal{I}_{VF}^{(k)} \cup \mathcal{I}^{-(k)} \cup \mathcal{I}^{+(k)} \\ &= \mathcal{I}^{(k)} \cup \mathcal{I}^{+(k)}\end{aligned} \tag{2.34}$$

where $\mathcal{I}^{+(k)}$ represents the indices of data set for the adaptive infill sampling from MPMO-ISC and DFI criteria. It should be noted that the lower-fidelity sample which is filtered out at the current (k)th design iteration, $f_m^{(k)}(\boldsymbol{x}_i),\ i \in \mathcal{I}_m^{-(k)}$, are included again in the next $(k+1)$th design iteration since the highest fidelity Kriging model, which is the reference of error calibration, keeps being improved in accuracy by infilling additional sample points.

2.5 Variable Fidelity EGO Framework

In the previous sections, new design method of variable fidelity analysis, dynamic sampling, and dynamic fidelity indicator is introduced. Integrating these design methods into Efficient Global Optimization(EGO), variable fidelity EGO framework can be constructed as shown in Figure 2.5.

First, the location of the sets of initial samples in different fidelity analysis is selected. As done in the general EGO framework, to distribute the design samples evenly in the multi-dimension design space, random sampling, Orthogonal sampling, or Latin Hypercube Sampling (LHS) can be used. To reduce the overall design cost, large number of lower fidelity samples and small number of high fidelity samples are selected.

Then, the sample evaluation for the selected training sample is performed with simulations in different fidelities. Once we obtain the function values, single-fidelity Kriging model is constructed for each different fidelity sample set, and error is estimated. Using estimated

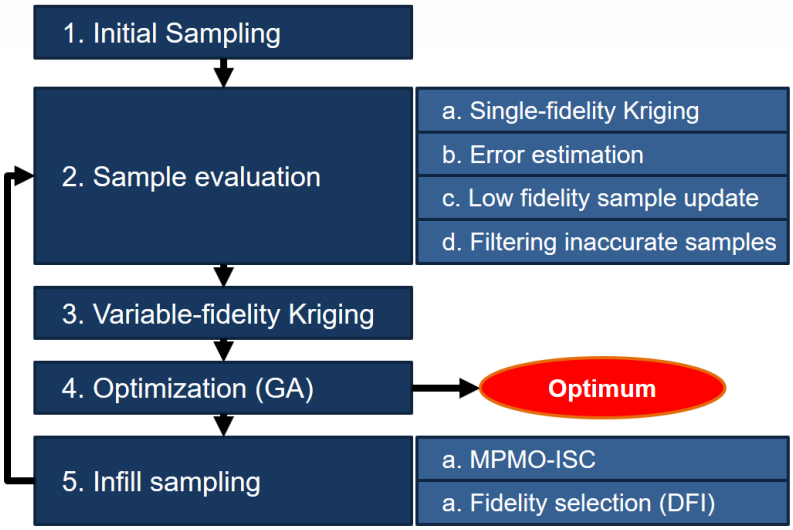

Figure 2.5: The schematics of variable fidelity EGO framework

error terms, lower fidelity samples are calibrated, and inaccurately calibrated lower fidelity samples are filtered out. (Step 2)

Using calibrated and filtered lower fidelity sample and the highest fidelity samples, variable-fidelity Kriging model can be constructed. (Step 3) Once the variable fidelity Kriging model is constructed, a genetic algorithm (GA) is applied to identify candidates of design optimum. (Step 4) The accuracy of the model is validated by the highest fidelity analysis for the predicted optimum. If the error between predicted optimum from Kriging model and the function value from the highest fidelity analysis at the optimum sample location is smaller than the criteria, the process is terminated. (Red box) Otherwise, the design process proceed to the next step, which is infill sampling.

In infill sampling step (Step 5), the location of additional samples is determined using Multi-Point Multi-Objective Infill Sampling Criteria for variable-fidelity optimization. Then, the fidelity of additional sample is selected through the dynamic fidelity indicator. There information is integrated with the initial samples, and the process goes to the second step to evaluate the function value of the additional samples.

Chapter 3

Extension to Multidisciplinary Optimization

In this chapter, the variable-fidelity optimization framework in the previous section will be extended for multidisciplinary optimization problems. To handle multiple disciplines in Efficient Global Optimization, multi-response Kriging surrogate model is studied, and iterative method to estimate Maximum Likelihood is developed for better global accuracy performance. The details of multi-response Kriging and implementation of one in variable fidelity optimization will be provided in the following sections.

3.1 Multi-response Kriging (MRK)

In the practical design, we used to face multidisciplinary problems, such as aeroelasticity problems, aerothermal problems and aeroservoelasticity problems. In these problems, we can still construct single-response GPR model for each discipline, which is introduced in the beginning of previous chapter. However, using single-response GPR model, the information of physical correlation between disciplines will be ignored even though two or more disciplines are tightly coupled to each other. To consider the coupling between different disciplines mathematically in GPR model, multi-response Kriging (MRK) is introduced in this section.

In this paper, two types of MRK model are introduced, which are a reduced-covariance

multiple response Kriging (RC-MRK) and a fully expended covariance multiple response Kriging (FEC-MRK). The discrepancy of the two MRK models lies in the structure of the covariance matrix. RC-MRK assumes that the covariance function for multi-response is the nominal uni-output covariance multiplied by the covariances between different outputs. Since the covariance function for multi-response is the nominal uni-output form, the covariance matrix of responses can be separated from the spatial covariance matrix. Whereas FEC-MRK has non-separable dependent covariance structure, which means that the covariance matrix of responses and the spatial covariance matrix are tightly coupled and not separable. The detail of two MRK models is described below.

3.1.1 Reduced-Covariance Multi-Response Kriging (RC-MRK)

For the q-dimensional responses, $\boldsymbol{y} = [y_1, y_2, \cdots, y_q]^T$, the multi-response linear regression model can be expressed as below,

$$\boldsymbol{y}_i = \boldsymbol{K}_i \boldsymbol{W} + \boldsymbol{\epsilon}_i, \ i = 1, 2, \cdots, n \tag{3.1}$$

where n is the number of observed data points and $\boldsymbol{K}_i \left(= \boldsymbol{I}_q \otimes \boldsymbol{x}_i^T\right)$ is the Kronecker product of the $(q \times q)$ identity matrix and p-dimensional input covariates vector. Therefore, the size of $\boldsymbol{K}_i$ is $(q \times pq)$. $\boldsymbol{W}$ is the concatenation of the regression vectors for the q response variables, which can be expressed as $\boldsymbol{W} = \left[\boldsymbol{w_1^T}, \boldsymbol{w_2^T}, \cdots, \boldsymbol{w_q^T}\right]^T$. The size of $\boldsymbol{W}$ is $(pq \times 1)$. $\boldsymbol{\epsilon}_i$ is a q-dimensional vector of noise given by a zero mean Gaussian distribution as below,

$$\boldsymbol{\epsilon}_i \sim G(\boldsymbol{0}, \boldsymbol{S}) \tag{3.2}$$

where $\boldsymbol{S}$ is $(q \times q)$ covariance matrix between the elements of $\boldsymbol{\epsilon}_i$ vector. Since the noise

is generally assumed to be independently and identically distributed noise, $\boldsymbol{S}$ becomes a diagonal matrix.

If the prior probability for the vectors of regression parameter $\boldsymbol{w}_g$ and $\boldsymbol{w}_h$, where g and h varies from 1 to q, is assumed to follow a Gaussian process, the covariance matrix between regression vectors can be defined as below,

$$\operatorname{cov}(\boldsymbol{w}_g, \boldsymbol{w}_h) = b_{gh}\sigma^2 \boldsymbol{I}_p \tag{3.3}$$

where b_{gh} forms a $(q \times q)$ symmetric matrix $\boldsymbol{B}$, which corresponds the covariance between outputs.

Now, for trial locations $\hat{\boldsymbol{x}} \in \mathbb{R}^p$ which has vectors of estimated function value $\hat{\boldsymbol{y}}$, the joint probability distribution of observed data augmented by $\hat{\boldsymbol{x}}$ and $\hat{\boldsymbol{y}}$ can be considered to evaluate the Gaussian process posterior distribution at $\hat{\boldsymbol{x}}$.

$$\begin{bmatrix} \boldsymbol{y}_{aug,RC-MRK} \\ \hat{\boldsymbol{y}} \end{bmatrix} \sim G\left(\boldsymbol{0}, \begin{bmatrix} \boldsymbol{C}(\boldsymbol{x_i}, \boldsymbol{x_j}) & \boldsymbol{C}(\boldsymbol{x_i}, \hat{\boldsymbol{x}}) \\ \boldsymbol{C}(\hat{\boldsymbol{x}}, \boldsymbol{x_j}) & \boldsymbol{C}(\hat{\boldsymbol{x}}, \hat{\boldsymbol{x}}) \end{bmatrix} \right), \; i, j = 1, 2, \cdots, n \tag{3.4}$$

where $\boldsymbol{y}_{aug,RC-MRK} = [\boldsymbol{y}_1^T, \boldsymbol{y}_2^T, \cdots, \boldsymbol{y}_q^T]^T = [y_{11}, \cdots, y_{1n}, y_{21}, \cdots, y_{2n}, \cdots, y_{q1}, \cdots, y_{qn}]^T$ is an augmented vector of observed response variables, and $\boldsymbol{C}$ is a covariance matrix between sample points. In Ref [27], the covariance function is suggested as below,

$$\begin{aligned} C_{ij}^{gh} &= Q_{ij} b_{gh} + \delta_{ij}\delta_{gh} S_{gh} \\ Q_{ij} &= a_0 + a_1 \sum_{d=1}^{p} x_{id} x_{jd} + \nu_0 \exp\left(- \sum_{d=1}^{p} \eta_d \left(x_{id} - x_{jd} \right)^2 \right) \end{aligned} \tag{3.5}$$

where a_0, a_1, ν_0, and η_d are hyper-parameters. Each hyper-parameter correspond bias term, the weight of linear correlation function, the weight of Gaussian correlation function, and the weight on distance in Gaussian correlation function, respectively. From Eq. (3.5), the covariance matrix of $\boldsymbol{C}$ can be derived as below.

$$\begin{aligned}\boldsymbol{C} &= \begin{bmatrix} b_{11}\boldsymbol{Q} + S_{11}\boldsymbol{I}_n & b_{12}\boldsymbol{Q} & \cdots & b_{1q}\boldsymbol{Q} \\ b_{21}\boldsymbol{Q} & b_{22}\boldsymbol{Q} + S_{22}\boldsymbol{I}_n & \cdots & b_{2q}\boldsymbol{Q} \\ \vdots & \vdots & \ddots & \vdots \\ b_{q1}\boldsymbol{Q} & b_{q2}\boldsymbol{Q} & \cdots & b_{qq}\boldsymbol{Q} + S_{qq}\boldsymbol{I}_n \end{bmatrix} \\ &= \boldsymbol{B} \otimes \boldsymbol{Q} + \boldsymbol{S} \otimes \boldsymbol{I}_n \end{aligned} \tag{3.6}$$

where $\otimes$ denotes the Kronecker product. Since $\boldsymbol{C}$ is a function of samples with multiple response covariates, the size is $(qn \times qn)$. $\boldsymbol{S}$ matrix is q-dimensional diagonal matrix of noise which is related to ϵ_i, above. Since these terms are unknown as well, we have S_{11}, S_{22}, $\cdots$, S_{qq} unknown variables, which are the elements of $\boldsymbol{S}$ matrix and another hyper-parameters. In the covariance matrix, $\boldsymbol{B}$ is the matrix of covariance between responses, which is a symmetric matrix. Therefore, the matrix can be re-organized as shown below.

$$\boldsymbol{B} = \boldsymbol{\phi}\boldsymbol{\phi}^T, \boldsymbol{\phi} = \begin{bmatrix} \phi_{11} & 0 & \cdots & 0 \\ \phi_{21} & \phi_{22} & \cdots & 0 \\ \vdots & \vdots & \ddots & \vdots \\ \phi_{q1} & \phi_{q1} & \cdots & \phi_{q1} \end{bmatrix} \tag{3.7}$$

where ϕ_{11}, ϕ_{21}, ϕ_{22}, $\cdots$ ϕ_{qq} are the hyper-parameters for the covariance between responses. Therefore, in multiple-response GPR model, we have $\left(p + \frac{q(q+3)}{2} + 3\right)$ number of unknown

hyper-parameters, which should be determined. These hyper-parameters can be determined by Maximum Likelihood Estimation (MLE) process. The equation below shows the equation of likelihood. Searching for the hyper-parameters which maximize the likelihood below, we can construct multi-response Kriging, which minimize the Mean Square Error(MSE) of Kriging estimation at the sample location.

$$L = -\frac{1}{2}\log[\det \boldsymbol{C}] - \frac{1}{2}\boldsymbol{y}_{aug,RC-MRK}^{T}\boldsymbol{C}^{-1}\boldsymbol{y}_{aug,RC-MRK} - \frac{nq}{2}\log[2\pi] \tag{3.8}$$

From the Eq. (3.4) and (3.6), using Gaussian identities, the posterior probability, which is the conditional probability of $\hat{\boldsymbol{y}}$ for given data $\boldsymbol{y}$ can be calculated as below,

$$\begin{aligned} p\left(\hat{\boldsymbol{y}}|\boldsymbol{y}_{aug,RC-MRK}\right) &= G\left(\boldsymbol{\mu}(\hat{\boldsymbol{y}}), \boldsymbol{\sigma}^2(\hat{\boldsymbol{y}})\right) \\ \boldsymbol{\mu}(\hat{\boldsymbol{y}}) &= \left[\boldsymbol{B} \otimes \hat{\boldsymbol{Q}}\right]^T \boldsymbol{C}^{-1}\boldsymbol{y}_{aug,RC-MRK} \\ \boldsymbol{\sigma}^2(\hat{\boldsymbol{y}}) &= \boldsymbol{B} \otimes Q\left(\hat{\boldsymbol{x}}, \hat{\boldsymbol{x}}\right) + \boldsymbol{S} - \left[\boldsymbol{B} \otimes \hat{\boldsymbol{Q}}\right]^T \boldsymbol{C}^{-1}\left[\boldsymbol{B} \otimes \hat{\boldsymbol{Q}}\right] \end{aligned} \tag{3.9}$$

where $\mu(\hat{\boldsymbol{y}})$ is the mean of $\hat{\boldsymbol{y}}$, which is a vector of estimated multi-response function values at a trial location $\hat{\boldsymbol{x}}$, and $\sigma^2(\hat{\boldsymbol{y}})$ is a matrix of estimation uncertainty for each response. The estimation uncertainty matrix includes the variance of the prediction at the trial location and the covariance of the prediction between different responses as shown in Eq. (3.10). $\hat{\boldsymbol{Q}} = [Q(\boldsymbol{x}_1, \hat{\boldsymbol{x}}), Q(\boldsymbol{x}_2, \hat{\boldsymbol{x}}), \cdots, Q(\boldsymbol{x}_n, \hat{\boldsymbol{x}})]$ is the covariances between the test data point $\hat{\boldsymbol{x}}$ and the training sample sets. The detailed derivation is introduced in Ref [27].

$$\boldsymbol{\sigma}^2(\hat{\boldsymbol{y}}) = \begin{bmatrix} Var(\hat{y}_1) & Cov(\hat{y}_1, \hat{y}_2) & \cdots & Cov(\hat{y}_1, \hat{y}_q) \\ Cov(\hat{y}_2, \hat{y}_1) & Var(\hat{y}_2) & \cdots & Cov(\hat{y}_2, \hat{y}_q) \\ \vdots & \vdots & \ddots & \vdots \\ Cov(\hat{y}_q, \hat{y}_1) & Cov(\hat{y}_q, \hat{y}_2) & \cdots & Var(\hat{y}_q) \end{bmatrix} \tag{3.10}$$

3.1.2 Fully-Expanded-Covariance Multi-Response Kriging (FEC-MRK)

For n number of observed training samples, fully expanded covariance multi-response Kriging (FEC-MRK) defines the covariance matrix C as shown in Eq. (3.11). While RC-MRK uses Kronecker product to separate the covariance between responses and the spatial covariance, FEC-MRK includes the effect of both covariance into one matrix, $\boldsymbol{Cov}\left(\boldsymbol{y}(\boldsymbol{x}_i), \boldsymbol{y}(\boldsymbol{x}_j)\right) (i, j = 1, 2, \cdots, n)$.

$$\boldsymbol{C} = \begin{bmatrix} \boldsymbol{B} & \boldsymbol{Cov}\left(\boldsymbol{y}(\boldsymbol{x}_1), \boldsymbol{y}(\boldsymbol{x}_2)\right) & \cdots & \boldsymbol{Cov}\left(\boldsymbol{y}(\boldsymbol{x}_1), \boldsymbol{y}(\boldsymbol{x}_n)\right) \\ \boldsymbol{Cov}\left(\boldsymbol{y}(\boldsymbol{x}_2), \boldsymbol{y}(\boldsymbol{x}_1)\right) & \boldsymbol{B} & \cdots & \boldsymbol{Cov}\left(\boldsymbol{y}(\boldsymbol{x}_2), \boldsymbol{y}(\boldsymbol{x}_n)\right) \\ \vdots & \vdots & \ddots & \vdots \\ \boldsymbol{Cov}\left(\boldsymbol{y}(\boldsymbol{x}_n), \boldsymbol{y}(\boldsymbol{x}_1)\right) & \boldsymbol{Cov}\left(\boldsymbol{y}(\boldsymbol{x}_n), \boldsymbol{y}(\boldsymbol{x}_2)\right) & \cdots & \boldsymbol{B} \end{bmatrix} \tag{3.11}$$

where $\boldsymbol{Cov}\left(\boldsymbol{y}(\boldsymbol{x}_i), \boldsymbol{y}(\boldsymbol{x}_j)\right)$ is the covariance matrix between the samples at $\boldsymbol{x}_i$ and $\boldsymbol{x}_j$. Including the covariance between responses and spatial covariance terms, the matrix can be expressed as below,

$$\boldsymbol{Cov}\left(\boldsymbol{y}(\boldsymbol{x}_i), \boldsymbol{y}(\boldsymbol{x}_j)\right) = \boldsymbol{ARA}^T$$

$$\boldsymbol{R} = \begin{bmatrix} R(d_{i,j};\theta^{(1)}) & 0 & \cdots & 0 \\ 0 & R(d_{i,j};\theta^{(2)}) & \cdots & 0 \\ \vdots & \vdots & \ddots & \vdots \\ 0 & 0 & \cdots & R(d_{i,j};\theta^{(q)}) \end{bmatrix} \tag{3.12}$$

where $R(d_{i,j};\theta^{(g)})$ is Gaussian correlation function $\exp\left[-\theta^{(g)}\left(\boldsymbol{x}_i - \boldsymbol{x}_j\right)^2\right]$ in Ref. [28]. $\boldsymbol{A}$ is the eigen-decomposition of $\boldsymbol{B}$ while guaranteeing that $\boldsymbol{A}$ is positive-definite matrix $\left(\boldsymbol{B} = \boldsymbol{AA}^T\right)$ [82], and $\boldsymbol{B}$ is the covariance matrix between responses and it does not vary with the input combination $\boldsymbol{x_i}$.

$$\boldsymbol{B} = \begin{bmatrix} \sigma_1^2 & \sigma_{1,2} & \cdots & \sigma_{1,q}^2 \\ \sigma_{2,1} & \sigma_2^2 & \cdots & \sigma_{2,q} \\ \vdots & \vdots & \ddots & \vdots \\ \sigma_{q,1} & \sigma_{q,2} & \cdots & \sigma_q^2 \end{bmatrix} = \begin{bmatrix} b_{11} & b_{12} & \cdots & b_{1q} \\ b_{21} & b_{22} & \cdots & b_{2q} \\ \vdots & \vdots & \ddots & \vdots \\ b_{q1} & b_{q2} & \cdots & b_{qq} \end{bmatrix} \tag{3.13}$$

where $\sigma_{g,h}$ is the covariance between the response, $Cov(\boldsymbol{y_g}, \boldsymbol{y_h})$. In Eq. (3.11), for $i = j$, which is diagonal blocks of covariance matrix $\boldsymbol{C}$, the diagonal elements in $\boldsymbol{R}$ matrix are equal to 1, and $\boldsymbol{R}$ matrix becomes an identity matrix. Therefore, only the covariance between responses are considered and the diagonal block becomes $\boldsymbol{B}$ matrix.

In the paper, for the comparison with RC-MRK method, the correlation function in Eq. (3.5) is used for REC-MRK. Using the correlation function in Eq. (3.5), $\boldsymbol{R}$ can be written as below.

$$\boldsymbol{R} = \begin{bmatrix} Q_{ij}^{(1)} & 0 & \cdots & 0 \\ 0 & Q_{ij}^{(2)} & \cdots & 0 \\ \vdots & \vdots & \ddots & \vdots \\ 0 & 0 & \cdots & Q_{ij}^{(q)} \end{bmatrix}$$
$$Q_{ij}^{(g)} = a_0^{(g)} + \nu_0^{(g)} \exp\left(- \sum_{d=1}^{p} \eta_d \left(x_{id} - x_{jd} \right)^2 \right) \tag{3.14}$$

where $a_0^{(g)}$, $\nu_0^{(g)}$, and η_d are hyper-parameters. Each hyper-parameter term corresponds bias term, the weight of Gaussian correlation function, and the weight on distance in Gaussian correlation function, respectively. Therefore, in $\boldsymbol{R}$ matrix, we have $p + 2q$ number of hyper-parameters.

Since $\boldsymbol{A}$ should be positive definite matrix, using the Cholesky transformation, $\boldsymbol{A}$ can be divided into $\boldsymbol{L}\boldsymbol{L}^T$, where $\boldsymbol{L}$ is lower triangular matrix and the diagonal elements are non-negative. Now, unknown $\boldsymbol{B}$ matrix is a function of $\boldsymbol{L}$ matrix. The elements of $\boldsymbol{L}$ should be set as hyper-parameters, and we have $\frac{q(q+1)}{2}$ number of hyper-parameters related to the covariance between multiple responses.

Now, for an arbitrary hyper-parameters, the covariance matrix $\boldsymbol{C}$ can be calculated. The size of $\boldsymbol{C}$ is $(qn \times qn)$. For $\frac{q(q+5)}{2} + p$ number of unknown hyper-parameters, Maximum Likelihood Estimation (MLE) is performed. The equation of likelihood L is shown in Eq. (3.15) [75].

$$\begin{aligned} L = & -\log\left[\det \boldsymbol{C}\right] - \log\left[\det\left[\boldsymbol{F}^T \boldsymbol{C}^{-1} \boldsymbol{F}\right]\right] \\ & - \left(\boldsymbol{y}_{aug,FEC-MRK} - \boldsymbol{F}\hat{\boldsymbol{\mu}}\right)^T \boldsymbol{C}^{-1} \left(\boldsymbol{y}_{aug,FEC-MRK} - \boldsymbol{F}\hat{\boldsymbol{\mu}}\right) \\ \hat{\boldsymbol{\mu}} = & \left(\boldsymbol{F}^T \boldsymbol{C}^{-1} \boldsymbol{F}\right)^{-1} \boldsymbol{F}^T \boldsymbol{C}^{-1} \boldsymbol{y}_{aug,FEC-MRK} \end{aligned} \tag{3.15}$$

with $\boldsymbol{F} = \mathbf{1}_n \otimes \boldsymbol{I}_q$ where $\mathbf{1}_n$ denotes an n-dimensional vector with ones. $\hat{\boldsymbol{\mu}}$ denotes the GLS estimator [83] and $\boldsymbol{y}_{aug,FEC-MRK} = [\boldsymbol{y}_1^T, \boldsymbol{y}_2^T, \cdots, \boldsymbol{y}_n^T]^T = [y_{11}, \cdots, y_{1q}, y_{21}, \cdots, y_{2q}, \cdots, y_{n1}, \cdots, y_{nq}]^T$ is an augmented vector of observed response variables.

Using the optimized hyper-parameters, the posterior probability of Kriging prediction at the trial location $\hat{\boldsymbol{x}}$ can be obtained as below,

$$
\begin{aligned}
p\left(\hat{\boldsymbol{y}} | \boldsymbol{y}_{aug,FEC-MRK}\right) &= G\left(\boldsymbol{\mu}(\hat{\boldsymbol{y}}), \boldsymbol{\sigma}^2(\hat{\boldsymbol{y}})\right) \\
\boldsymbol{\mu}(\hat{\boldsymbol{y}}) &= \hat{\boldsymbol{\mu}} + \hat{\boldsymbol{C}}\boldsymbol{C}^{-1}\left(\boldsymbol{y}_{aug,FEC-MRK} - \boldsymbol{F}\hat{\boldsymbol{\mu}}\right) \\
\boldsymbol{\sigma}^2(\hat{\boldsymbol{y}}) &= \boldsymbol{B} - \hat{\boldsymbol{C}}\boldsymbol{C}^{-1}\hat{\boldsymbol{C}}^T + \boldsymbol{U}\left(\boldsymbol{F}^T\boldsymbol{C}^{-1}\boldsymbol{F}\right)^{-1}\boldsymbol{U}^T
\end{aligned}
\tag{3.16}
$$

where $\boldsymbol{U} = \boldsymbol{I}_q - \hat{\boldsymbol{C}}\boldsymbol{C}^{-1}\boldsymbol{F}$ and $\hat{\boldsymbol{C}} = (Cov(\boldsymbol{y}(\hat{\boldsymbol{x}}), \boldsymbol{y}(\boldsymbol{x}_1)), Cov(\boldsymbol{y}(\hat{\boldsymbol{x}}), \boldsymbol{y}(\boldsymbol{x}_2)), \cdots, Cov(\boldsymbol{y}(\hat{\boldsymbol{x}}), \boldsymbol{y}(\boldsymbol{x}_n)))$. The size of $\hat{\boldsymbol{C}}$ matrix is $(q \times qn)$.

3.1.3 Comparisons between RC-MRK and FEC-MRK

The key difference between two multi-response Kriging is how to handle the covariance matrix between responses and the number of hyper-parameters. In RC-MRK, the covariance matrix between multivariate responses, $\boldsymbol{B}$, can be separated to the spatial covariance matrix $\boldsymbol{Q}$ by Kronecker product as shown in Eq. (3.6). To put it another way, each covariance between responses is expressed as a single unknown constant $(b_{11}, b_{12}, b22, \cdots, b_{qq})$, and these values are multiplied to the spatial covariance directly. Since $\boldsymbol{B}$ and $\boldsymbol{Q}$ matrices are separated, the method can be extended to the case of different sample number and locations for different responses.

In FEC-MRK, the covariance matrix between different responses is tightly combined with

Table 3.1: Comparison of the number of hyper-parameters in various GPR models

	Single response GPR	RC-MRK	FEC-MRK
Covariance between samples	$q(p+3)$	$p+3$	$p+3q$
Covariance between responses	0	$\frac{q(q+3)}{2}$	$\frac{q(q+1)}{2}$
Total	$q(p+3)$	$p+\frac{q(q+1)}{2}+3$	$p+\frac{q(q+5)}{2}$

the spatial covariance matrix $\boldsymbol{R}$, which is non-separable dependence covariance structure, as shown in Eq. (3.11) and Eq. (3.12). Since the covariance matrix of response and spatial covariance matrix are coupled to each other, the meta-model is not able to be used for different sample number and locations in different responses. However, the method has much more flexibility in the form of covariance matrix of responses. While the correlation function between responses in RC-MRK is set as a single constant, which is not a function of any variate, FEC-MRK can use the correlation function as a function of response variate. For example, using Gaussian correlation function, $\sigma_{g,h}$ component in Eq. (3.13) which will be multiplied to the spatial covariance matrix between $\boldsymbol{x_i}$ and $\boldsymbol{x_j}$ can be expressed as $b_{gh} \times \exp\left[|y_{g,i} - y_{h,j}|^2\right]$.

Since the form of covariance matrix $\boldsymbol{C}$ is different in two meta-model, the number of hyper-parameter in MLE process is different. Table 3.1 and Fig.3.1 show the comparison of the number of hyper-parameters for single-response GPR model, RC-MRK, and FEC-MRK. It is assumed that the correlation function in Eq. (3.5) is used for the covariance matrix for all the cases. As shown in the table and graph, the number of hyper-parameters for single-response GPR is always larger than multi-response Kriging since we need separate responses for each output. FEC-MRK has $2q-3$ more hyper-parameters compared to RC-MRK. Since we will deal with $q > 1$, FEC-MRK always has more hyper-parameters than RC-MRK.

For example, if we are constructing a GPR model with two input covariates and three response covariates, the number of hyper-parameters in RC-MRK is 14, and the number of hyper-parameters in FEC-MRK is 17, while single-response GPR model uses only 5 for

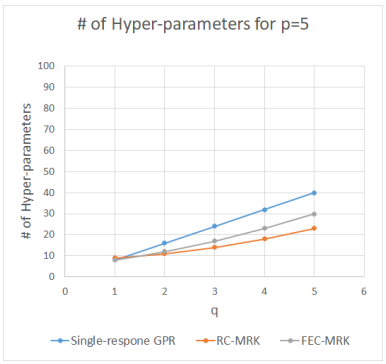

(a) The number of input variates = 5

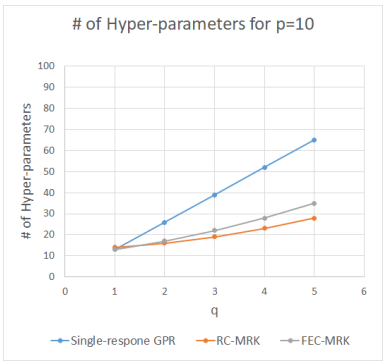

(b) The number of input variates = 10

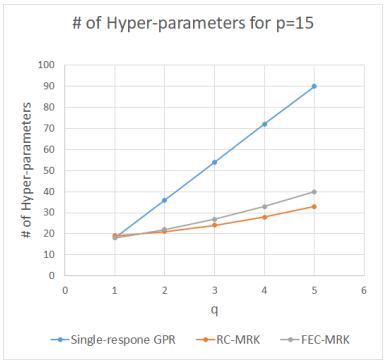

(c) The number of input variates = 15

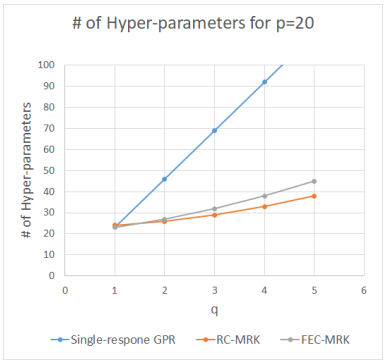

(d) The number of input variates = 20

Figure 3.1: The comparison of the number of hyper-parameter for different number of input and output variate

each response. However, since three single-response GPR models should be constructed separately, total number of hyper-parameters for single-responses GPR model will be 15.

3.1.4 Iterative method for Maximum Likelihood (iMLE) Estimation

Even the number of hyper-parameters are the largest for single-response GPR model, the number of hyper-parameters, which should be calculated in a single model, remains small. However, in multi-response GPR model, the number of hyper-parameters is remarkably increases in a single model since the covariance between responses are set as unknown variable.

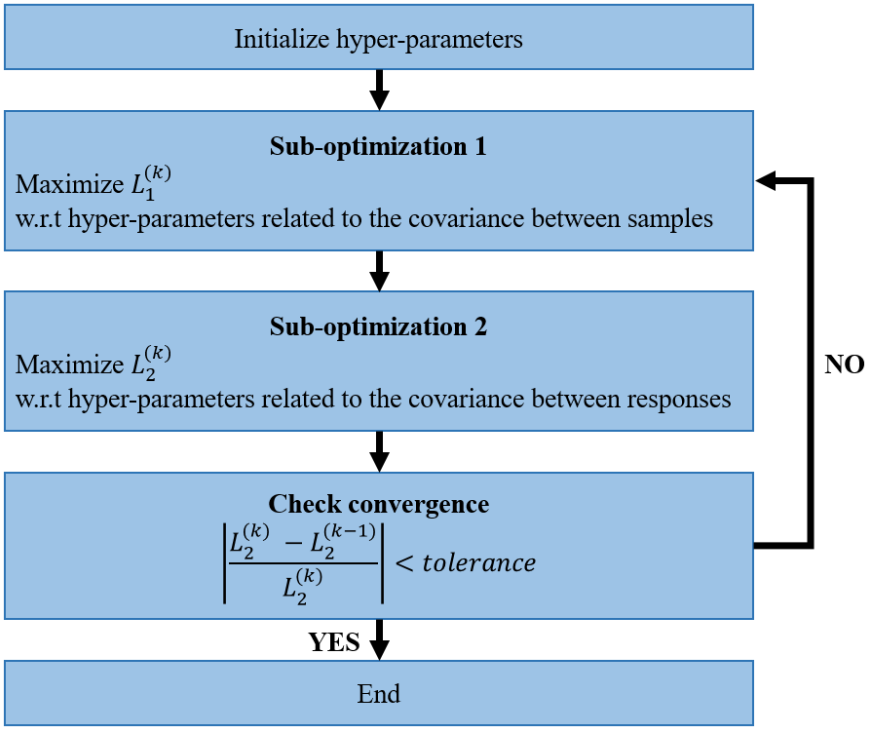

Figure 3.2: The schematics of iterative Maximum Likelihood Estimation (k = iteration number)

As the number of variables in the optimization of MLE process increases, the stability of optimization decreases, and the chance to find optimum hyper-parameter is reduced. To guarantee the accuracy of MLE process, iterative Maximum Likelihood Estimation(iMLE) process is developed and applied to two multi-response GPR models.

The schematics of iMLE process is shown in Fig. 3.2. The iMLE process separates hyper-parameters into two groups; hyper-parameters for the spatial covariance between samples and hyper-parameters for the covariance between responses. Each group of hyper-parameters are optimized through two separated sub-optimization in order.

First of all, hyper-parameters are initialized with constant numbers. In the next step, which is sub-optimization 1 in Fig.3.2, the hyper-parameters for the covariance between samples are optimized to have maximum likelihood. Non-linear Gauss-Seidel method [84], which is

gradient-based optimization, is used. To avoid the numerical instability of matrix inversion during the optimization process, the range of design variable is restricted with step size Δ.

For example, in RC-MRK model, the initial values of hyper-parameters are set as $a_0^{(0)}$, $a_1^{(0)}$, $\nu_0^{(0)}$, $\eta_d^{(0)}$, $S_{11}^{(0)}$, $S_{22}^{(0)}$, $\cdots$, $S_{qq}^{(0)}$, $\phi_{11}^{(0)}$,$\phi_{21}^{(0)}$,$\phi_{22}^{(0)}$, $\cdots$ $\phi_{qq}^{(0)}$. Then, the maximum likelihood L_1 is optimized w.r.t a_0, a_1, ν_0, η_d, and S_{11}, S_{22}, $\cdots$, S_{qq}. The range of design variables are set as $\pm\Delta$ of initial values. The hyper-parameters for the covariance between response are fixed as same as initial values. The detailed definition of the optimization problem of this step is shown below.

$$
\begin{aligned}
\text{maximize} \quad & \textit{Likelihood } L_1^{(1)} \\
\text{w.r.t} \quad & a_0, a_1, \nu_0, \eta_d, S_{11}, S_{22}, \cdots, S_{qq}, \\
\text{subject to} \quad & a_0^{(0)} - \Delta \le a_0 \le a_0^{(0)} + \Delta, \\
& a_1^{(0)} - \Delta \le a_1 \le a_1^{(0)} + \Delta, \\
& \nu_0^{(0)} - \Delta \le \nu_0 \le \nu_0^{(0)} + \Delta, \\
& \eta_d^{(0)} - \Delta \le \eta_d \le \eta_d^{(0)} + \Delta, \\
& S_{11}^{(0)} - \Delta \le S_{11} \le S_{11}^{(0)} + \Delta, \\
& \qquad \vdots \\
& S_{qq}^{(0)} - \Delta \le S_{qq} \le S_{qq}^{(0)} + \Delta, \\
& \phi_{11} = \phi_{11}^{(0)}, \phi_{21} = \phi_{21}^{(0)}, \phi_{22} = \phi_{22}^{(0)}, \cdots \phi_{qq} = \phi_{qq}^{(0)}
\end{aligned}
\tag{3.17}
$$

In the third step, the hyper-parameters for the covariance between responses are optimized to have maximum likelihood. In this optimization process, as same as the previous sub-optimization, the range of design variables are set as $\pm\Delta$ of initial values. The hyper-parameters related to the spatial covariance are set as the value which is obtained in the previous step. In RC-MRK model, the optimization problem can be written as below.

$$
\begin{aligned}
&\text{maximize} && \textit{Likelihood } L_2^{(1)} \\
&\text{w.r.t} && \phi_{11}, \phi_{21}, \phi_{22}, \cdots, \phi_{qq}, \\
&\text{subject to} && \phi_{11}^{(0)} - \Delta \le \phi_{11} \le \phi_{11}^{(0)} + \Delta, \\
& && \phi_{21}^{(0)} - \Delta \le \phi_{21} \le \phi_{21}^{(0)} + \Delta, \\
& && \phi_{22}^{(0)} - \Delta \le \phi_{22} \le \phi_{22}^{(0)} + \Delta, \\
& && \qquad \vdots \\
& && \phi_{qq}^{(0)} - \Delta \le \phi_{qq} \le \phi_{qq}^{(0)} + \Delta, \\
& && a_0 = a_0^{(1)}, a_1 = a_1^{(1)}, \nu_0 = \nu_0^{(1)}, \eta_d = \eta_d^{(1)}, S_{11} = S_{11}^{(1)}, \cdots S_{qq} = S_{qq}^{(1)}
\end{aligned}
\tag{3.18}
$$

where $a_0^{(1)}$, $a_1^{(1)}$, $\nu_0^{(1)}$, $\eta_d^{(1)}$, $S_{11}^{(1)}$, $S_{22}^{(1)}$, $\cdots$ $S_{qq}^{(1)}$ are the hyper-parameters for the spatial covariates which are obtained from Eq. (3.17). The process is iterate until the relative error of L_2 is less than the tolerance. (The fourth step in Fig.3.2) In this paper, strong termination criteria is applied; the error should be less than $1.0E-10$.

3.2 MRK for Variable Fidelity Optimization

Multi-response Kriging model can be implemented into variable-fidelity optimization in various ways. First of all, for the single-fidelity optimization process, multi-response Kriging can be used for the construction of Kriging model for different fidelity samples. In other words, multi-response Kriging can replace the single-response Kriging in Step 2.a of Figure 2.5.

Figure 3.3 shows an example for the use of multi-response Kriging in variable fidelity optimization. If we have two fidelity analysis methods of potential flow solver and RANS solver, in the previous chapter, for the error estimation between two different fidelity data set, two single response Kriging models are constructed separately as shown in Figure 3.3a. However,

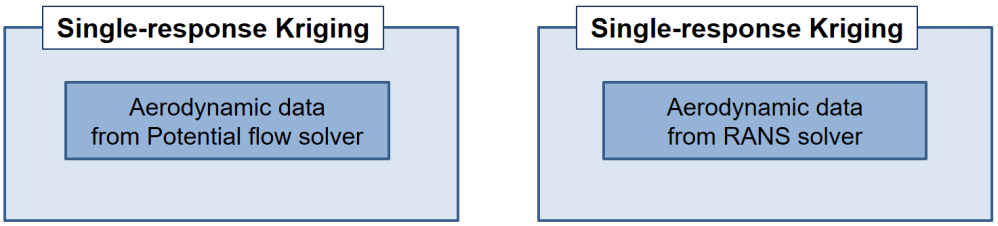

(a) Single response Kriging for variable fidelity optimization

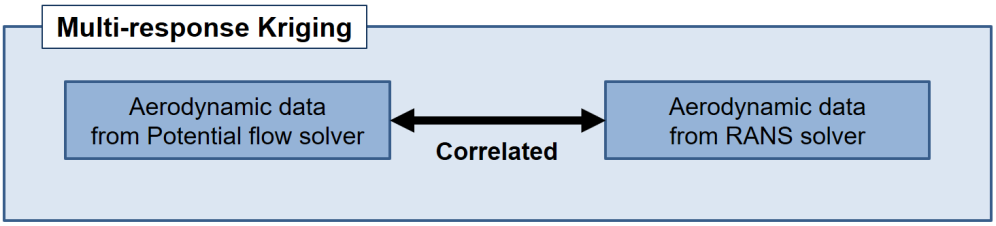

(b) Multi response Kriging for variable fidelity optimization

Figure 3.3: Example of Kriging in variable fidelity optimization

recalling the assumption of sample calibration in the previous chapter, it is assumed that the set of data in different fidelities are correlated, because they are describing same phenomena. Therefore, rather than using separate single-fidelity Kriging models, multi-response Kriging model of two different fidelity sample set can be constructed as shown in Figure 3.3b.

This approach can be extended for the multidisciplinary problem as well. Let's assume that we have two different disciplines of aerodynamic and structural analysis for the aeroelasticity design problem. For the aerodynamic analysis, two different fidelity analysis method of potential flow solver and RANS solver is selected. For the structural analysis, two different fidelity analysis of simple spring model and finite element method(FEM) can be selected.

In this case, since each disciplines are correlated each other, multi-response Kriging model can be constructed for separate fidelities as shown in Figure 3.4a. Otherwise, since the disciplines are correlated with physics, and fidelities are correlated by the assumption of variable fidelity analysis, all four of the data can be constructed together into one multi-response Kriging as shown in Figure 3.4b.

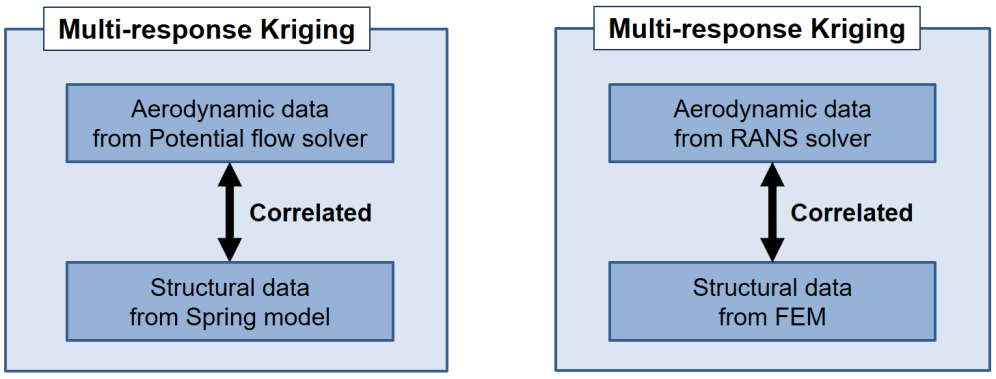

(a) Multi-response Kriging for different disciplines

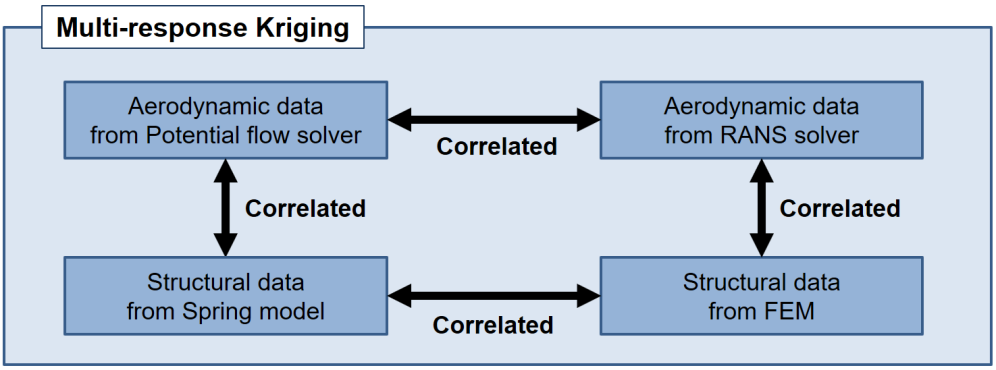

(b) Multi-response Kriging for different disciplines and different fidelity

Figure 3.4: Example of the use of multi-response Kriging in variable fidelity multidisciplinary design problem

In the second case, the main issue will be the size of total covariance matrix. As discussed in Section 3.1.3, as the number of responses q increases, the size of total covariance matrix, which is $(qn \times qn)$ increases, and the number of hyper-parameter increases as well. Since the total covariance matrix is a full matrix, if the size of the matrix increases, numerical issue in matrix conversion can be easily occurred. Moreover, due to the increase number of unknown hyper-parameters, the sub-optimization process for searching the proper hyper-parameters will become much more difficult. Therefore, to use multi-response Kriging in multidisciplinary and variable fidelity optimization problem, further studies about these numerical issues will be required.

Chapter 4

Validations

In this chapter, the validations of developed design methodologies, variable fidelity analysis, dynamic sampling, dynamic fidelity indicator, and multi-response Kriging, are carried out. For the validation, various types of analytic functions are used. The mathematical formulation of analytic function and the statement of problems for the validations are introduced in the following sections.

4.1 Infill sampling criteria

This section shows the validation of infill sampling criteria applied to the single-fidelity and single-disciplinary problem in Section 2.3.2. For the validation of efficiency, both balancing and dynamic switching approaches are implemented into Efficient Global Optimization design framework. The approximated q-EI method [49] is also implemented into EGO framework, and the result is compared with developed methods.

Optimization problems with simple constraints of bounds on design variables is set for two 2D analytic functions: a six-hump camel back function [85, 86] and a Matlab peak function [87]. Two functions have different characteristics in terms of local and global minima and the degree of non-linearity. The mathematical formulation of a six-hump camel back function is shown in Eq. (4.1). The six-hump camel back function has two global minima at $(x_1, x_2) = (-0.0898, 0.7126), (0.0898, -0.7126)$. The minimum function value is -1.0316. The contour

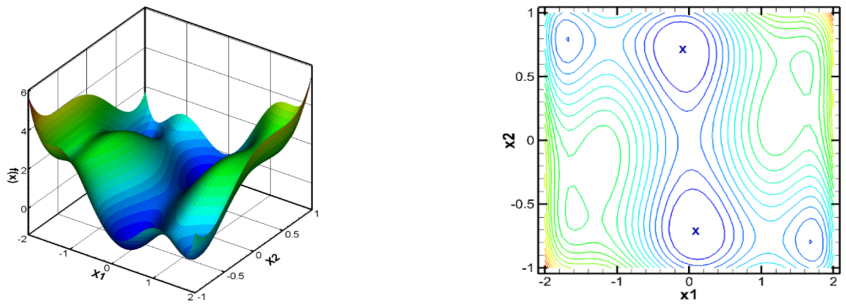

(a) Configuration (b) Iso-contour

Figure 4.1: Configurations and iso-contours of six-hump camel back function

of the function is shown in Figure 4.1. The locations of minima is displayed with the symbols of '×' in blue.

$$\begin{aligned} f &= \left(4 - 2.1x_1^2 + \frac{x_1^4}{3}\right) x_1^2 + x_1 x_2 + \left(-4 + 4x_2^2\right) x_2^2, \\ & x_1 \in [-2, 2],\ x_2 \in [-1, 1] \end{aligned} \tag{4.1}$$

The mathematical formulation of a Matlab peak function is shown in Eq. (4.2). The Matlab peak function has one local minima and one global minima at $(x_1, x_2) = (0.2282, -1.6255)$. The minimum function value is -6.551133. The contour of the function is shown in Figure 4.2.

$$\begin{aligned} f =& 3\left(1 - x_1\right)^2 \exp\left[-x_1^2 - \left(x_2 + 1\right)^2\right] \\ & - 10\left(\frac{x_1}{5} - x_1^3 - x_2^5\right) \exp\left[-x_1^2 - x_2^2\right] - \frac{1}{3}\exp\left[-\left(x_1 + 1\right)^2 - x_2^2\right], \\ & x_1 \in [-3, 3],\ x_2 \in [-3, 3] \end{aligned} \tag{4.2}$$

The best performance of infill sampling in EGO framework is defined as the ability to find

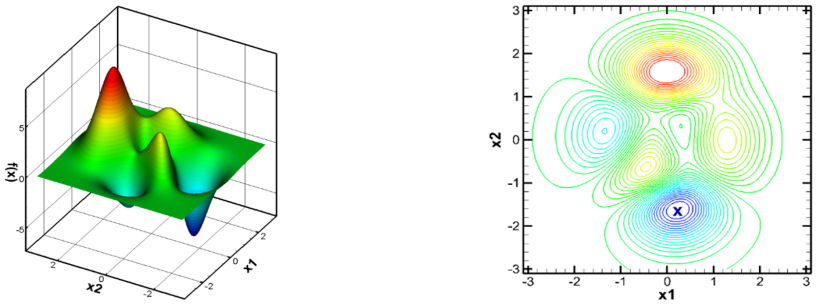

(a) Configuration (b) Iso-contour

Figure 4.2: Configurations and iso-contours of Matlab peak function

exact optimum/optima at low cost as possible. As the overall quality of the surrogate model should be addressed by the local and global accuracies, two metrics are defined. First, to check the solution optimality, or the local accuracy, two relative errors are computed: the metrics of difference in $\boldsymbol{x}$ location between the optimizer and the true minimum, ϵ_x, and the difference in function value of f, ϵ_f. Those are formulated in Eq. (4.3), where the value of $\bar{f}^*$ represents the predicted minimum, and f_{min} is the true optimum at $\boldsymbol{x}_{min}$. Second, a total of 2,500 validation points are evenly distributed in two-dimensional design space, and root mean square error (RMSE) is calculated between the predicted function value and the exact function values at the validation points. This value stands for the global accuracy of the surrogate model.

$$\epsilon_x = \frac{\|\boldsymbol{x}^* - \boldsymbol{x}_{min}\|}{\|\boldsymbol{x}_{min}\|}, \quad \epsilon_f = \frac{\left|\bar{f}^* - f_{min}\right|}{|f_{min}|} \tag{4.3}$$

4.1.1 Parametric study on dynamic switching approach

Prior to the validation of infill sampling method, a parameter study of a dynamic switching approach is performed. Dynamic switching approach involves three parameters: a switching parameter, κ, a clustering parameter for exploration, θ_G, and a clustering parameter for

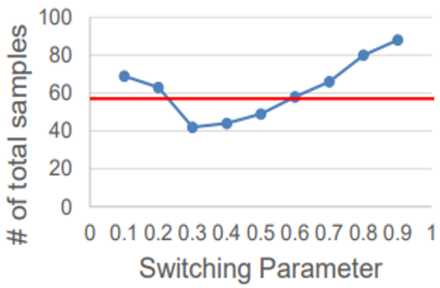

(a) $\theta_G = 0.3$, $\theta_L = 0.01$

(b) $\kappa = 0.3$, $\theta_L = 0.01$

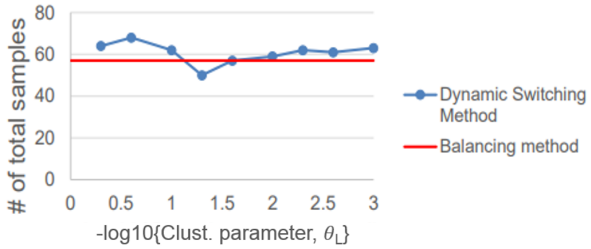

(c) $\kappa = 0.3$, $\theta_G = 0.4$

Figure 4.3: Parameter study results for six hump camel back function

exploitation, θ_L. To carry out the best performance of dynamic switching approach, these parameters should be properly set. Therefore, a parameter study to find optimal parameters is performed with both analytic functions.

Due to the randomness of initial sampling and Genetic algorithm, fifty sets of six initial samples are randomly selected using the Latin Hypercube Sampling method. The total number of samples needed to find the function minimum is averaged over the fifty runs. For both analytic functions, the termination criterion is set for the relative error of optimal function value between current and previous design steps to be less than 10^{-5}. The average number of samples for the convergence is compared with that by the balancing approach.

Figure 4.3 and 4.4 show the results of the parameter study for six hump camel back function and Matlab peak function, respectively, in terms of the average number of total samples for the convergence. In the parametric study, switching parameter and clustering parameter for exploration are varied between zero and one and clustering parameter for exploitation is

(a) $\theta_G = 0.3$, $\theta_L = 0.01$

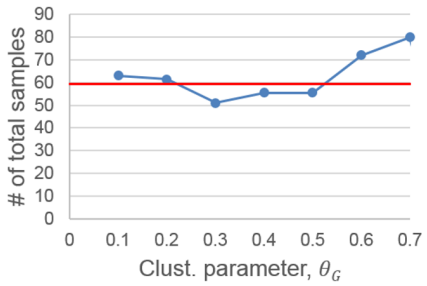

(b) $\kappa = 0.3$, $\theta_L = 0.01$

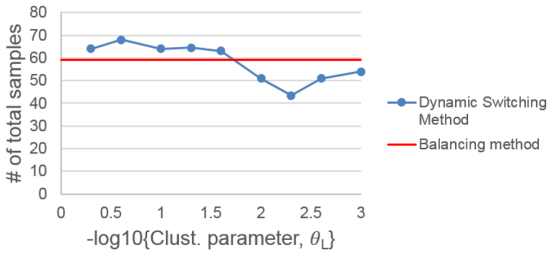

(c) $\kappa = 0.3$, $\theta_G = 0.4$

Figure 4.4: Parameter study results for Matlab peak function

varied from 0.001 to 0.1, relatively, while two other parameters are fixed. It is shown that an optimal range for the minimal number of required sample points exists for all parameters, $\kappa = 0.3$, $\theta_G = 0.3 \sim 0.4$, and $\theta_L = 0.05 \sim 0.005$. These values are used in further studies. However, it should be noted that the determination of a single parameter that is optimal for all types of design problems is difficult, and a certain amount of inefficiency is inevitable in our approach if used for other design problems. However, the values ranging from 0.2 to 0.5 for κ and θ_G, and from 0.002 to 0.1 for θ_L appear to be reasonable not showing much sensitivity.

4.1.2 Cost comparison

In this section, the cost efficiency of developed method is validated. For the validation, three types of the ISC methods are used: 1) the MPMO-ISC method with the balancing approach, 2) the MPMO-ISC method with the dynamic-switching approach, and 3) the approximated

q-EI method. For the approximated q-IE method, three different approximations to the maximum EI value are used: Kriging Believer (KB), and Constant Liars (CL) with a minimum (CLmin) and a maximum (CLmax). For the MPMO-ISC method with the dynamic switching approach, the parameters which are found in the previous parameter study is used.

Starting from a total of six initial sample points, adaptive sample points of three (or less if clustering is detected) are added at each design iteration to update the Kriging surrogate model, and performance metrics are computed correspondingly. The termination criteria are the values of ϵ_x and ϵ_f to be less than 0.01%. To mitigate the randomness in the set of initial samples for the surrogate model construction and in the population of the genetic algorithm for optimization, a total of 50 different sets of initial points are randomly chosen using the Latin Hypercube Sampling (LHS) method. For each set, the average number of required samples is averaged, and compared with each other infill sampling strategy. The values of average, standard deviation, and the minimum number of total required sample points for convergence, are summarized in Table 4.1 and 4.2 for each method.

For both six-hump camel back function and Matlab peak function, the results of the MPMO-ISC with the balancing approach and the dynamic switching approach demonstrate the best performance at the lowest computation cost as shown in Table 4.1 and 4.2. For the Matlab peak function case, the dynamic switching approach requires only one more design iteration than balancing approach, which indicates no difference in the computational efficiency. Since the dynamic switching approach needs three parameters which can be varied case by case,

Table 4.1: A total required number of sample points (Six hump camel back function)

	MPMO-ISC (Balancing)	**MPMO-ISC (D. switching)**	**Q-EI (KB)**	**Q-EI (Max.CL)**	**Q-EI (Min.CL)**
Avg. number	54	48	69	74	79
Std. deviation	12	15	16	13	15
Min. number	27	15	42	45	52

Table 4.2: A total required number of sample points (Matlab Peak Function)

	MPMO-ISC (Balancing)	**MPMO-ISC (D. switching)**	**Q-EI (KB)**	**Q-EI (Max.CL)**	**Q-EI (Min.CL)**
Avg. number	51	54	66	78	79
Std. deviation	12	19	16	13	15
Min. number	27	11	36	45	48

standard deviation of the total number of samples was larger than that of the balancing approach. However, once the parameter is set correctly, the total number of samples is dramatically reduced as shown in the row of minimum number of samples; the minimum number of samples for the balancing approach is 27, but the one for the dynamic switching approach is 12.

The approximated q-EI method with the Kriging Behavior, the minimum Constant Liar and the maximum Constant Liar shows about 30% to 55% higher computational cost for the design convergence. Based on the results from the two analytic functions, it is shown that the MPMO-ISC method with both balancing and dynamic switching approaches shows relatively robust and good results. On the other hand, the accuracy of the approximated q-EI method is sensitive to the specific approximation value of the EI. It is not straightforward to decide a priori which approximation value should be used and is difficult to predict the corresponding accuracy and efficiency. However, arbitrariness should be noted in determining parameters for the MPMP ISC methods: the number of infill sample points at each iteration (three in the current case) and the parameter values in the dynamic switching approach.

In summary, in real engineering design applications where the characteristics of the design space are not known in advance, the choice of the MPMO-ISC method becomes reasonable and robust with limited computing resources, guaranteeing both the local and global accuracies.

4.2 EGO Framework with Variable Fidelity Analysis

In this paper, variable fidelity Efficient Global Optimization framework is constructed with variable-fidelity analysis method in Section 2.2, dynamic sampling in Section 2.3, and dynamic fidelity indicator in Section 2.4. The schematic of framework is shown in Figure 2.5. In this section, the validation of the developed methods and the variable fidelity EGO framework is performed with two analytic functions of six hump camel back function and simplified Rastrigin function. First, cost saving is shown in comparison to that of the high fidelity design, followed by the sensitivity to the filtering criterion.

4.2.1 Cost comparison

As the first validation, the cost efficiency of variable fidelity EGO framework is compared with the optimization process with high fidelity sample analysis only. In this validation, the reduction of the total cost in variable fidelity EGO framework should be observed while the optimum result is same with high fidelity case. For the comparison of cost efficiency, a metric of the computational cost factor (CCF) is defined to take into account the number of samples and computational cost associated with each analysis fidelity.

$$CCF = \sum_{m=1}^{r} a_m \times n_m, \tag{4.4}$$

where a_m is the cost factor for the mth fidelity function analysis, and n_m is the number of mth fidelity analysis, where $m = 1, 2, \cdots, r$. Although there is no difference in the computational cost for the analytic function of different fidelity, the ratio of 0.1, 1.0, and 6.0 is set for the low-, medium-, and high-fidelity function analyses which correspond to the CFD computations needed for the tailless aircraft (see Sec. 5.3) by panel, Euler and the

Reynolds-averaged Navier-Stokes (RANS) solvers, respectively.

To check the accuracy and convergence of the design framework, two metrics are set; 1) the normalized root mean square error (NRMSE) of the surrogate model at pre-specified points and 2) the prediction error between the Kriging prediction and the high fidelity analysis at the same location. Those two metrics are representative of the global and the local accuracy of the surrogate model, respectively. A total of $2,601(51 \times 51)$ sample points are pre-selected evenly in x_1 and x_2 directions. The NRMSE is defined as

$$NRMSE = \frac{\sqrt{\frac{1}{n}\sum_{i=1}^{2601}(\hat{f}^{VF}(x_i) - f_{exact}(x_i))^2}}{|\max(f_{exact}) - \min(f_{exact})|} \times 100. \tag{4.5}$$

Six hump camel back function (SHCBF)

First, the six hump camel back function [85, 86] in the previous section is used for the validation. For the variable fidelity design, the exact function is used as the high fidelity analysis, and the low- and medium-fidelity functions, f_{medium} and f_{low} are created by adding arbitrary noises as shown in Eq. (4.6), respectively. Figure 4.5 illustrate the contours in two- and three-dimensional plots.

$$\begin{aligned} f_{SHCBF,exact}(x_1, x_2) &= (4 - 2.1x_1^2 + 1/3x_1^4)^2 x_1^2 + x_1 x_2 + (-4 + 4x_2^2)x_2^2 \\ f_{medium}(x_1, x_2) &= 1.2 \times f_{SHCBF,exact}(x_1 + 0.05, x_2 - 0.05) + 0.3 \\ f_{low}(x_1, x_2) &= 0.7 \times f_{SHCBF,exact}(x_1 - 0.1, x_2 + 0.1) + 0.5 \end{aligned} \tag{4.6}$$

Initially, the total number of 12, 8, and 4 sample points were selected for low-, medium-, and high-fidelity analysis, respectively, and four infill samples are added at each design

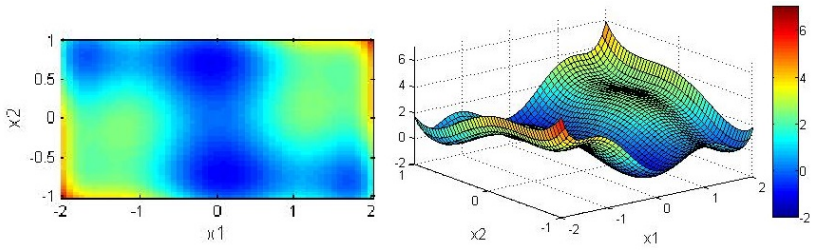

(a) Exact function (assumed highest-fidelity)

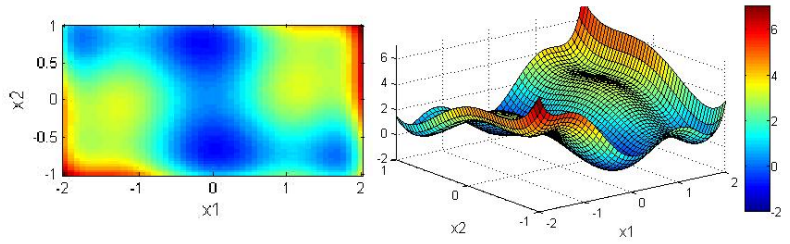

(b) Medium-fidelity function

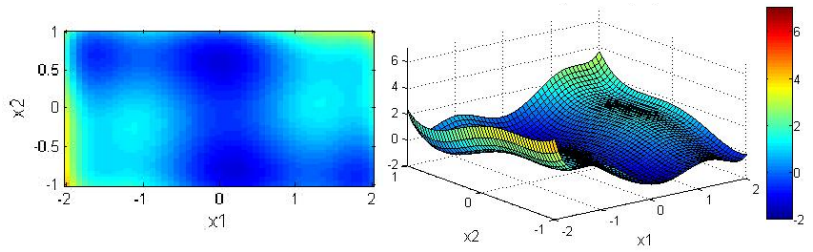

(c) Low-fidelity function

Figure 4.5: 2D contour and 3D plot of six hump camel back function with different fidelities

iteration; one sample is calculated with high fidelity analysis at the current optimum for the error estimation and three samples are from infill sampling of MPMO-ISC. The high fidelity design was carried out independently with the same four high-fidelity sample points used initially for the VF design.

The termination criterion is set 0.5% for the Kriging prediction error at the optimum. After six design iterations for the variable fidelity design with the addition of 16 low-, 11 medium-, and 16 high-fidelity samples (see Figure 4.6. L, M, H represent the number of low-, medium-, and high-fidelity samples), the optimum point was found, whereas the HF design added 25 high-fidelity infill sample points to converge. Fig. 4.7 shows the direct comparison of the

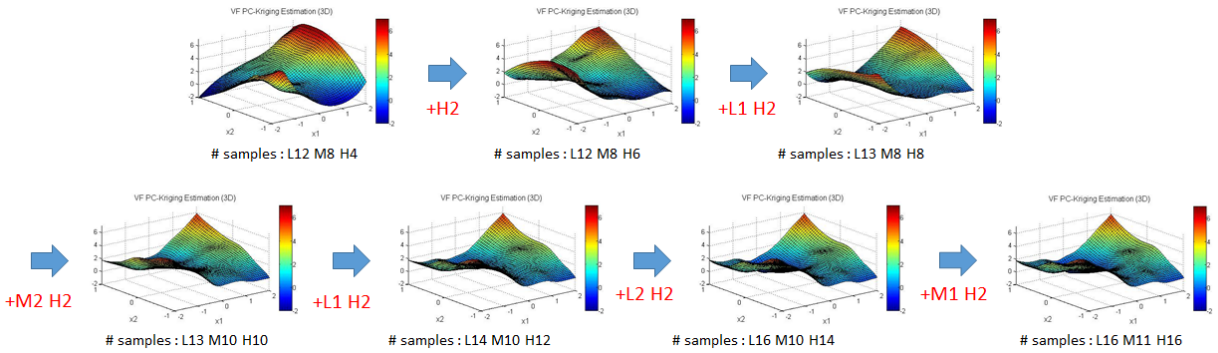

Figure 4.6: Design history of 3D plots of VF optimization framework for six hump camel back function

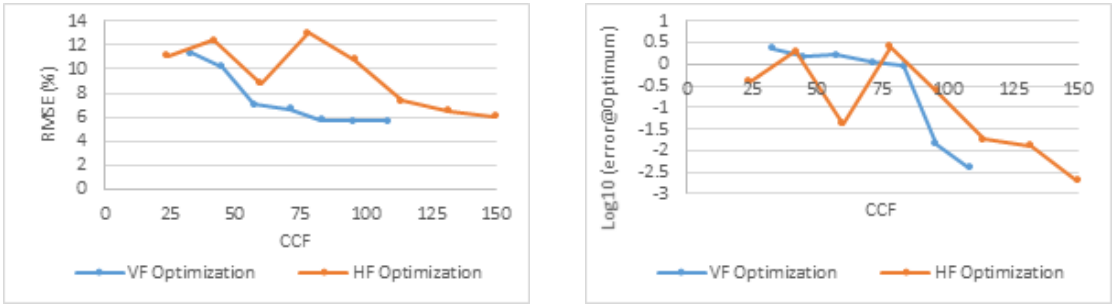

(a) History of NRMSE (b) History of Kriging error @ Opt

Figure 4.7: Comparison of variable fidelity and high fidelity optimization for six hump camel back function

convergence over design iteration between the variable fidelity and the high fidelity design in terms of the NRMSE and the Kriging prediction error at the optimum. The variable fidelity design found the optimum at the CCF of 110, while the high fidelity design needed the CCF of 150, at 27.6% less cost, which is mostly attributed to sparing high fidelity analyses.

Simplified Rastrigin function (SRF)

The second test function is the simplified Rastrigin function [88] which is one of the canonical problems with high non-linearity and multi-modality. The exact, medium- and low-fidelity simplified Rastrigin functions are formulated in Eq. (4.7). The exact simplified Rastrigin

function formulated is a slight variation of the original function such that it has the reduced number of local minima from 80 to 24, but it still has the same global minimum at $(0, 0)$. The two- and three-dimensional contours of those functions are shown in Fig. 4.8.

$$\begin{aligned} f_{SRF,exact}(x_1, x_2) &= 20 + \sum_{i=1}^{2} [x_i^2 - 10\cos(\pi x_i)] \\ f_{medium}(x_1, x_2) &= 0.8 \times f_{SRF,exact}(x_1 + 0.1, x_2 - 0.1) + 5.0 \\ f_{low}(x_1, x_2) &= 13 + 0.9 \sum_{i=1}^{2} [x_i^2 - 10\cos(0.5\pi x_i)] \\ -5.12 \le x_1 \le 5.12, &\quad -5.12 \le x_2 \le 5.12 \end{aligned} \tag{4.7}$$

Initially, the total numbers of 30, 25, and 15 sample points were selected for low-, medium-, and high-fidelity analysis, respectively. A relatively large number of initial samples are needed due to more complicated characteristics. Again, the high fidelity design is carried out independently with the 15 initial sample points which were used for the VF design.

The termination criterion is set for the Kriging prediction error at the optimum to be as small as 10^{-4}. The reason for more strict tolerance is to avoid being trapped in one of the numerous local minima. The variable fidelity design was terminated after eight iterations with the infill samples of 34 low-, 32 medium- and 35 high-fidelity analyses. On the other hand, the high fidelity design needed as many as 82 infill sample points to satisfy the specified convergence. Figure 4.9 shows the history of Kriging surrogate model with infill samples added at each iteration. L, M, H represent the number of low-, medium-, and high-fidelity samples.

Figure 4.10 shows the histories of the NRMSE and the Kriging prediction error at the optimum, respectively, in terms of the CCF values. The variable fidelity design found the optimum at the CCF of 245 which is almost half of the CCF for the high fidelity design with

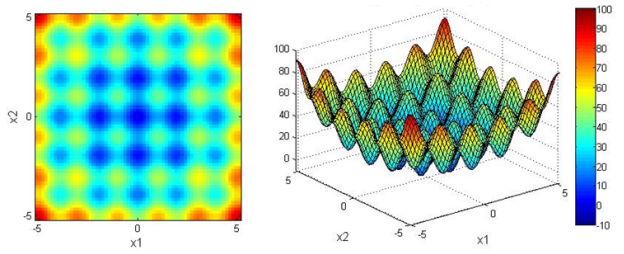

(a) Exact function (assumed highest-fidelity)

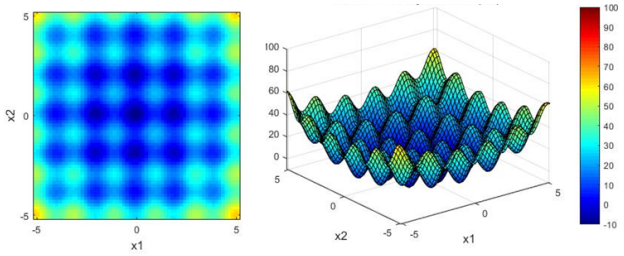

(b) Medium-fidelity function

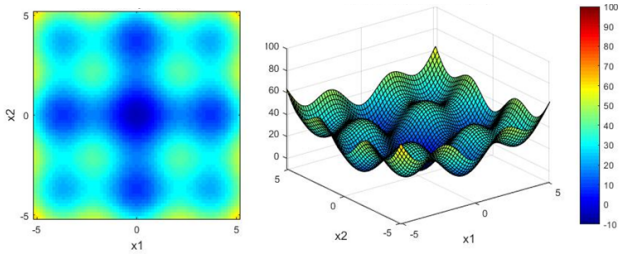

(c) Low-fidelity function

Figure 4.8: 2D contour and 3D plot of simplified Rastrigin function with different fidelities

492.

From the validation, it is shown that using variable-fidelity design framework, the cost of sampling can be hugely saved since both high fidelity data, which is accurate but expansive, and low fidelity data, which is less accurate but cheap, are used together. Especially, it was observed that as the problem became more difficult, the efficiency of variable fidelity design increased because we can use much more information from inexpensive lower fidelity samples.

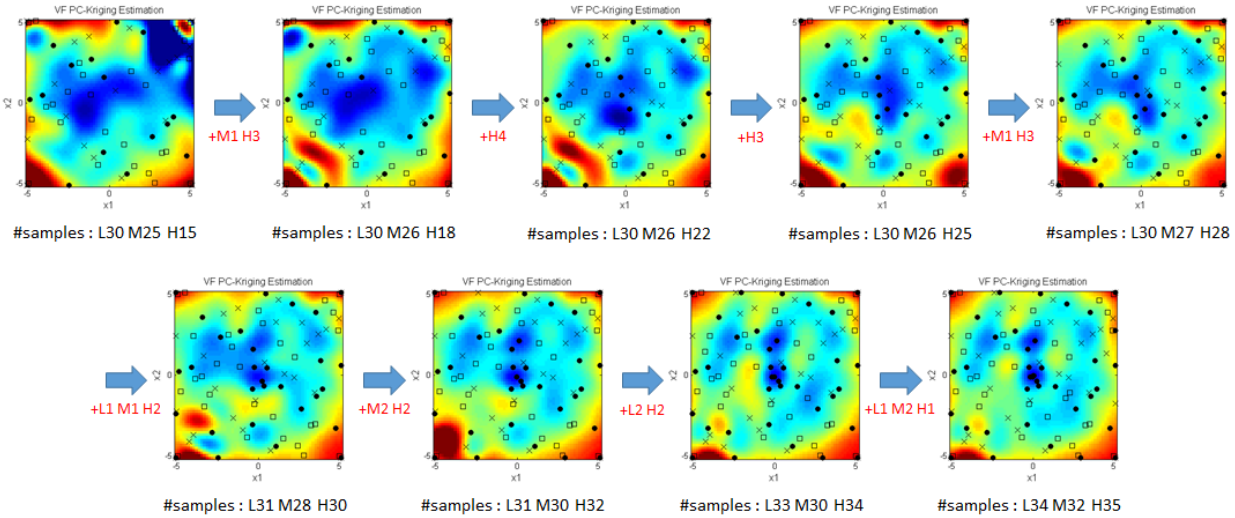

Figure 4.9: Design history of VF optimization framework with the simplified Rastrigin function

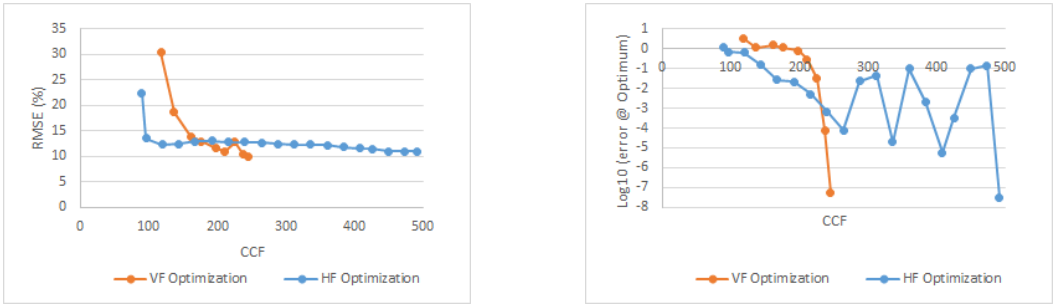

(a) History of NRMSE

(b) History of Kriging error @ Opt

Figure 4.10: Comparison of variable fidelity and high fidelity optimization for simplified Rastrigin function

4.2.2 Sensitivity to filtering criteria

In the variable-fidelity EGO framework, the sample filtering process is important to guarantee the quality of variable fidelity Kriging surrogate model. In sample filtering process, filtering criterion (FC) is set to determine whether the calibrated lower fidelity sample will be filtered out or not. The mathematical formulation of filtering criteria using overlapping coefficient(OVL) is represented in Eq. (2.17) and (2.18), and the threshold OVL value was set to be 0.5 for the validation study in the previous section.

This section discusses the sensitivity of design with respect to the threshold OVL value. In Eq. (2.17), the low threshold value allows lower accuracy for the function analysis whereas the higher threshold value enforces more high fidelity analyses. The design iteration counts and the CCF values are plotted in Figure 4.11 and 4.12 with respect to the varying threshold OVL value varying from 0 to 1.

In Figure 4.11 and 4.12, an optimal threshold value for the filtering criteria appears to be around 0.5 resulting the lowest iteration count and the minimum CCF value, confirming that the value of 0.5 used in the present study appears reasonable. The OVL coefficient of zero means that the design accepts all lower-fidelity sample points without filtering any of them. It is notable that more design iterations and higher CCF are needed with the lower OVL value, which can be explained by the fact that accepting all lower-fidelity sample points deteriorate the accuracy of the variable fidelity surrogate model, thus requiring a larger number high fidelity sample points during the infill sampling procedure. On the other hand, the variable fidelity design with the OVL threshold value of one filters out all sample points of fidelities lower than the highest-fidelity, and cannot benefit from the low-fidelity sample points with relatively good accuracy.

Most importantly, it is observed that filtering out or accepting all low-fidelity points are

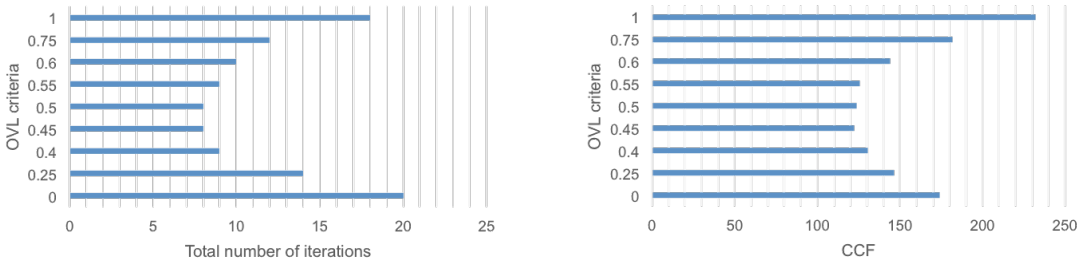

(a) OVL vs. the number of iterations (b) OVL vs. CCF

Figure 4.11: Design iterations and the CCF w.r.t the varying filtering criteria (six hump camel back function)

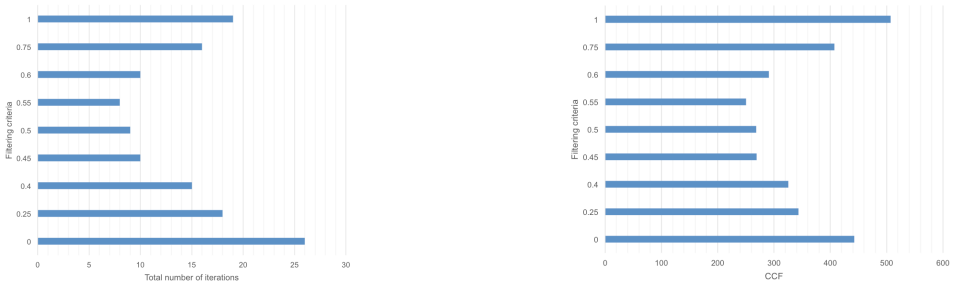

(a) OVL vs. the number of iterations (b) OVL vs. CCF

Figure 4.12: Design iterations and the CCF w.r.t the varying filtering criteria (simplified Rastrigin function)

not most efficient, and there is an optimal overlapping coefficient for the filtering criterion to maximize the computational efficiency. However, exact quantification of the optimal threshold OVL a priori for all types of problems is a difficult problem and the value of 0.5 appears to be reasonable based on our numerical test results.

4.3 Multi-Response Kriging model

In this section, the improvement in global accuracy of multi-response Kriging model is validated with analytic test functions. For the comparison, single response Kriging is constructed as well. Moreover, the multi-response Kriging model and single-response Kriging model are implemented into Efficient Global Optimization (EGO) process, and the local accuracy and efficiency as a surrogate model in the optimization process is verified. In this validation, to focus on the performance of Kriging model, single fidelity optimization problem is selected..

4.3.1 Global accuracy

To validate the improvement in global accuracy using multi-response Kriging model, the global accuracy test is performed. In this test, single- and multi-response Kriging models are constructed for the test analytic functions with multiple discipline and root mean square errors(RMSE) are compared. RMSE is computed by comparing with the exact analytic function with constructed Kriging model. The observed samples are selected using Latin Hypercube Sampling(LHS) [19]. To consider the randomness of Latin Hypercube Sampling, the result of 20 sample sets are averaged.

Weakly coupled function

As the weakly coupled function, the test function by Wang et al is used [27]. The test function has two design variables, and two responses, which are correlated. To enhance the coupling between two responses, the functions are modified as shown in Eq. (4.8). The relation between f_1 and f_2 is shown in Eq. (4.9). Both design variables x_1 and x_2 varies from 0.0 to 5.0. The contours of exact function value are shown in Fig. 4.13.

$$\begin{aligned} f_1 &= 3\cos(x_1) + 4\cos(2x_2) \\ f_2 &= 3/2\cos(x_1 + 1) + 2\cos(2x_2 + 1) \end{aligned} \tag{4.8}$$

$$f_1 - 2f_2 = \sin(1)\,[3\sin(x_1) + 4\sin(2x_2)] \tag{4.9}$$

To compare the RMSE and computational time to find the hyper-parameters of each Kriging model, Monte Carlo simulation [80] has been performed. From 15 number of samples, the

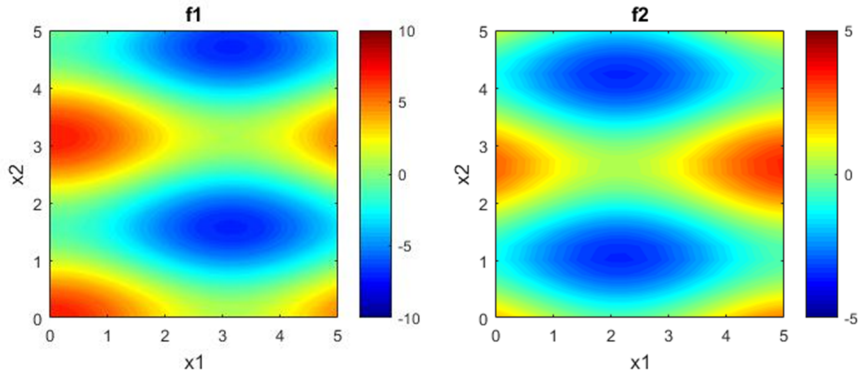

Figure 4.13: The contour of weakly coupled functions

number of sample is increased by 5. For each different number of sample, 20 sample sets are randomly picked using LHS. The RMSE and computational time are averaged for these 20 sample sets. The RMSE is calculated with 21×21 evenly spread test samples.

Figure 4.14 shows the result of global accuracy test for weakly coupled function. For the comparison, the single response Kriging model is constructed by DACE, which is Matlab Kriging code [74]. Since RC-MRK and FEC-MRK methods uses huge matrix inversion and iterative MLE process in Section 3.1.4, the computational time is much larger. While single response Kriging model takes less than a second, multi-response Kriging models take a minutes to 25 minutes by different number of samples. However, since the correlation between responses are considered, the average RMSE is remarkably lower in both multi-response Kriging models.

Strongly coupled function

As a strongly coupled function, the analytic function which is previously solved by Sellar et al is used [89]. The test function has three design variables, and two responses. Since each function is the function of another function, they are strongly correlated by each other response. The functions are as shown below. The sliced contours of exact function value at

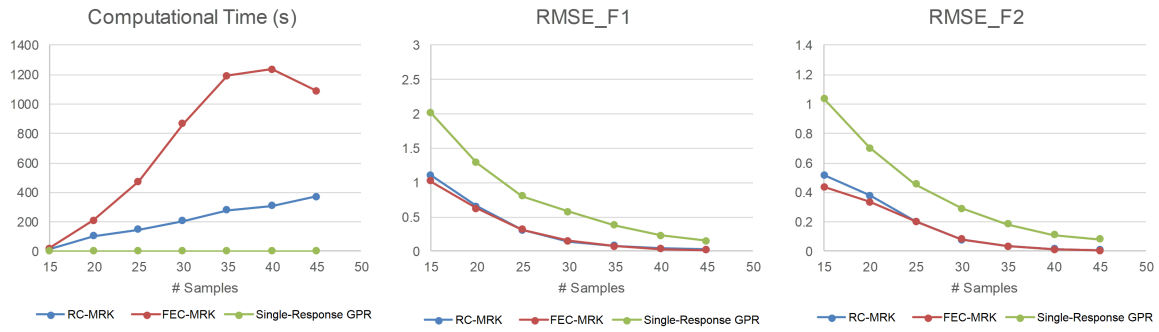

Figure 4.14: The result of global accuracy test for weakly coupled function

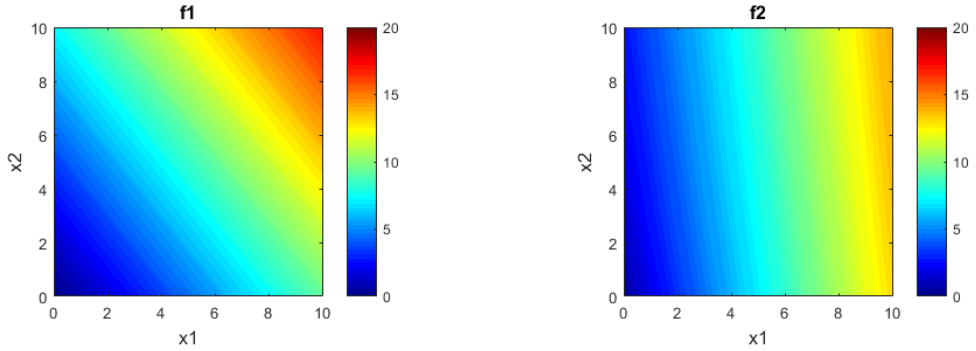

Figure 4.15: The sliced contour of strongly coupled functions ($z_1 = 0$)

$z_1 = 0$ are shown in Fig. 4.15.

$$
\begin{aligned}
f_1 &= z_1^2 + x_1 + x_2 - 0.2 f_2 \\
f_2 &= \sqrt{f_1} + z_1 + x_2 \\
0 &\le x_1 \le 10 \\
0 &\le x_2 \le 10 \\
-10 &\le z_1 \le 10
\end{aligned}
\tag{4.10}
$$

As shown in the previous test, the computational time to find the hyper-parameters of each Kriging model and RMSE is compared. From 15 number of samples, the number of sample

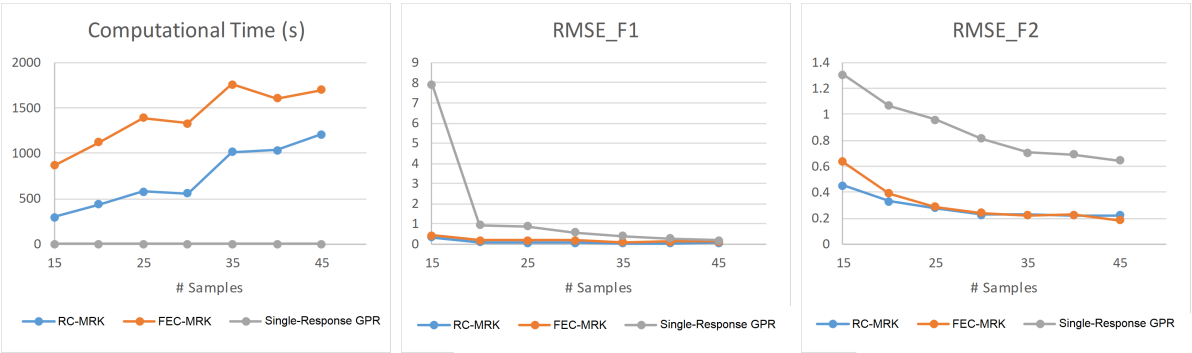

Figure 4.16: The result of global accuracy test for strongly coupled function

is increased by 5. For each different number of sample, 20 sample sets are randomly picked using Latin Hypercube Sampling. The RMSE and computational time is averaged for these 20 sample sets. The RMSE is calculated with $11 \times 11 \times 11$ evenly spread test samples.

Figure 4.16 shows the result of global accuracy test for strongly coupled function. For the comparison, the single response Kriging model is constructed by DACE, which is Matlab Kriging code. As shown in the previous global accuracy test with weakly coupled function, the computational time of multi-response Kriging methods is much larger than single response Kriging model. However, the average RMSE is generally lower in both multi-response Kriging models for all the functions.

From the global accuracy test with weekly and strongly coupled function, it is verified that multi-response Kriging provided us much more accurate function prediction in the overall design space for coupled discipline compared to single-response Kriging model at the same number of sample points. This is due to the effect of covariance between responses. Since multi-response Kriging model includes the correlation between responses in the covariance matrix, much more knowledge can be considered during the construction of surrogate model. The results above indicates us that we can achieve same global accuracy (RMSE) with much smaller number of samples, and it leads huge reduction in the design cost.

However, since iterative Maximum Likelihood Estimation (iMLE) process is used and the size of covariance matrix and the number of hyper-parameters are much larger in multi-response Kriging model, the computational time to construct the model is remarkably increased. While single-response Kriging takes less than a second, multi-response Kriging takes several minutes. However, since high-fidelity analysis, such as RANS simulation, takes several hours even using parallel computing, it will not be a bottle neck in the entire design process.

4.3.2 Local accuracy

The key reason for using multi-response Kriging is multidisciplinary optimization problems. In this section, multi-response Kriging model is implemented into efficient global optimization (EGO), and the local accuracy around the optimum and the cost efficiency in the entire design process is validated. As the optimization problem, analytic functions, which are introduced in the previous section, are used. The number of iterations, the number of samples for the convergence, and RMSE of converged responses are compared for weakly and strongly coupled problems.

Weakly coupled function

The first test comes with weakly coupled function. The weakly coupled functions in the previous subsection is used as two different disciplines, (Eq. 4.8) but the high-level objective functions are added to consider the optimization problem. The problem is described as below. The exact contour of function F is shown in Figure 4.17. The function has one global minimum at (x_1, x_2) =(2.6416,1.2847), and one local minimum.

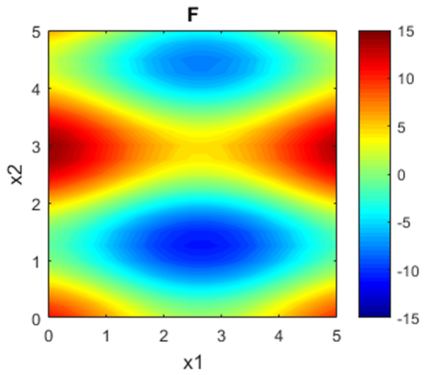

Figure 4.17: The contour of objective function for weakly coupled case

$$\begin{aligned} \underset{x_1,x_2}{\text{minimize}} \quad & F = f_1 + 0.5 f_2 + x_2 \\ \text{subject to} \quad & 0 \leq x_1 \leq 5, \\ & 0 \leq x_2 \leq 5 \end{aligned} \tag{4.11}$$

For this optimization problem, the number of initial samples are set as 10, and randomly picked with Latin Hypercube Sampling. For the comparison, single-response Kriging, RC-MRK and FEC-MRK are used as the surrogate model, and the results are compared. For the construction of single-response Kriging, DACE Matlab Kriging code [74] is used. As the adaptive sampling process, one sample at the optimum of each EGO iteration is added to improve the local accuracy of the surrogate model, and samples at the maximum prediction uncertainty in each surrogate model is added to improve the global accuracy. (It is same with a balancing approach with third point in multi-point multi-objective infill sampling criteria in Section 2.3.2)The design iteration is terminated if the relative error of optimum function value is lower than 10^{-4}. The relative error of optimum function value is calculated as below.

$$error = \left| \frac{F_{opt}^{(k)} - F_{opt}^{(k+1)}}{F_{opt}^{(k)}} \right| \tag{4.12}$$

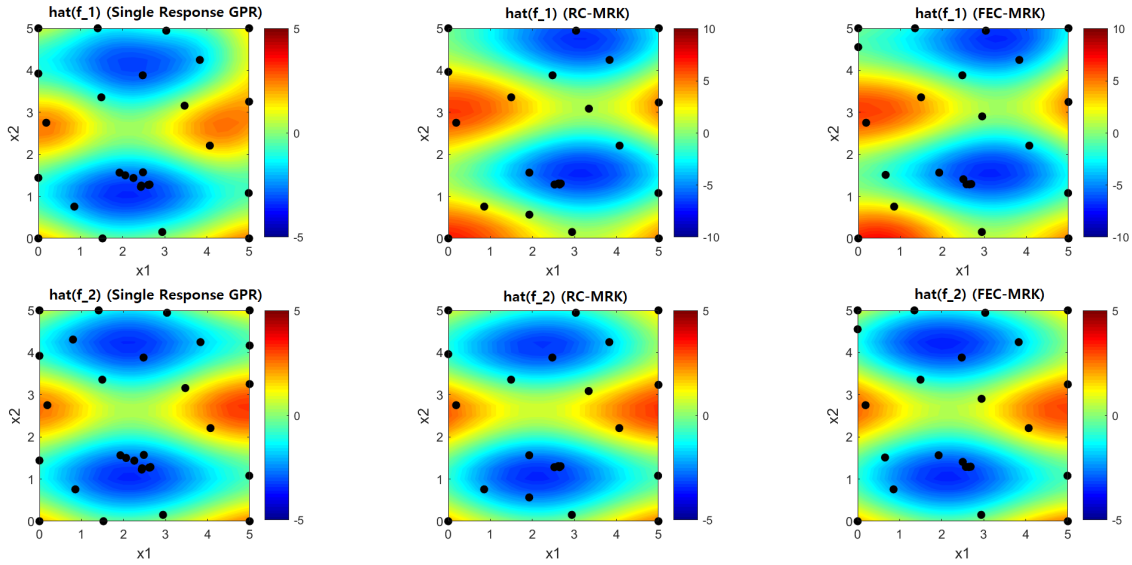

(a) Single response GRP
samples = 31
iteration = 10
RMSE of $f_1 = 0.4201$
RMSE of $f_2 = 0.1769$

(b) RC-MRK
samples = 23
iteration = 7
RMSE of $f_1 = 0.3108$
RMSE of $f_2 = 0.1648$

(c) FEC-MRK
samples = 24
iteration = 7
RMSE of $f_1 = 0.3778$
RMSE of $f_2 = 0.1111$

Figure 4.18: The comparison of f_1 and f_2 contour at the last iteration (Weakly coupled function)

where (k) is the iteration number. To consider the randomness of the initial sampling, the test has been performed 20 times, and the results are averaged.

Figure 4.18 shows the comparison of F contour at the last iteration for one test case. Figure 4.19 shows the result of the test for weakly coupled functions. Compared to the single response Kriging model, both multi-response Kriging model used less number of design iterations and samples for the convergence. Especially, the number of samples to find the optimum is decreased about 20%. Moreover, comparing the average RMSE at the last design iteration, both multi-response GPR models have lower RMSE even fewer number of samples are used. Therefore, the global accuracy of the surrogate model during the EGO process is promising.

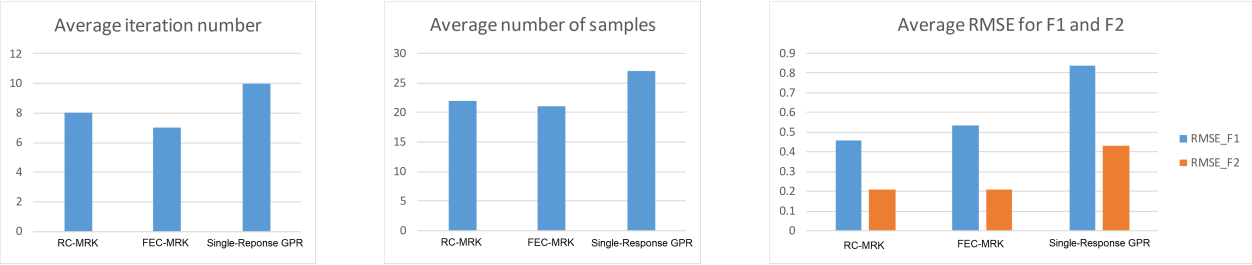

Figure 4.19: The result of EGO test for weakly coupled functions

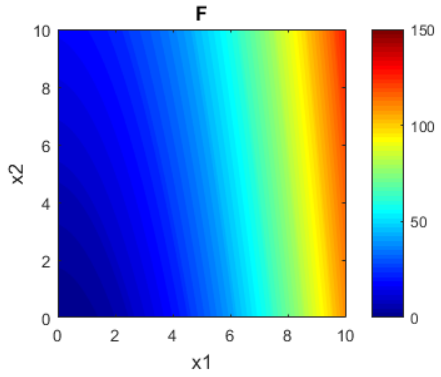

Figure 4.20: The contour of objective function for strongly coupled case($z_1 = 0$)

Strongly coupled function

The second test comes with strongly coupled function. The strongly coupled functions in the previous subsection is used as two different disciplines (Eq. (4.10)), but the high-level objective function F is added to consider the optimization problem. The problem is described as below. The exact sliced contour of function F at $z_1 = 0$ is shown in Figure 4.20. The objective function has one global minimum at (x_1, x_2, z_1) =(0,0,1.9776).

$$\begin{aligned} \underset{x_1,x_2,z_1}{\text{minimize}} \quad & F = x_1^2 + x_2 + f_1 + \exp\left[-f_2\right] \\ \text{subject to} \quad & 0 \leq x_1 \leq 10, \\ & 0 \leq x_2 \leq 10, \\ & -10 \leq z_1 \leq 10, \end{aligned} \tag{4.13}$$

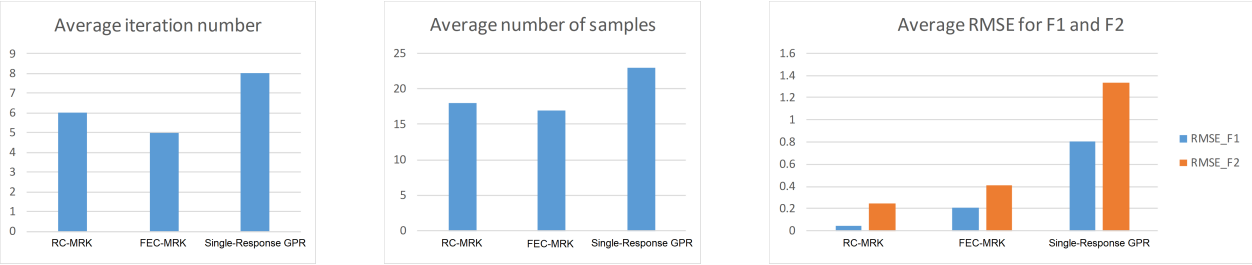

Figure 4.21: The result of EGO test for strongly coupled functions

For this optimization problem, the number of initial samples are set as 15, and randomly picked with LHS. For the comparison, DACE, RC-MRK and FEC-MRK are used as the surrogate model, and the results are compared. Same infill sampling strategy as done with weakly coupled case is used. The design iteration is terminated if the relative error of optimum function value is lower than 10^{-4}. To consider the randomness of the initial sampling, the test has been performed 20 times, and the results are averaged.

Figure 4.21 shows the result of EGO test for strongly coupled functions. Compared to the single response Kriging model, both multi-response Kriging model used less number of design iterations and samples for the convergence; the number of samples to find the optimum is decreased up to 25%. Moreover, the average RMSE at the last design iteration is dramatically lower with both multi-response Kriging models.

From the local accuracy test with EGO process, it is verified that for the multidisciplinary design problem, multi-response Kriging model can decrease the number of samples which is required for the design convergence. Moreover, since the global accuracy of the surrogate model is better due to the correlation information between the responses, the global optimum of the complex problems can be guaranteed as well.

Chapter 5

Design Applications

5.1 Aeroelastic Shape Optimization Airfoil

Multi-response Kriging model is a useful tool for most aerospace applications as the majority of the aerodynamic/structural/thermal etc. since the outputs are highly coupled. In this section, as an application of multi-response Kriging model, airfoil shape optimization of performed with aeroelasticity analysis. To focus on the performance of multi-response Kriging model, the optimization of performed with no infill sampling and single fidelity analysis. NACA0012 airfoil is set as a base airfoil, and the airfoil is designed to maximize the lift coefficient while minimizing the pitching angle associated with the lift. The objective function for the minimization problem is shown in Eq. 5.1.

$$OBJ = \left(\frac{C_l}{C_l'}\right)^{-1} + \frac{\theta}{\theta'} \tag{5.1}$$

where C_l is the lift coefficient of the airfoil, and θ is the wing twist. The variables with superscript denote the value from baseline airfoil, which is NACA0012.

To perturb the airfoil, the radial basis function (RBF) domain approach [90] is used. RBF domain element approach is a full domain deformation method which creates new airfoil shapes based on the deformation of an initial airfoil. The deformation is performed by preserving the exact movement of a set of control points, then creating a deformation field

defined by radial basis function interpolation. Eq.5.2 shows RBF equation.

$$f(\xi) = \exp\left(\frac{-\xi^2}{2\sigma^2}\right) \tag{5.2}$$

where ξ is the distance of mesh node to control point, and σ is the radius of influence. Since ξ is the distance between node on the airfoil and the control point, once the location of control point is calculated, it can be determined as well. The radius of influence σ is unknown variable. In this paper, two control points at the leading edge and trailing edge of the airfoil are used for the baseline. As the location of control points and the radius of influence changes, it creates a new deformation field, and a new airfoil geometry can be obtained. Therefore, in this paper, six design variables are used; x-directional translation and y-directional translation of control points, and the radius of influence for each control point. Figure 5.1 shows NACA0012 diagram with control point and design variables.

The aerodynamic condition of the problem is set as $Re = 10^6$ and $Mach = 0.2$. For the aerodynamic analysis, incompressible RANS equations were solved to determine the lift coefficient at zero angle of attack and the lift curve slope using QuickerSim [91]. Figure 5.2 shows aerodynamic analysis result of the baseline airfoil (NACA 0012).

For the elastic model, spring model is used for the prediction of the pitching angle [92]. Figure 5.3 shows the model description. For the lift L and aerodynamic moment M_0 on the airfoil, the aerodynamic pitching angle can be calculated as shown in Eq. 5.3.

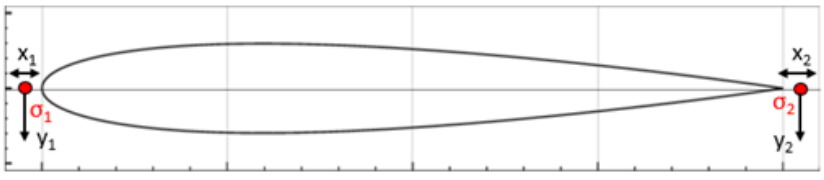

Figure 5.1: NACA 0012 diagram with design variables

$$
\begin{aligned}
M_0 + Le &= K\theta \\
M_0 &= \frac{1}{2}\rho V^2 c^2 C_{M,0} \\
L &= \frac{1}{2}\rho V^2 c C_L \\
C_L &= C_{L,0} + \frac{\partial C_L}{\partial \alpha}(\alpha + \theta)
\end{aligned}
\tag{5.3}
$$

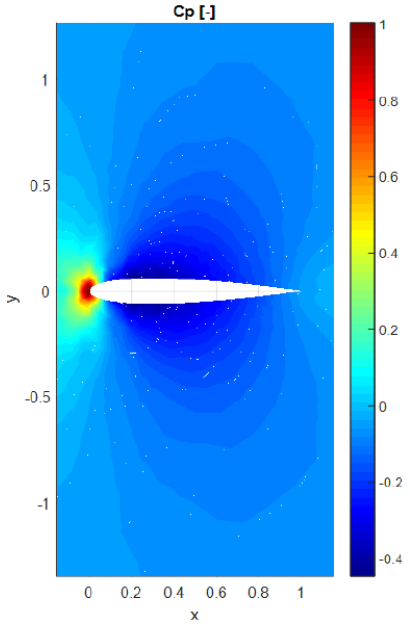

Figure 5.2: Aerodynamic analysis result of NACA0012 baseline airfoil

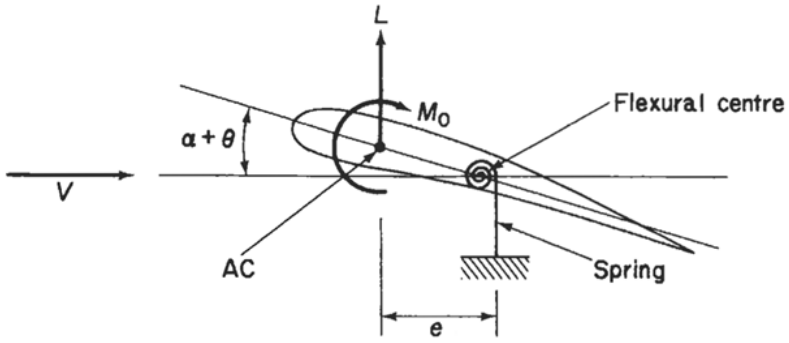

Figure 5.3: Aerodynamic force and aeroelastic torsion of the wing

where e is the distance between aerodynamic center and flexural center, K is spring constant and c is the chord length of airfoil. Solving the equation, aerodynamic torsion θ can be calculated.

Fig. 5.4 shows the schematic of airfoil optimization process. First of all, the samples are randomly generated using Latin Hypercube Sampling. In this study, 50 training samples are selected. These sample airfoils are analyzed with aerodynamic solver and aeroelasticity solver. From these two solvers, the lift coefficient and wing twist can be calculated, and FEC-MRK model is generated for two responses. Then, the optimization is performed using genetic algorithm [11, 93]. In the genetic algorithm, 50 generations with 100 population size is used.

Table 5.1 show the optimization result. For the comparison, the optimization which does not use multi-response GRP model but all the analysis for the optimization has runs using CFD and aeroelastic model has been performed, which can be the exact optimization solution. As shown in Table 5.1, the optimization using FEC-MRK shows similar results with the optimum from the full solver. The relative error in lift coefficient between MRK result and full-solver result is about 1.28%, and the error in pitching angle is about 2.40%. However, FEC-MRK based optimization takes approximately 33 minutes whereas the full solver

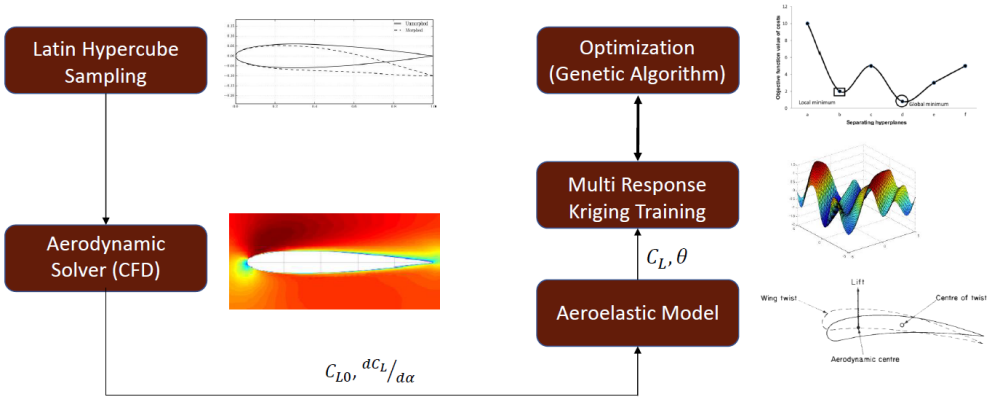

Figure 5.4: Schematic of airfoil optimization process

Table 5.1: NACA 0012 airfoil optimization results

	C_l	θ	Computational time
Opt. using Multi response GPR model	0.8439	0.0732 rad	1.9407×10^3
Opt. using aero. and aeroelastic solver	0.8548	0.0750 rad	1.1251×10^5

takes approximately 31 hours for the same. Therefore, about FEC-MRK based optimization used only 1.72% computational cost of full-solver optimization, and the cost reduction is remarkable.

5.2 Aerodynamic shape optimization of high-lift multi-element airfoil

As a practical design application of infill sampling method, high-lift multi-element airfoil is optimized in shape to maximize lift at a take-off condition. In this application, to focus on the performance of newly developed infill sampling criteria (ISC), single-disciplinary and single-disciplinary design is performed. In the general Efficient Global Optimization (EGO) process, multi-point multi-objective infill sampling criteria (MPMO-ISC) in Section 2.3.2 is implemented. For the comparison of sampling performance, the approximated q-EI, which is existing method, is implemented into EGO process as well.

5.2.1 Design problem

baseline airfoil is chosen as the NLR 7301 multi-element airfoil [94]. The objective of aerodynamic design is to maximize lift at drag force maintained as the baseline value at the take-off condition. The design variables are angle of attack, flap deflection angle, gap and overlap of flap. The design flow condition is at Mach number of 0.185, Reynolds number of 2.51

million and angle of attack of 13.1 degrees. The baseline NLR 7301 multi-element airfoil has a flap with 32% of the chord length, 2.6% of the gap and 5.3% of the overlap relative to the main airfoil. Baseline configuration of main airfoil and flap is shown in Figure 5.5 and 5.6.

The mathematical formulation of the design problems is shown in Eq. (5.4) as a single objective optimization problem. The constraint of C_d^* and C_l^* is included in the objective function, and consequently the design problem reduces to the unconstrained optimization problem requiring a single surrogate model. The optimization process is iterated until the error in the objective function values between previous and the current design steps to be less than 0.01%.

$$\begin{aligned} \underset{\alpha,\delta_\theta,\delta_x,\delta_y}{\text{minimize}} \quad & F = \left(1.0 - \frac{C_l^*}{C_l}\right)^2 + \left(1.0 - \frac{C_d^*}{C_d}\right)^2 \\ \text{subject to} \quad & C_l^* = 1.5 C_{l,baseline},\ C_d^* = C_{d,baseline} \end{aligned} \tag{5.4}$$

Instead of using conventional definitions of flap gap and overlap, the location of flap is defined with horizontal and vertical displacements to conveniently handle the geometry variation and CFD mesh generation. Mesh deformation for the CFD analysis is carried out automatically through the software journaling technique [95]. The flap geometry changes from baseline

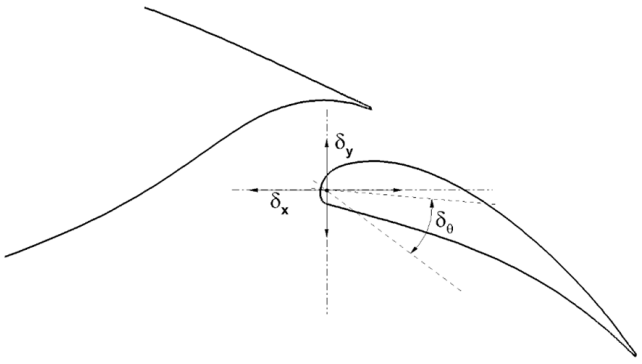

Figure 5.5: Configuration of design variables in NLR 7301 multi-element airfoil

Table 5.2: Design variable bound for NLR 7301 multi-element airfoil optimization

Design variable	Symbal	Baseline	Lower bound	Upper bound
Angle of attack	α	13.1°	7.0°	13.0°
Flap deflection angle	δ_θ	$-14.5°$	$-30.0°$	$-12.0°$
Horizontal displacement	δ_x	0.0%c	-5.0%c	10.0%c
Vertical displacement	δ_x	0.0%c	-2.0%c	2.0%c

configuration depicted in Figure 5.5 corresponding to the variation of the design variables with their upper and lower bounds listed in Table 5.2.

5.2.2 High-fidelity aerodynamic analysis

The function evaluations of a set of initial sample points and adaptive infill sample points are carried out through high-fidelity CFD analysis using parallel CPUs. The Reynolds-averaged Navier-Stokes (RANS) equations are solved by a SU2 flow solver [96] at a given design condition. The flow solver uses an unstructured grid topology and has a computational design suite with sensitivity analysis available based on continuous adjoint formulation. Automatic mesh deformation using a torsional spring analogy or free-form deformation (FFD) method for three-dimensional shape variation are available in the design framework along with the choice of various gradient-based optimization algorithms.

To validate the flow solver, flows around the baseline airfoil (NRL 7301 with flap) are solved at the design take-off condition and the results are compared with the experimental data. The O-type unstructured grid system with 64,201 elements and 32,531 nodes is generated using the T-REX technique of Pointwise software [95] and shown in Figure 5.6. For the spatial discretization, the 2nd order centered difference scheme with JST artificial dissipation [4] is used, and time is integrated using the second-order of Euler-implicit method [97]. Viscous flux is discretized using the centered difference method with a Spalart-Allmaras turbulence

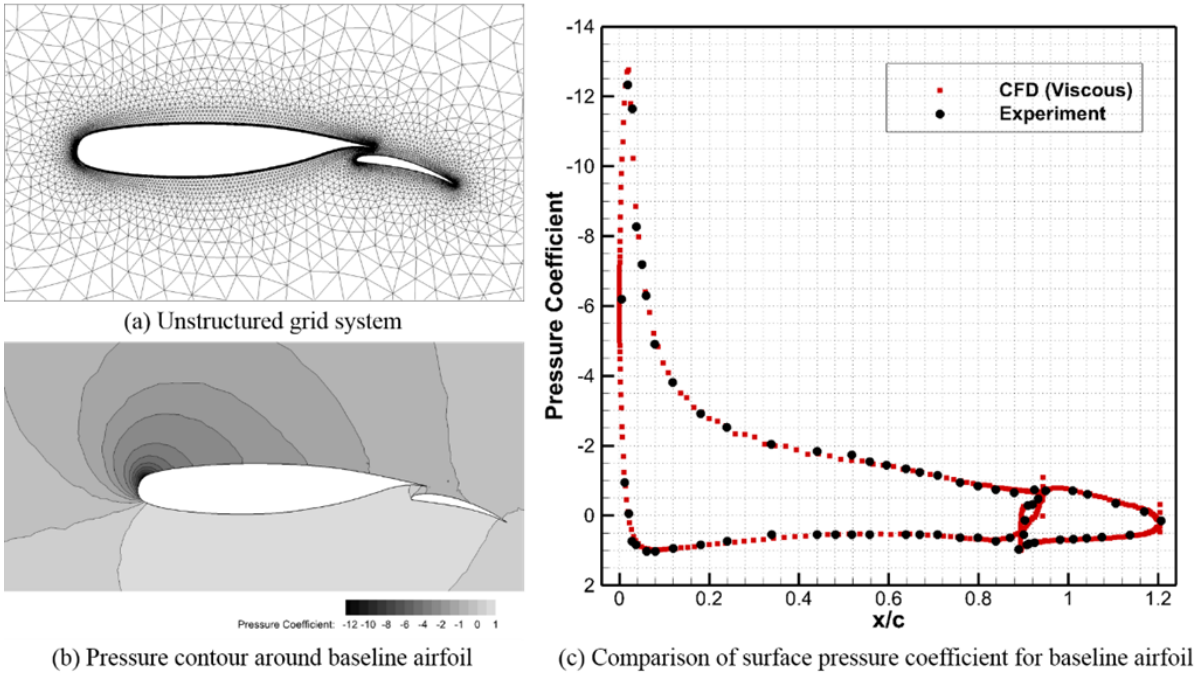

Figure 5.6: Validation of CFD analysis for baseline airfoil

model [98]. The two-level multigrid technique [99] is used to accelerate the convergence. Pressure coefficients on the airfoil surface and near-field pressure coefficients are plotted in Fig. 7(b) and (c), respectively, showing good agreement with experimental data.

5.2.3 Design results

Initially, a set of 15 initial sample points are generated by the LHS method for the current four dimensional design space. This number is notably small considering a general sampling rule based on $(p+1)(p+2)/2$ [17], which is attributed to the efficiency of the MPMO-ISC. Initial sample points are evaluated by the CFD analysis, and an initial Kriging model is constructed correspondingly. For additional infill sampling method, the MPMO-ISC with balancing approach and dynamic switching approach and the approximated q-EI with KB, CLmax, and CLmin are used. To save computational time considerably, alternative to

finding the optimal value through the GA with the Kriging model, the minimum objective value of existing sample points at each design iteration is regarded as the minimum point. It does not harm the original purpose of EGO framework, because the optimal point searched from optimization procedure and the minimum function value of sample points would be converged to the same value as a result of exploitation performance of ISC refining around the minimum. The number of additional sample points is set three.

Starting from 15 initial sample points, more sample points are added at each design iteration by the MPMO-ISC method with the balancing approach, the MPMO-ISC method with the dynamic switching approach, and the q-EI method with CLmin. An optimum function value at each design iteration is plotted in Fig. 8 with respect to the number of sample points. The MPMO-ISC method with the balancing approach is the most efficient, finding the minimum with 186 sample points after 57 design iterations. The second most efficient ISC is the MPMO-ISC method with the dynamic switching approach and finds the minimum point with 243 sample points after 76 iterations. The optimum found by the q-EI method with the CLmax has a larger objective value than that of the MPMO-ISC method, even with more than the twice the number of sample points.

Improvements in the lift force are summarized in Table 5.3 with respect to the EGO frameworks with different ISC methods as well as to the gradient-based optimization. The lift coefficient is increased by about 18.5%, while the drag coefficient is slightly increased by about 6.5% by EGO methods with the MPMO-ISC and q-EI methods.

Optimal values of the design variables are listed in Table 5.4. The angle of attack is reduced to about 10.25 degree from 13.1 degree of the baseline airfoil. The flap angle is reduced so that the total chord length is increased and flows over the main airfoil move smoothly over the flap, which can be seen in Figure 5.8(Left : baseline, Right : Optimized airfoil) and Figure 5.9(Black line : baseline, Red line : Optimized airfoil). The increase of the lift force

Table 5.3: Aerodynamic performance of the minimum point

Design method	**Objective value**	C_l **(Inc., %)**	C_d **(Inc., %) (Inc.,Δ counts)**	**# of Design iterations**	**# of CFD Sim.**
Baseline	0.25	3.2089	0.06079		
MPMO-ISC (balancing)	0.07332	3.80822 (18.68%)	0.064703 (6.438%) (3.914 counts)	57	186
MPMO-ISC (D. switching)	0.07601	3.79125 (18.15%)	0.064512 (6.124%) (3.723 counts)	76	243
Approximated q-EI KB	0.07480	3.80177 (18.48%)	0.064892 (6.749%) (4.103 counts)	134	417
Approximated q-EI CLmax	0.07480	3.80177 (18.48%)	0.064892 (6.749%) (4.103 counts)	134	417
Approximated q-EI CLmin	0.07371	3.80618 (18.61%)	0.06472 (6.466%) (3.931 counts)	122	381

Table 5.4: Design variable of the minimum point

Design method	α	δ_θ	δ_x	δ_y
Baseline	13.1°	-14.5°	0.0%c	0.0%c
MPMO-ISC (balancing)	10.26°	-29.66°	6.44%c	1.06%c
MPMO-ISC (D. switching)	10.24°	-29.84°	6.42%c	1.05%c
Approximated q-EI KB	10.25°	-30.00°	6.47%c	1.08%c
Approximated q-EI CLmax	10.24°	-29.92°	6.45%c	1.05%c
Approximated q-EI CLmin	10.26°	-29.99°	6.41%c	1.06%c

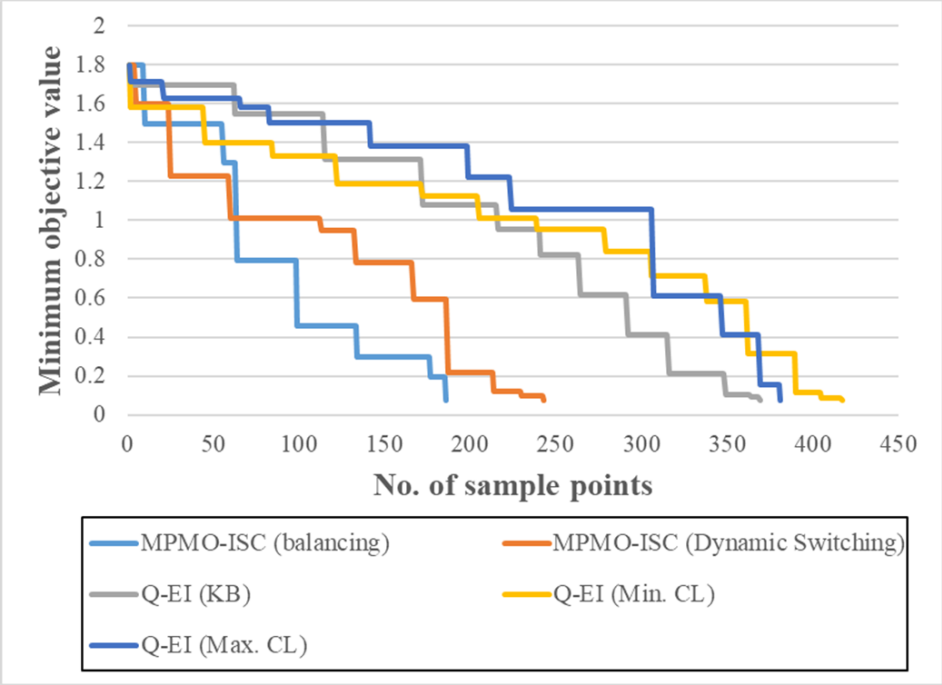

Figure 5.7: Comparison of objective value variations w.r.t the number of sample points

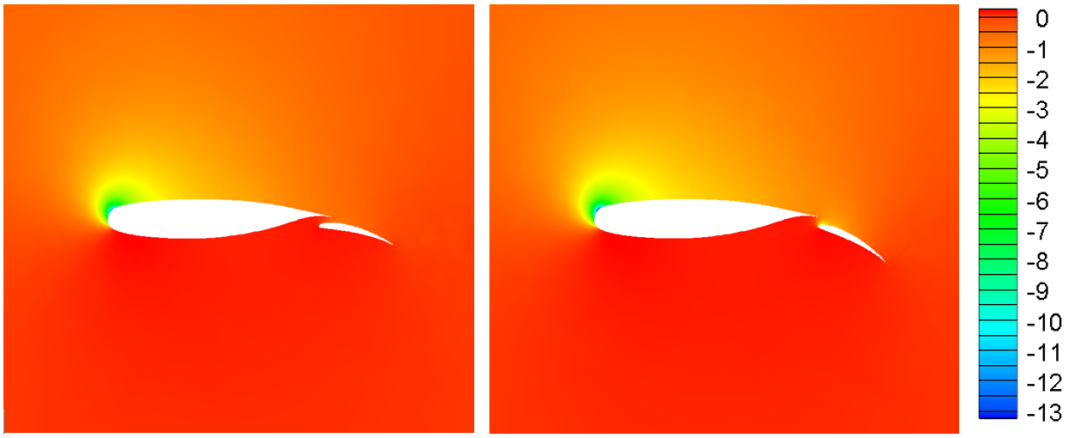

Figure 5.8: Comparison of baseline and design results in pressure coefficient contour

is also observed in the plot of surface pressure coefficient in Figure 5.8.

Figure 5.9: Comparison of baseline and design results in geometry

5.3 Aerodynamic shape optimization of control surface of tailless aircraft

In this section, the shape optimization of the control surface of tailless aircraft is carried out as a three-dimensional design problem to minimize the geometric area to reduce power consumption for controlling hinge-moment of the surface while satisfying the constraint on the roll performance. For the optimization, variable fidelity Efficient Global Optimization framework (Figure 2.5) in Section 2.5 is applied, which includes variable-fidelity analysis technique in Section 2.2, dynamic sampling in Section 2.3 and dynamic fidelity indicator in Section 2.4. The result is compared with Efficient Global Optimization only with high fidelity analysis method.

As the geometry of tailless aircraft, a configuration of Lockheed Martin tactical aircraft systems-innovative control effector (LMTAS-ICE) is selected, for which the variable-fidelity aerodynamic analysis was carried out in author's previous work [21] to validate the wind-tunnel experimental data. The design using the high fidelity analyses only is carried out independently for the direct comparison with the variable fidelity design.

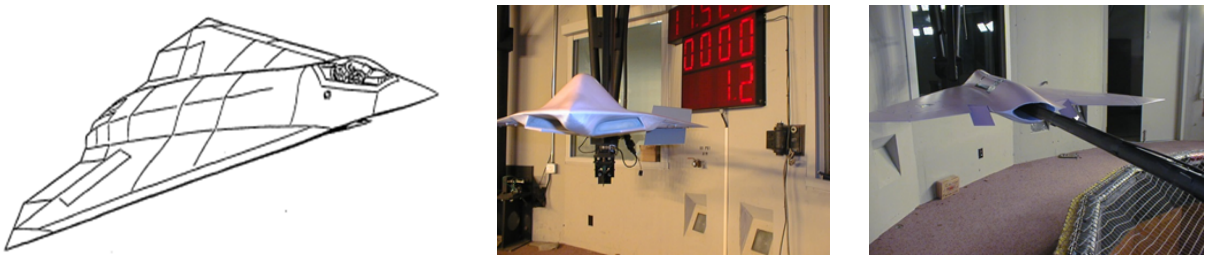

Figure 5.10: ICE 101 configuration and the models for wind tunnel test

5.3.1 Innovative control effectors

As the tailless aircraft does not have horizontal and vertical tails, it has great advantages in aerodynamic performance with low drag and reduced weight. However, this geometric characteristic also leads to poor performance in stability and control, especially in the lateral stability, as the moment becomes sensitive to the location of the center of gravity without the tails.

To overcome the disadvantages, several studies have been performed including a Lockheed Martin Tactical Aircraft Systems-Innovative Control Effector (LMTAS-ICE, ICE, Fig.5.10) [34, 35, 100] to improve the stability characteristics of the wing-body tailless combat aircraft. Many computational fluid dynamics (CFD) calculations [101, 102, 103] and wind tunnel tests [34, 35, 100] were carried out for stability analysis.

Based on the wind tunnel experiments performed at the Air Force Research Laboratory (AFRL) facilities [34, 35, 100], three types of control surfaces of all-moving-wingtip (AMT), differential-leading-edge-flap(DLEF), and spoiler-slot-deflector(SSD) are concluded to be appreciably effective among several types of control effectors shown in Fig.5.11 [35]. However, according to the report, being an all-round control effector, AMT is the most effective control surface for the ICE configuration.

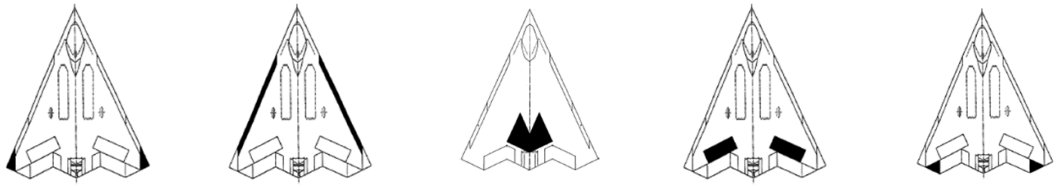

(a) AMT (b) DLEF (c) DRUD (d) SSD (e) Clamshell

Figure 5.11: Control surfaces of ICE 101 configuration

5.3.2 Design problem

The all-moving-wingtip (AMT) surface is designed for a minimum surface area to satisfy mission requirements, enforced by the Department of Defense [104]. The current ICE-101 configuration belongs to the 'Class IV' high maneuverability aircraft such as fighter, attacker, and tactical reconnaissance. The design condition is close to 'Category C' which requires gradual maneuvers and requires accurate flight path control during takeoff, approach, landing and etc. Regarding the flying qualities, 'Level 1' of 'satisfactory' requires that the flying quality should be adequate for the mission flight phase. Desired performance should be achievable with no more than minimal pilot compensation.

The objective is to minimize the geometric area of the AMT surface which is defined by the four design variables, shown in Fig. 5.12, of the AMT length (A), angle (B), rotation axis ratio (C), and the deflection angle (δ_{AMT}). Bounds on each design variable are imposed as

$$\begin{aligned} 6.0ft \leq A \leq 8.5ft \\ -10^\circ \leq B \leq 25^\circ \\ 0.2 \leq C \leq 0.8 \\ 5.0^\circ \leq \delta_{AMT} \leq 30^\circ. \end{aligned} \tag{5.5}$$

The rolling performance of the ICE-101 configuration is evaluated by the time-to-bank angle

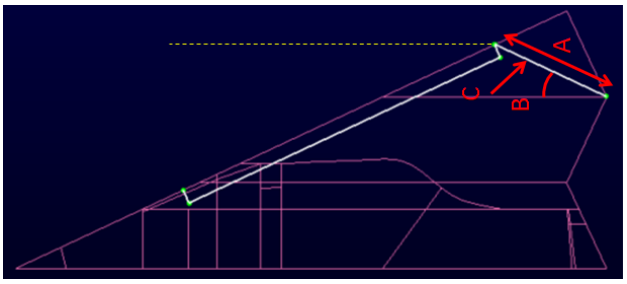

Figure 5.12: Design variables of AMT

specified by the DoD military handbook [104] which states that the time-to-bank angle for aircraft of Class I with the flight conditions of Category C should be less than 1.1 seconds to satisfy the 'Level 1' requirement. The detailed derivation of the time-to-bank is explained in Ref. [105]. The flight condition is at the trim condition with the Mach number of 0.3 at the angle of attack of 3.76°.

5.3.3 Variable-fidelity aerodynamic analysis

Vortex panel, Euler, and RANS flow solvers are used for low-, medium-, and high-fidelity analyses, respectively. An open source of the VortexJE code [106] is employed, which is based on a low-order panel method with source and doublet elements.

As the highest-fidelity analysis, the three-dimensional Reynolds-Averaged Navier-Stokes (or the Euler) equations are solved. The CFD flow solver of SU2 (Stanford University Unstructured) [107, 108] is used which is C++ programming software in parallel computation environment. It is based on the finite volume method (FVM) with a grid partitioning algorithm for parallel computation.

Figure 5.13 shows the computational grids for the panel and the CFD computation. An unstructured mesh is used with T-rex approach to generate boundary-layer cells. The grid with 4.64∼5.10 million volume cells is used for the Euler computation. For the RANS computa-

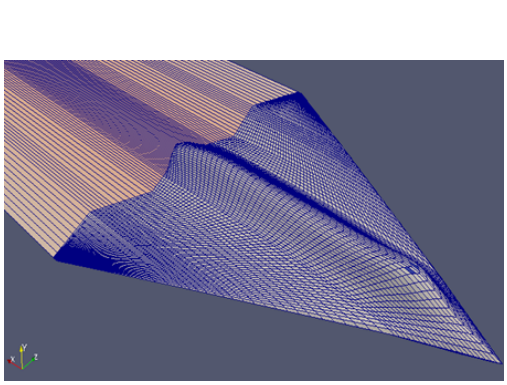

(a) Surface mesh for VortexJE

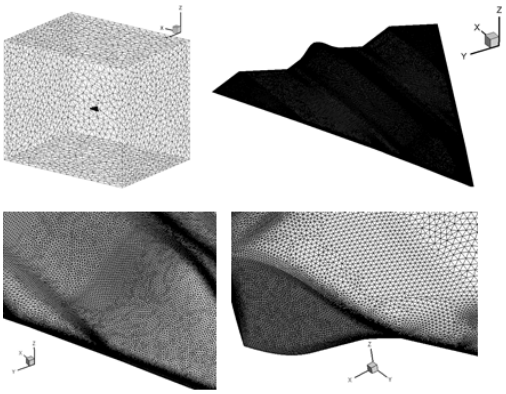

(b) Surface mesh for SU2 (Euler computation)

Figure 5.13: Surface mesh for computational methods

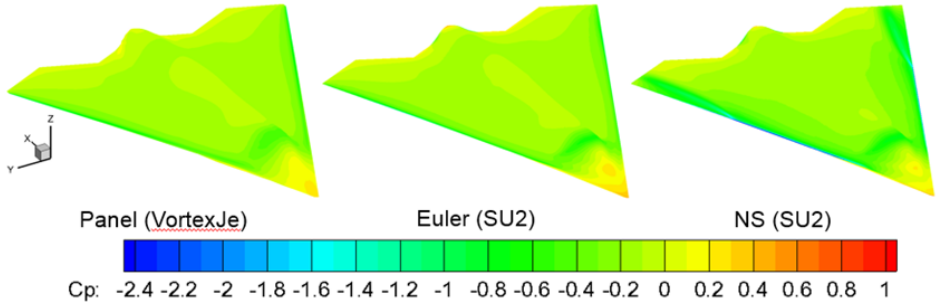

Figure 5.14: Pressure coefficient contour comparison between each method (M=0.3, α=3.76 °)

tion, the grid with 14.50∼14.65 million volume cells is made. Roe's second order accurate spatial discretization [5] and the Venkatakrishnan limiter [109] is used. An Euler implicit method with an LU-SGS scheme [110] is applied for time integration with better numerical stability, and the multi-grid technique is used to accelerate the solution convergence. The Euler CFD calculation takes about one hour, and RANS computation takes about 6 hours using a total of 63 cores. For all computation, a CPU with AMD Opteron processor 6376 with 3.30 GHz is used. Resultant surface pressures are plotted in Figure 5.14 and 5.15 [102, 103] with the convergence criterion of 10^{-7}.

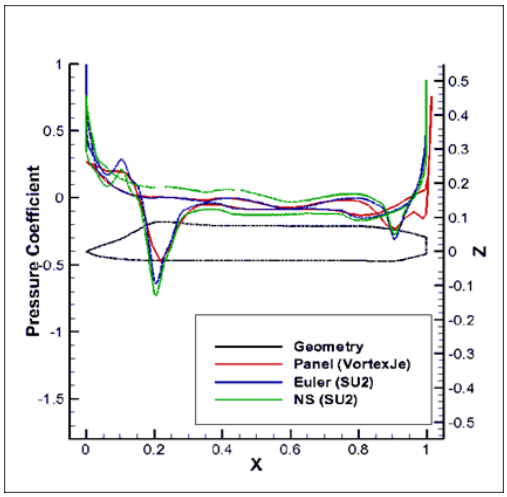

(a) $y = 0\%$ of half span from the center line

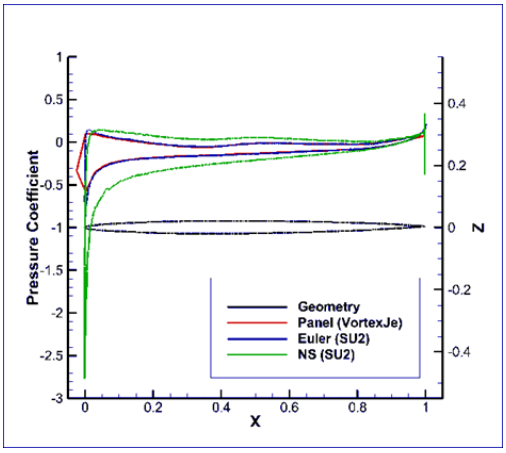

(b) $y = 50\%$ of half span from the center line

Figure 5.15: The comparison of pressure coefficient along the cross section between each method (M=0.3, α=3.76 °)

5.3.4 Design results

The initial samples of 18, 9, and 6 points are selected for the panel, Euler, and RANS computations, respectively. The design termination criterion is the accuracy of the Kriging prediction at the optimal point with an error less than 5% by the RANS validation. Again, the high fidelity design using the RANS solutions only is carried out independently. The computational cost factor (CCF) of both designs are defined as

$$\begin{aligned} CCF_{VF} &= 6.0 \times n_H + 1.0 \times n_M + 0.00046 \times n_L \\ CCF_{HF} &= 6.0 \times n_H \end{aligned} \tag{5.6}$$

where n_H, n_M, and n_L are the number of RANS, Euler, and panel analyses, respectively.

Design histories of the variable fidelity and the high fidelity design are shown in Fig. 5.16.

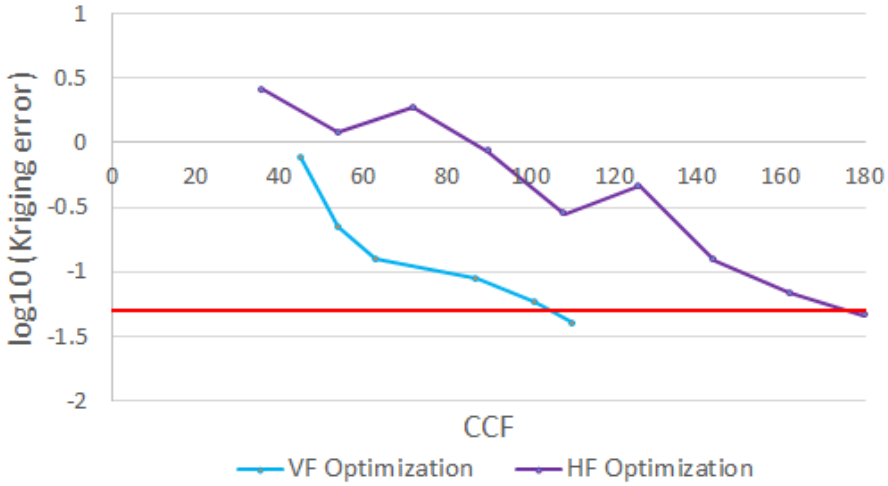

Figure 5.16: Design history for the optimum AMT shape between VF optimization and HF optimization

Red line on the graph shows termination criterion. As the result, the convergence rate is faster by 30 $\sim$ 40% with the variable fidelity design than that of the high fidelity design. During the optimization, a total of 11 and 9 infill sample points are added for Euler and RANS analyses for the variable fidelity design, while 24 RANS analyses are additionally needed for the high fidelity design.

Table 5.5 and Fig. 5.17 summarize design results and compares computation efficiency and optimum values between the variable fidelity and high fidelity designs. All design results are similar for the area of the AMT surface which is reduced by about 75% compared to that of the baseline. Values of optimal design variables are close to the bounds, indicating further reduction of area may have been possible.

Table 5.5: Comparison of Design result for AMT shape

Quantity	Baseline	VF Optimization	HF Optimization
CCF		110.09	180
A (ft)	8.5	6.00	6.01
B (degree)	25	-9.40	-9.36
C	0.5	0.6482	0.6591
δ_{AMT} (degree)	10	28.996	29.511
T_B (s)	1.51	1.0981	1.0912
S (ft^2)	17.79	4.5023	4.4813

(a) Baseline AMT (b) Optimized AMT

Figure 5.17: The comparison of AMT shape

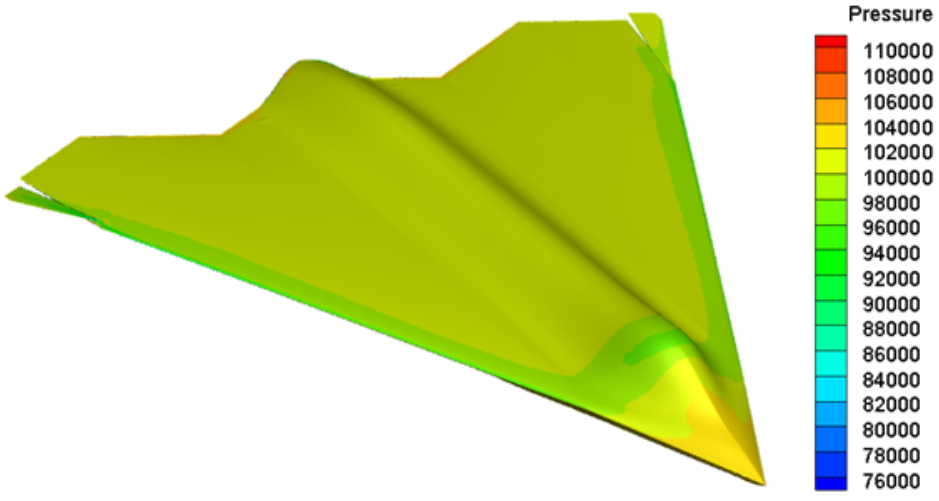

Figure 5.18: Pressure contour of the optimum AMT design result by variable fidelity optimization

Chapter 6

Conclusion

In this paper, four key design methodologies were developed to improve Efficient Global Optimization(EGO) design framework for multidisciplinary design problem with variable-fidelity data analysis : 1) Variable-fidelity analysis based on error approximation and calibration of low-fidelity analysis, 2) Dynamic sampling criteria which includes both filtering and infilling samples, 3) Dynamic fidelity indicator (DFI) for infill samples in variable-fidelity analysis, and 4) Multi-response Kriging model with iterative method of searching Maximum Likelihood (iMLE).

For the use of variable fidelity analyses for the sample evaluation in the EGO process, the variable-fidelity analysis method based on error approximation and calibration is developed. Using the method, lower fidelity samples are updated as accurate as high fidelity samples. Using all the data set together, variable fidelity Kriging model can be constructed and implemented into EGO process. The method is validated with two analytic test functions of a six-hump camel-back and a simplified Rastrigin function. The results confirmed that the developed variable fidelity design method is as accurate as the high fidelity design at less computational cost ($20\% \sim 50\%$ reduced cost).

For the dynamic sampling in the EGO process, filtering criteria and infilling criteria is developed. Filtering criteria is for the filtering process of improperly calibrated lower fidelity samples during the variable-fidelity analysis. Infilling criteria is for adding the additional samples in each design iteration for the training of surrogate model. For the infilling sam-

ples, multi-point and multi-objective infill sampling criteria (MPMO- ISC) is developed and implemented in the EGO design framework to maximize the cost efficiency. MPMO-ISC is proposed in the consideration of where additional sampling should be placed, either on the less explored area – exploration, or near the optimum point– exploitation. The trade-off between exploration and exploitation is resolved with the multi-objective optimization. Two approaches of the balancing and dynamic switching are developed to choose infill sample points with flexibility and adaptivity along the Pareto-front set of the MPMO-ISC method. Both approaches are observed to be more efficient than the approximated q-EI methods from the results of validation of two analytic functions : six-hump camel-back function and Matlab peak function.

Moreover, for the use of infill sampling in variable fidelity design, dynamic fidelity indicator(DFI) based on overlapping coefficient is developed. Throughout developed DFI, engineers can choose the fidelity of the additional sample in the next design iteration, and it can lead to a cost reduction of the entire design process since we can replace unnecessary high fidelity samples with the lower fidelity samples.

To extend Efficient Global Optimization process from single-disciplinary problem to multidisciplinary design problem, multi-response Kriging model is developed. Two different approaches of multi-response Kriging model, RC-MRK and FEC-MRK, are introduced, and the methods are advanced using iterative Maximum Likelihood Estimation (iMLE) process. Since the model can consider the correlation between responses, which are physically related in nature, the accuracy of function estimation is improved. Moreover, through the developed Maximum Likelihood Estimation process, a large number of hyper-parameters in Kriging model are observed accurately even with huge covariance matrix with numerical instability, which leads improvement in the accuracy of the prediction. The advanced methods are validated with analytic test function, and it is shown that the suggested meta-model is

improved up to 25% cost efficient and accurate in global accuracy.

As the practical design problem, aeroelasticity design problem with NACA0012 airfoil is carried out with multi-response Kriging model. NRL 7301 multi-element airfoil is optimized using the EGO framework with MPMO-ISC, and the shape of the control surface of the tailless aircraft is optimized for minimum geometric area to improve controllability and stability with variable-fidelity EGO framework.

In the future, multi-response Kriging model will be extended to the use of variable fidelity data analysis as mentioned in Section 3.2. Multi-response Kriging model provides us the information of covariance between predicted function value of different responses. If we construct multi-response Kriging model between different fidelity data, we can obtain the correlation between the responses, which is the correlation between different fidelity sample sets. This information can be used for the variable-fidelity data analysis. In current study, single response Kriging model is used for the variable-fidelity data analysis. Since it is proved that the global accuracy of multi-response Kriging model is much better than the one of single-response Kriging, a huge improvement in variable-fidelity data analysis is expected.

Bibliography

[1] N. R. Augustine. *Augustine's Laws*. American Institute of Aeronautics and Astronautics, Reston, Va, 6 edition, 1997.

[2] *Defense Systems Management College*, Dec. 1991.

[3] P. Raj. Aircraft design in the 21st century - implications for design methods. In *29th AIAA, Fluid Dynamics Conference*, Albuquerque,NM, Jun 1998. AIAA.

[4] Antony Jameson, Wolfgang Schmidt, and Eli Turkel. Numerical solution of the euler equations by finite volume methods using runge kutta time stepping schemes. In *14th fluid and plasma dynamics conference*, page 1259, 1981.

[5] Philip L Roe. Approximate riemann solvers, parameter vectors, and difference schemes. *Journal of computational physics*, 43(2):357–372, 1981.

[6] Elijah Polak. *Optimization: algorithms and consistent approximations*, volume 124. Springer Science & Business Media, 2012.

[7] Ronald M Errico. What is an adjoint model? *Bulletin of the American Meteorological Society*, 78(11):2577–2592, 1997.

[8] Rachit Prasad, Hyun Soon Kim, Dongkyun Im, Seongim Choi, and Seulgi Yi. Analysis and sensitivity calculation using high fidelity spectral formulation-based fsi and coupled adjoint method. In *AIAA AVIATION Forum, 17th AIAA/ISSMO Multidisciplinary Analysis and Optimization Conference*, Washington, DC, Jun 2016. AIAA.

[9] Rachit Prasad, Hyunsoon Kim, and Seongim Choi. *Flutter Related Design Optimization using the Time Spectral and Coupled Adjoint Method*. American Institute of Aeronautics and Astronautics, Kissimmee, FL, Jan 2018.

[10] Lawrence Davis. Handbook of genetic algorithms. 1991.

[11] David E Goldberg. *Genetic algorithms*. Pearson Education India, 2006.

[12] John A Nelder and Roger Mead. A simplex method for function minimization. *The computer journal*, 7(4):308–313, 1965.

[13] Andre I Khuri and John A Cornell. *Response surfaces: designs and analyses*. Routledge, 2018.

[14] Noel Cressie. Statistics for spatial data. *Terra Nova*, 4(5), 1992.

[15] Jacek M Zurada. *Introduction to artificial neural systems*, volume 8. West publishing company St. Paul, 1992.

[16] Donald R. Jones, Matthias Schonlau, and William J. Welch. Efficient global optimization of expensive black-box functions. *Journal of Global Optimization*, 13(4):455–492, 1998.

[17] T. W. Simpson, J. D. Poplinski, P. N. Koch, and J. K. Allen. Metamodels for computer-based engineering design: Survey and recommendations. *Engineering with Computers*, 17(2):129–150, 2001.

[18] Jerome Sacks, Susannah B. Schiller, and William J. Welch. Designs for computer experiments. 31(1):41–47, 1989.

[19] Boxin Tang. Orthogonal array-based latin hypercubes. 88(424):1392–1397, 1993.

[20] Arnold M Kuethe, Chuen-Yen Chow, and YC Fung. *Foundations of Aerodynamics, Bases of Aerodynamics Design*. American Society of Mechanical Engineers, 1987.

[21] Jangho Park, Jae-Young Choi, Yeongmin Jo, and Seongim Choi. Stability and control of tailless aircraft using variable-fidelity aerodynamic analysis. *Journal of Aircraft*, 54(6):2148–2164, May 2017.

[22] Sohaib Obeid, Ratneshwar Jha, and Goodarz Ahmadi. Rans simulations of aerodynamic performance of naca 0015 flapped airfoil. *Fluids*, 2(1):2, 2017.

[23] D. You and P. Moin. Active control of flow separation over an airfoil using synthetic jets. *Journal of Fluids and Structures*, 24(8):1349–1357, 2008.

[24] Christopher C Rethmel. *Airfoil leading edge flow separation control using nanosecond pulse DBD plasma actuators*. PhD thesis, The Ohio State University, 2011.

[25] C.E. Rasmussen and C.K.I. Williams. *Gaussian Processes for Machine Learning*. Adaptative computation and machine learning series. University Press Group Limited, 2006.

[26] Economind. Is economic modelling a futile attempt before the everlasting uncertainty?, 2017.

[27] Bo Wang and Tao Chen. Gaussian process regression with multiple response variables. *Chemometrics and Intelligent Laboratory Systems*, 142:159 – 165, 2015.

[28] Jack P.C. Kleijnen and Ehsan Mehdad. Multivariate versus univariate kriging metamodels for multi-response simulation models. *European Journal of Operational Research*, 236(2):573 – 582, 2014.

[29] M. C. Kennedy and A. O'Hagan. Predicting the output from a complex computer code when fast approximations are available. 87(1):1–13, 2000.

[30] Zhonghua Han, Ralf Zimmerman, and Stefan GÃ¶rtz. Alternative cokriging method for variable-fidelity surrogate modeling. *AIAA Journal*, 50(5):1205–1210, May 2012.

[31] Zhong-Hua Han, Ralf Zimmermann, and Stefan Goretz. A new cokriging method for variable-fidelity surrogate modeling of aerodynamic data. In *48th AIAA Aerospace Sciences Meeting Including the New Horizons Forum and Aerospace Exposition, Aerospace Sciences Meetings*. AIAA, Jan 2010.

[32] Zhong-Hua Han, Stefan Görtz, and Ralf Zimmermann. Improving variable-fidelity surrogate modeling via gradient-enhanced kriging and a generalized hybrid bridge function. *Aerospace Science and Technology*, 25(1):177 – 189, 2013.

[33] Youngmin Jo, Seongim Choi, and Duckjoo Lee. Variable-fidelity design method using gradient-enhanced kriging surrogate model with regression. In *14th AIAA Aviation Technology, Integration, and Operations Conference, AIAA AVIATION Forum*. AIAA, Jun 2014. 0.

[34] Kenneth M. Dorsett and David R. Mehl. Innovative control effectors (ice). Technical Report WL-TR-96-3043, Jan 1996.

[35] Rears S. P. Dorsett, K. M. and H. P. Houlden. Innovative control effectors (ice) phase ii. Technical Report WL-TR-97-3059, Jan 1996.

[36] Youngmin Jo, Jangho Park, Christopher L. Ocheltree, Jae Young Choi, Seongim Choi, Pradeep Raj, and Duckjoo Lee. *Adaptive Variable-Fidelity Aerodynamic Analysis and Design for Tailless Aircraft under Model-Form Uncertainty*. American Institute of Aeronautics and Astronautics, Dallas, TX, Jun 2015.

[37] Felipe A. C. Viana, Timothy W. Simpson, Vladimir Balabanov, and Vasilli Toropov. Special section on multidisciplinary design optimization: Metamodeling in multidisci-

plinary design optimization: How far have we really come? *AIAA Journal*, 52(4):670–690, Jan 2014.

[38] Mohamed H. Bakr, John W. Bandler, Kaj Madsen, and Jacob SÃ?ndergaard. An introduction to the space mapping technique. *Optimization and Engineering*, 2(4):369–384, 2001.

[39] T. D. Robinson, M. S. Eldred, K. E. Willcox, and R. Haimes. Surrogate-based optimization using multifidelity models with variable parameterization and corrected space mapping. *AIAA Journal*, 46(11):2814–2822, Nov 2008.

[40] Leifur Leifsson, Slawomir Koziel, and Yonatan A. Tesfahunegn. Multiobjective aerodynamic optimization by variable-fidelity models and response surface surrogates. *AIAA Journal*, 54(2):531–541, Nov 2015.

[41] RAPHAEL T. HAFTKA. Combining global and local approximations. *AIAA Journal*, 29(9):1523–1525, Sep 1991.

[42] Seongim Choi, Juan J. Alonso, and Ilan M. Kroo. Two-level multifidelity design optimization studies for supersonic jets. *Journal of Aircraft*, 46(3):776–790, May 2009.

[43] Shawn E. Gano, John E. Renaud, and Brian Sanders. Hybrid variable fidelity optimization by using a kriging-based scaling function. *AIAA Journal*, 43(11):2422–2433, Nov 2005.

[44] Matthias Schonlau. *Computer Experiments and Global Optimization*. PhD thesis, University of Waterloo, Waterloo, Ont., Canada, Canada, 1997. AAINQ22234.

[45] Michael J. Sasena, Panos Papalambros, and Pierre Goovaerts. Exploration of metamodeling sampling criteria for constrained global optimization. *Engineering Optimization*, 34(3):263–278, Jan 2002.

[46] Dennis D Cox and Susan John. A statistical method for global optimization. In *IEEE International Conference on Systems, Man, and Cybernetics*, pages 1241–1246. IEEE, 1992.

[47] Harold J Kushner. A new method of locating the maximum point of an arbitrary multipeak curve in the presence of noise. *Journal of Basic Engineering*, 86(1):97–106, 1964.

[48] Felipe Viana, Raphael Haftka, and Layne Watson. Why not run the efficient global optimization algorithm with multiple surrogates? In *51st AIAA/ASME/ASCE/AHS/ASC Structures, Structural Dynamics, and Materials Conference*, Orlando, Florida, Apr 2010. American Institute of Aeronautics and Astronautics.

[49] David Ginsbourger, Rodolphe Le Riche, and Laurent Carraro. *Computational Intelligence in Expensive Optimization Problems*, chapter Chapter 6: Kriging Is Well-Suited to Parallelize Optimization, pages 131–162. Springer-Verlag, New York, 2010.

[50] Raphael T. Haftka, Diane Villanueva, and Anirban Chaudhuri. Parallel surrogate-assisted global optimization with expensive functions âeur" a survey. *Structural and Multidisciplinary Optimization*, 54(1):3–13, 2016.

[51] Zhiwei Feng, Qingbin Zhang, Qingfu Zhang, Qiangang Tang, Tao Yang, and Yang Ma. A multiobjective optimization based framework to balance the global exploration and local exploitation in expensive optimization. *Journal of Global Optimization*, 61(4):677–694, 2015.

[52] Seulgi YI, Hyung-Il. Kwon, and Seongim Choi. Efficient global optimization using a multi-point and multi-objective infill sampling criteria. In *52nd Aerospace Sciences Meeting, AIAA SciTech Forum*. AIAA, Jan 2014.

[53] Yeongmin Jo, Seulgi Yi, Seongim Choi, Duck-Joo Lee, and Dong-Zin Choi. Adaptive variable-fidelity analysis and design using dynamic fidelity indicators. *AIAA Journal*, 54(11):3564–3579, Aug 2016.

[54] Michael Schäfer Hans-Joachim Bungartz. *Fluid-structure Interaction: Modelling, Simulation, Optimization*. Springer-Verlag Berlin Heidelberg, 1 edition, 2006.

[55] Timothy W. Simpson, Timothy M. Mauery, John J. Korte, and Farrokh Mistree. Kriging models for global approximation in simulation-based multidisciplinary design optimization. *AIAA Journal*, 39(12):2233–2241, Dec 2001.

[56] Kevin G. Bowcutt. Multidisciplinary optimization of airbreathing hypersonic vehicles. *Journal of Propulsion and Power*, 17(6):1184–1190, Nov 2001.

[57] Donald E. Myers. Matrix formulation of co-kriging. *Journal of the International Association for Mathematical Geology*, 14(3):249–257, 1982.

[58] H.-S. Chung and J. Alonso. Using gradients to construct cokriging approximation models for high-dimensional design optimization problems. In *40th AIAA Aerospace Sciences Meeting & Exhibit*, Reno,NV, Jan 2002. AIAA.

[59] Alexander I. J. Forrester, Andras Sobester, and Andy J. Keane. *Engineering Design via Surrogate Modelling - A Practical Guide.* Wiley, 2008.

[60] Wataru Yamazaki, Markus Rumpfkeil, and Dimitri Mavriplis. Design optimization utilizing gradient/hessian enhanced surrogate model. In *28th AIAA Applied Aerodynamics Conference, Fluid Dynamics and Co-located Conferences*, Chicago, IL, Jun 2010. AIAA.

[61] J. Laurenceau and P. Sagaut. Building efficient response surfaces of aerodynamic functions with kriging and cokriging. *AIAA Journal*, 46(2):498–507, Feb 2008.

[62] Radford M. Neal. *Bayesian Learning for Neural Networks*. Springer-Verlag, Berlin, Heidelberg, 1996.

[63] S. Wang and S. H. Ng. A joint gaussian process metamodel to improve quantile predictions. In *2017 Winter Simulation Conference (WSC)*, pages 1891–1902, 2017.

[64] Stefano Conti and Anthony OâEUR(tm)Hagan. Bayesian emulation of complex multi-output and dynamic computer models. *Journal of Statistical Planning and Inference*, 140(3):640–651, 2010.

[65] A. O'Hagan. *Some Bayesian Numerical Analysis. In : Bayesian statistics*, volume 4. Oxford University Press, New York, 1992.

[66] Jay M. Ver Hoef and Ronald Paul Barry. Constructing and fitting models for cokriging and multivariable spatial prediction. *Journal of Statistical Planning and Inference*, 69(2):275–294, 1998.

[67] M. Goulard and M. Voltz. Linear coregionalization model: Tools for estimation and choice of cross-variogram matrix. *Mathematical Geology*, 24(3):269–286, 1992.

[68] Mauricio A. Álvarez and Neil D. Lawrence. Computationally efficient convolved multiple output gaussian processes. *J. Mach. Learn. Res.*, 12:1459–1500, Jul 2011.

[69] X. Hong, L. Ren, L. Chen, F. Guo, Y. Ding, and B. Huang. A weighted gaussian process regression for multivariate modelling. In *2017 6th International Symposium on Advanced Control of Industrial Processes (AdCONIP)*, pages 195–200, 2017.

[70] Xiaodan Hong, Biao Huang, Yongsheng Ding, Fan Guo, Lei Chen, and Lihong Ren. Multi-model multivariate gaussian process modelling with correlated noises. *Journal of Process Control*, 58:11–22, 2017.

[71] Mohammadkazem Sadoughi, Meng Li, and Chao Hu. Multivariate system reliability analysis considering highly nonlinear and dependent safety events. *Reliability Engineering & System Safety*, 180:189–200, 2018.

[72] Michael L. Stein. *Interpolation of Spatial Data: Some Theory for Kriging (Springer Series in Statistics)*. Springer, 1 edition, June 1999.

[73] S. Roberts, M. Osborne, M. Ebden, S. Reece, N. Gibson, and S. Aigrain. Gaussian processes for time-series modelling. *Philosophical Transactions of the Royal Society A: Mathematical, Physical and Engineering Sciences*, 371, 2013.

[74] H. B. Nielsen, S. N. Lophaven, and J. Søndergaard. DACE - a matlab kriging toolbox. *Informatics and Mathematical Modeling, Technical Report, IMM-TR-2002-12*, 2002.

[75] Thomas J Santner, Brian J Williams, William Notz, and Brain J Williams. *The design and analysis of computer experiments*, volume 1. Springer, 2003.

[76] Henry F. Inman and Edwin L. Bradley. The overlapping coefficient as a measure of agreement between probability distributions and point estimation of the overlap of two normal densities. *Communications in Statistics - Theory and Methods*, 18(10):3851–3874, Jan 1989.

[77] Michael James Sasena. *Flexibility and Efficiency Enhancements for Constrained Global Design Optimization with Kriging Approximations*. PhD thesis, University of Michigan, Ann Arbor, MI, 2002.

[78] Hyo-Gil Bae. *A study on EGO method for aerodynamic optimal design*. PhD thesis, Korea Advanced Institute of Science and Technology, Daejeon, Republic of Korea, 2012.

[79] Dieter Heermann Kurt Binder. *Monte Carlo Simulation in Statistical Physics : An Introduction*. Springer-Verlag Berlin Heidelberg, 5 edition, 2010.

[80] Christopher Z. Mooney. *Monte Carlo simulation*. Thousand Oaks, Calif. : Sage Publications, 1997.

[81] Anthony Hayter. *Probability and statistics for engineers and scientists*. Nelson Education, 2012.

[82] Thomas E. Fricker, Jeremy E. Oakley, and Nathan M. Urban. Multivariate gaussian process emulators with nonseparable covariance structures. *Technometrics*, 55(1):47–56, Feb 2013.

[83] Joshua Svenson and Thomas Santner. Multiobjective optimization of expensive-to-evaluate deterministic computer simulator models. 94, Sep 2015.

[84] Dimitri P Bertsekas. Nonlinear programming. *Journal of the Operational Research Society*, 48(3):334–334, 1997.

[85] J. Hirche. Dixon, l. c. w. / szegã¶, g. p. (eds.), towards global optimization. proceedings of a workshop at the university of cagliari, italy, october 1974. amsterdam-oxford. north-holland publ. co. 1975. x. 472 s. *ZAMM - Journal of Applied Mathematics and Mechanics*, 59(2):137–138, Jan 1979.

[86] Aimo Törn and Antanas Žilinskas. *Global optimization*, volume 350. Springer, 1989.

[87] The MathWorks Inc. peaks : Example function of two variables.

[88] L. A. Rastrigin. *Systems of extremal control*. Mir, Moscow, 1974.

[89] R. Sellar, S. Batill, and J. Renaud. Response surface based, concurrent subspace optimization for multidisciplinary system design. In *34th Aerospace Sciences Meeting and Exhibit, Aerospace Sciences Meetings*, Reno,NV, Jan 1996. AIAA.

[90] A. M. Morris, C. B. Allen, and T. C. S. Rendall. Cfd-based optimization of aerofoils using radial basis functions for domain element parameterization and mesh deformation. *International Journal for Numerical Methods in Fluids*, 58(8):827–860, 2008.

[91] Quickersim. https://quickersim.com/.

[92] Dewey H. Hodges and G. Alvin Pierce. *Introduction to Structural Dynamics and Aeroelasticity*. Cambridge Aerospace Series. Cambridge University Press, 2 edition, 2011.

[93] Melanie Mitchell. *An Introduction to Genetic Algorithms*. MIT Press, Cambridge, MA, USA, 1998.

[94] Berend Van den Berg. Boudary layer measurements on a two-dimensional wing with flap. Technical report, Nationaal Lucht-en Ruimtevaartlaboratorium, 1979.

[95] Pointwise.

[96] Francisco Palacios, Thomas D Economon, Aniket Aranake, Sean R Copeland, Amrita K Lonkar, Trent W Lukaczyk, David E Manosalvas, Kedar R Naik, Santiago Padron, Brendan Tracey, et al. Stanford university unstructured (su2): Analysis and design technology for turbulent flows. In *52nd Aerospace Sciences Meeting*, page 0243, 2014.

[97] Youcef Saad and Martin H Schultz. Gmres: A generalized minimal residual algorithm for solving nonsymmetric linear systems. *SIAM Journal on scientific and statistical computing*, 7(3):856–869, 1986.

[98] Philippe Spalart and Steven Allmaras. A one-equation turbulence model for aerodynamic flows. In *30th aerospace sciences meeting and exhibit*, page 439, 1992.

[99] Dimitri J Mavriplis. Multigrid techniques for unstructured meshes. Technical report, Institute for Computer Applications in Science and Engineering, Hampton, VA, 1995.

[100] Northcraft S.A. Roetman, E.L. and J.R. Dawdy. Innovative control effector (ice). Technical Report WL-TR-96-3074, Jan 1996.

[101] Michael Park, Lawrence Green, Raymond Montgomery, and David Raney. Determination of stability and control derivatives using computational fluid dynamics and automatic differentiation. In *17th Applied Aerodynamics Conference*, Norfolk,VA, Jun 1999. American Institute of Aeronautics and Astronautics.

[102] Jangho Park, Christopher L. Ocheltree, Jae Young Choi, Seongim Choi, Pradeep Raj, and Alex Friedman. Stability derivative computation of tailless aircraft using variable-fidelity aerodynamic analysis and wind-tunnel experiments. In *33rd AIAA Applied Aerodynamics Conference*, Dallas, TX, Jun 2015. American Institute of Aeronautics and Astronautics.

[103] Jangho Park, Jae-Young Choi, Youngmin Jo, and Seongim Choi. Stability derivative computation of tailless aircraft using variable-fidelity aerodynamic analysis for control performance analysis. In *54th AIAA Aerospace Sciences Meeting*, San Diego, CA, Jan 2016. American Institute of Aeronautics and Astronautics.

[104] Flying qualities of piloted aircraft. Technical Report MIL-STD-1797A, Wasington D.C., Apr 2012.

[105] J Kay, WH Mason, W Durham, F Lutze, and A Benoliel. Control authority issues in

aircraft conceptual design: Critical conditions, estimation methodology, spreadsheet assessment, trim and bibliography. 24061, 1993.

[106] Jorn H. Baayen. Vortexje - an open-source panel method for co-simulation. *CoRR*, abs/1210.6956, 2012.

[107] Stanford university unstructured (su2).

[108] Francisco Palacios, Juan Alonso, Karthikeyan Duraisamy, Michael Colonno, Jason Hicken, Aniket Aranake, Alejandro Campos, Sean Copeland, Thomas Economon, Amrita Lonkar, Trent Lukaczyk, and Thomas Taylor. Stanford university unstructured (su²): An open-source integrated computational environment for multi-physics simulation and design. In *51st AIAA Aerospace Sciences Meeting including the New Horizons Forum and Aerospace Exposition*, Grapevine (Dallas/Ft. Worth Region), Texas, Jan 2013. American Institute of Aeronautics and Astronautics.

[109] Venkat Venkatakrishnan. Convergence to steady state solutions of the euler equations on unstructured grids with limiters. *Journal of computational physics*, 118(1):120–130, 1995.

[110] Seokkwan Yoon and Antony Jameson. Lower-upper symmetric-gauss-seidel method for the euler and navier-stokes equations. *AIAA journal*, 26(9):1025–1026, 1988.